Towards a free-electron laser driven by a laser wakefield accelerator

by

Maria Pia Anania

A thesis presented in the fulfilment of the requirements for the degree of Doctor of Philosophy in Physics.

Department of Physics, University of Strathclyde

Supervisors:

Prof. Dino A. Jaroszynski

Dr. Mark S. Wiggins

2014

Signed:

Date:

Abstract

The free-electron laser (FEL) is a powerful source of tuneable coherent radiation that currently demands kilometre-scale beam lines for high-energy vacuum ultra-violet (VUV) and X-ray output. Driving an FEL with a laser wakefield accelerator (LWFA) electron beam would radically reduce the size of such systems as well as delivering ultra-short duration radiation pulses. In this thesis, the production and optimal transport of high-quality electron beams in an LWFA and the feasibility of using such beams to drive a VUV FEL has been investigated.

The ALPHA-X LWFA uses a 25 TW femtosecond laser pulse focused into a 2 mm gas jet to accelerate electrons. Using simulation codes [General Particle Tracer (GPT) and TRANSPORT], the initial ALPHA-X transport system has been analysed and an improved system using additional permanent magnet quadrupoles has been designed and installed. GPT has also been applied in analysis of the beam transport through a high resolution magnetic dipole electron spectrometer. It is shown that measurements of beam energy spreads of less than 1% imply a normalised transverse emittance of less than $1\,\pi$ mm mrad, showing that these beams are suitable for driving an FEL.

Efficient electron beam transport through an undulator (100 periods, period = 15 mm) is demonstrated implying an estimated source diameter of 300 μm close to the centre of the undulator (in agreement with simulation). Undulator radiation have been generated using electron beams of energy 83-131 MeV. Output radiation spans the range 180-500 nm and the scaling of photon yield with electron charge provides tentative evidence of coherent emission – the radiation flux is up to ~3 times greater than the expected spontaneous emission flux. The maximum number of photons peaks at 8×10^6 and, assuming a pulse duration of 100 fs, the maximum peak brilliance is 10^{18} photons/second/mm^2/mrad^2/0.1% bandwidth.

Acknowledgements

I would like to express my deep gratitude to Professor Dino Jaroszynski, my research supervisor, for his patient guidance, enthusiastic encouragement and useful critiques of this research work. I would like to express my very great appreciation to Dr Mark Wiggins for the supervision that supervisors didn't have time for, for most of the proof-reading, and moreover for being a friend! His willingness to give his time so generously has been very much appreciated. I would also like to extend my thanks to the technicians of the laboratory, David and Tom for their help.

My special thanks to Bas and Marieke, for helping me with my GPT simulations and for being so very patient with me!

A particular and sincere thanks goes to Gregor and Riju, who have been working hard on the laser side to give me the possibility to run my experiments and to learn a lot: I want to thank both of them for always creating a nice and peaceful lab environment to work in! In particular, I will never forget all the teaching of Riju, both from a working and a personal point of view; and neither I will forget how nice it was to work with Gregor, who has always been a good friend, a good person with which have constructive chats and laugh a lot!

A special thanks to Enrico, who has helped me a lot with the data analysis; all the chats with him have been very fruitful, even if most of the time he was so pessimistic! But I have to say that he was right most of the time!!

I would also like to thank all the other PhD students that have been working in the group during my PhD, in particular Silvia, for being not only a source of knowledge, but also a wonderful flatmate and a shoulder to cry on! I will never forget our aperitifs after work, talking about everything and moreover about the stressful days, especially when the PhD was turning to the end! She has been a second sister to me and I will never thank her enough. I would also like to thank Gion, my best Scottish friend, for being always around for a beer, a pizza and a good whiskey and

for his extraordinary dinners! My sincere thanks also to Grace - my UK daughter - and Constantin - my UK husband - for always being into the lab with me, helping to collect data and moreover for always encouraging my work! It has been a great pleasure to work with them, to share knowledge, to cry and to laugh together!!

I wish to thank Richard, who taught me a lot, especially from the experimental point of view, training me in the lab since the very beginning of my PhD.

My special thanks to my new group members and in particular to Giancarlo, Enrica and Alessandro for always pushing me to finish and moreover to my new boss, Massimo, not only for pushing me to finish, but also for closing an eye when I was dedicating work-time to finish this Thesis!

I also want to thank my best friends Matteo and Peppino for trusting me more than I was... and also for asking me updates about the thesis writing every single week-end!! A special thanks to Angelica, for always listening to me, believing in my work and tolerating my stress.

Special and warm thanks goes to my brother Giulio, my sister Francesca, my brother-in-law Alberto, my niece Sofia and my nephew Gabriele for always being near me even at 2000 km of distance. They have always been on my side, believing in myself more than I was, especially in the last period of my life!

And last, but not least, I want to immensely thank my parents, Paola and Gaetano: they have always supported me and my work. They are the foundation of my life and none of my success, this one included, could have arrived without them. I hope they will always be proud of me and I hope one day I will be able to repay them for all they have done for me so far.

Role of the author

The transport and free-electron laser simulations presented in this thesis were designed by the author. The experiments were performed by the author. The experimental setup and data obtained was from the author. The data analysis were done by the author, and discussed with Dr. Enrico Brunetti and Dr. Mark S. Wiggins.

List of Publications

The following key publications resulted from the work in this thesis:

1. **M.P. Anania**, E. Brunetti, S.M. Wiggins, D.W. Grant, G.H. Welsh, R.C. Issac, S. Cipiccia, R.P. Shanks, G.G. Manahan, C. Aniculaesei, S.B. van der Geer, M.J. de Loos, M.W. Poole, B.J.A. Shepherd, J.A. Clarke, W.A. Gillespie, A.M. MacLeod, D.A. Jaroszynski, An ultrashort pulse ultra-violet radiation undulator source driven by a laser plasma wakefield accelerator, Appl. Phys. Lett. **105**, 264102 (2014).
2. **M.P. Anania**, E. Brunetti, S. Cipiccia, D. Clark, R. Issac, G.G. Manahan, T. McCanny, A.W. Reitsma, R.P. Shanks, G.H. Welsh, S.M. Wiggins and D.A. Jaroszynski, The ALPHA-X beam line: toward a compact FEL, Proceedings of IPAC'10, **TUPE052**, Kyoto, Japan (2010).
3. **M.P. Anania**, D. Clark, R.C. Issac, A.J.W. Reitsma, G.H. Welsh, S.M. Wiggins, D.A. Jaroszynski, S.B. van der Geer, M.J. de Loos, M.W. Poole, J. Clarke, B. Shepherd, The ALPHA-X beam line: toward a compact FEL, Proceedings of FEL2009, **MOPC71**, Liverpool, UK (2009).
4. **M.P. Anania**, D. Clark, R.C. Issac, A.J.W. Reitsma, G.H. Welsh, S.M. Wiggins, D.A. Jaroszynski, S.B. van der Geer, M.J. de Loos, M.W. Poole, J. Clarke, B. Shepherd, Transport of ultra-short electron bunches in a free-electron laser driven by a laser-plasma wakefield accelerator, Proceedings of PAC09, **TU2BC04**, Vancouver, Canada (2009).
5. **M.P. Anania**, D. Clark, S.B. van der Geer, M.J. de Loos, R. Isaac, A.J.W. Reitsma, G.H. Welsh, S.M. Wiggins, D.A. Jaroszynski, "Transport of ultra-short electron bunches in a free-electron laser driven by a laser-plasma wakefield accelerator", Proc. SPIE **7359**, Harnessing Relativistic Plasma Waves as Novel Radiation Sources from Terahertz to X-Rays and Beyond, 735916 (2009).

6. **M.P. Anania**, S.B. van der Geer, M.J. de Loos, A.J.W. Reitsma and D.A. Jaroszynski, Beam Transport of Ultra-Short Electron Bunches, 35th EPS Conference on Plasma Phys. Hersonissos, 9 - 13 June 2008 ECA Vol.**32D**, P-1.147 (2008).

Other publications where the author has contributed and are related to this thesis:

7. G.G. Manahan, E. Brunetti, C. Aniculaesei, R.P. Shanks, **M.P. Anania**, S. Cipiccia, R.C. Issac, G.H. Welsh, S.M. Wiggins, D.A. Jaroszynski, *"Characterisation of laser-driven single and double electron beams with a permanent quadrupole triplet and pepper-pot mask"*, New J. Phys. **16**, 103006 (2014).
8. S.M. Wiggins, R.C. Issac, G.H. Welsh, E. Brunetti, R.P. Shanks, **M.P. Anania**, S. Cipiccia, G.G. Manahan, C. Aniculaesei, B. Ersfeld, M.R. Islam, R.T.L. Burgess, G. Vieux, W.A. Gillespie, A.M. MacLeod, S.B. van der Geer, M.J. de Loos, D.A. Jaroszynski, *"High quality electron beams from a laser wakefield accelerator"*, Plasma Phys. Control. Fusion **52**, 124032 (2010).
9. E. Brunetti, R.P. Shanks, G.G. Manahan, M.R. Islam, B. Ersfeld, **M.P. Anania**, S. Cipiccia, R.C. Issac, G. Raj, G. Vieux, G.H. Welsh, S.M. Wiggins, D.A. Jaroszynski, *"Low emittance, high brilliance relativistic electron beams from a laser-plasma accelerator"*, Phys. Rev. Lett. **105**, 215007 (2010).
10. J.G. Gallacher, **M.P. Anania**, E. Brunetti, F. Budde, A. Debus, B. Ersfeld, K. Haupt, M.R. Islam, O. Jäckel, S. Pfotenhauer, A.J.W. Reitsma, E.G. Rohwer, H.-P. Schlenvoigt, H. Schwoerer, R.P. Shanks, S.M. Wiggins, D.A. Jaroszynski, *"A method of determining narrow energy spread electron beams from a laser plasma wakefield accelerator using undulator radiation"*, Phys. Plasmas **16**, 093102 (2009).

11. E. Brunetti, G.G. Manahan, R.P. Shanks, M.R. Islam, B. Ersfeld, **M.P. Anania**, S. Cipiccia, R.C. Issac, G. Vieux, G.H. Welsh, S.M. Wiggins, D.A. Jaroszynski, *"Characterisation of electron beams from laser-driven particle accelerators"*, AIP Conf. Proc. **1507**, 672 (2012).
12. W.A. Gillespie, **M.P. Anania**, C. Aniculaesei, E. Brunetti, S. Cipiccia, B. Ersfeld, M.R. Islam, R.C. Issac, D.A. Jaroszynski, G.G. Manahan, R.P. Shanks, G.H. Welsh, S.M. Wiggins, S.P. Jamison, and A. MacLeod, *"High Quality Electron Beams Generated in a Laser Wakefield Accelerator"*, Proceedings of PAC11, **MOP113**, New York, USA (2011).
13. S.M. Wiggins, J.G. Gallacher, H.-P. Schlenvoigt, H. Schwoerer, G.H. Welsh, R.C. Issac, E. Brunetti, G. Vieux, R.P. Shanks, S. Cipiccia, **M.P. Anania**, G.G. Manahan, C. Aniculaesei, A. Subiel, D.W. Grant, A.J.W. Reitsma, B. Ersfeld, M.R. Islam, D.A. Jaroszynski, *"Laser-driven radiation sources in the ALPHA-X project"*, Proc. SPIE **8075**, 80750O (2011).
14. G.G. Manahan, E. Brunetti, R.P. Shanks, M.R. Islam, B. Ersfeld, **M.P. Anania**, S. Cipiccia, R.C. Issac, G. Raj, G. Vieux, G.H. Welsh, S.M. Wiggins, D.A. Jaroszynski, *"High resolution, single shot emittance measurement of relativistic electrons from laser-driven accelerator"*, Proc. SPIE **8079**, 807909 (2011).
15. R.P. Shanks, **M.P. Anania**, E. Brunetti, S. Cipiccia, B. Ersfeld, J.G. Gallacher, R.C. Issac, M.R. Islam, G. Vieux, G.H. Welsh, S.M. Wiggins, D.A. Jaroszynski, *"Pepper-pot emittance measurement of laser-plasma wakefield accelerated electrons"*, Proc. SPIE **7359**, 735907 (2009).
16. S.M. Wiggins, **M.P. Anania**, E. Brunetti, S. Cipiccia, B. Ersfeld, M.R. Islam, R.C. Issac, G. Raj, R.P. Shanks, G. Vieux, G.H. Welsh, W.A. Gillespie, A.M. MacLeod, D.A. Jaroszynski, *"Narrow energy spread electron beams from a laser-plasma accelerator"*, Proc. SPIE **7359**, 735914 (2009).
17. R.C. Issac, G. Vieux, G.H. Welsh, R.P. Shanks, E. Brunetti, S. Cipiccia, **M.P. Anania**, X. Yang, S.M. Wiggins, M.R. Islam, B. Ersfeld, J. Farmer, G. Raj, S. Chen, D. Clark, T. McCanny, D.A. Jaroszynski, *"Electron beam pointing stability of a laser wakefield accelerator"*, Proc. SPIE **7359**, 735915 (2009).

Contents

List of Figures

List of Tables

Chapter 1

Introduction

1.1 Overview

Particle accelerators are used in a wide variety of fields, ranging from medicine and biology to high-energy physics. In particular, Gigaelectron Volt (GeV) electron accelerators are vital to synchrotron radiation, X-ray free-electron laser and high-energy particle physics facilities. Radiofrequency (RF)-based accelerators are limited by electrical breakdown to relatively low accelerating fields (10 – 100 MVm^{-1}) [1], and therefore these kind of structures require tens to hundreds of metres to reach the multi-GeV beam energies needed to drive short wavelength radiation sources, and kilometres to reach particle energies interesting for high-energy physics [2].

Laser-wakefield accelerators (LWFAs) [3-9], on the other hand, are able to produce accelerating fields of the order of 10–100 GVm^{-1}, enabling the possibility to have very compact devices by reaching GeV energies in just a few centimetres. Until a few years ago, the laser intensity required for LWFAs to reach GeV energies was not maintained over the required distance and, hence, acceleration was limited to the 100 MeV scale [10-12]. However, and contrary to predictions that petawatt-class lasers would be needed to reach GeV energies [13,14], a set of experiments at the Lawrence Berkeley National Laboratory has demonstrated production of a high-quality electron beam with 1 GeV energy by channelling a 40 TW peak-power laser pulse in a 3.3 cm gas-filled capillary discharge waveguide [15-17]. GeV-scale electron energies have subsequently been generated in several other laboratories using capillary waveguides [17-20], gas-jets [21] and gas-cells.

1.2 Laser-plasma accelerators

The story of laser-plasma accelerators started in 1979 with Tajima and Dawson [5], a few years before the invention of chirped pulse amplification (CPA), when they proposed the use of high-power lasers propagating in under-dense plasma to

accelerate electrons to relativistic energies in very short distances. The principle of laser wakefield acceleration can be explained by the well-known analogy of a speedboat travelling on the sea followed by a surfer. As the speedboat travels, it generate waves; if the surfer is able to reach the crest of the wave, he/she can surf it and be accelerated. In the same way, the laser pulse travelling in the plasma generates waves and trapped electrons surfing these waves can be accelerated.

The result, given in 1995 by Modena et al. [7], about the electron accelerating gradient from a laser plasma accelerator of ≈100 GV/m was astonishing: using the plasma as an accelerating medium, the accelerator is practically immune to electrical breakdown (which is the major limit of RF accelerators). However, the quality of the electron bunches from an LWFA was not high enough for most of the applications: even with a 100 MeV energy and about 1 nC charge, the spectral distribution was thermal showing an exponential decay.

Since then, a lot of work has been conducted on these novel accelerators and a lot of physics behind the process has been understood. Today, electron bunches from laser plasma accelerators are much improved [7,11,12] and several groups have reported better and better beam quality: high energy (up to 1 GeV) [17], quasi-mono-energetic (less than 1% energy spread) [22], low emittance (down to 1 π mm mrad) [22], femtosecond duration bunches [22,23] and kiloAmpere peak currents [22,23]. If the present parameters are still far away from the energy and luminosity range of interest for high energy physics, it is worthwhile noticing that this is still a very young technology compared to standard accelerators that date back to the early decades of the 20th century. A rapid growth can be forecast in the next several years that can lead to a further increase in power, size reduction, lower cost and higher reliability. If they cannot replace at least for the moment the conventional accelerator, probably in the near future the laser-plasma accelerators could be employed in niche fields harnessing their compactness that is their strength.

1.3 Free-Electron Lasers

The term "free-electron laser (FEL)" was introduced in the 1970s but the development of coherent radiation sources based on an electron beam propagating in a magnetic undulator goes back to the ubitron of the 1950s [24]. However, the device only really started to excite the scientific community at the beginning of 1990s when high-energy linear accelerators were seen as being capable of providing beams with high enough quality for FEL operation in the X-ray regime and infrared (which would make them superior to synchrotron light sources).

The interest in such devices comes from the fact that the FEL is a source of powerful and tuneable coherent radiation, able to cover those regions of the electromagnetic spectrum which are not accessible to conventional lasers, such as the far infra-red [25], the extreme ultra-violet down to the water window [26] and into hard X-rays [27].

1.3.1 Overview

The first theoretical explanation of the FEL has been given by Madey in 1971, when he proposed that an undulator structure working as an amplifier at optical wavelengths could replace the active medium between the mirrors of the laser optical cavity. He called such a device a *free-electron laser* [28].

Madey gave an interesting calculation of the gain based on an approximate treatment of relativistic quantum theory [29]. He argued that the sinusoidal magnetic field of the undulator, independent of the time in the L-frame, would be seen by electrons in the E-frame as a photon flux from which they could be scattered, and related the transition rates of this process to the more easily calculable rates of Compton scattering. Transforming back into the L-frame, the Compton cross-section was used to calculate the transition rate from all initial electron and photon states to a given final state, a desired cavity mode. He thus obtained a theory very similar to that of the stimulated Compton Effect, which had

been dealt with already in 1933 by Kapitza and Dirac [30], and was being studied at the same time by other authors [31,32], as a possible means of amplifying coherent optical radiation.

1.4 Global context

1.4.1 Particle Accelerators

A particle accelerator is a device that uses electromagnetic fields to propel charged particles to high speed and to contain them in well-defined bunches [33]. The two basic classes of accelerators are essentially the electrostatic field accelerators and the oscillating field accelerators. The first kind uses static electric fields to accelerate particles, while the second uses RF electromagnetic fields to accelerate particles. Both types of accelerator are limited in the maximum kinetic energy achievable from the particle by electrical breakdown in the accelerating cavity [34].

The RF-based accelerators were first developed in the 1920s [35] and are still the basis for all modern accelerator concepts and large-scale facilities, see fig. 1.1.

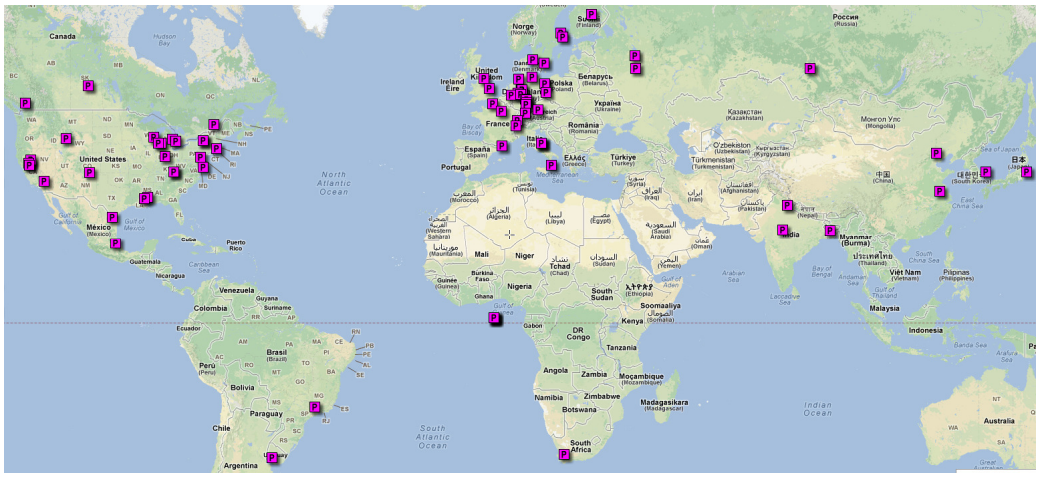

Figure 1.1: World map of major particle accelerators.

Conventional techniques are used in particle physics as colliders, as for example the Large Hadron Collider (LHC) at CERN [36], the Relativistic Heavy Ion Collider (RHIC) at Brookhaven [37] and Tevatron at Fermilab [38], and in a large variety of applications, including particle therapy for oncology and as synchrotron light sources for fields such as condensed matter physics [39-41].

Oscillating field accelerators use high voltage sources to accelerate particles; the electrodes can be arranged either in a straight line or in a circle, and in particular they are referred as linear accelerators (linacs) if the particles are accelerated in a straight line. The most important and longest linac is the Stanford Linear Accelerator (SLAC) which is 3 km long and can provide up to 50 GeV electrons and positrons [42].

When the particles are accelerated in a circle, the accelerators are called synchrotrons. In this case, the particles are accelerated in a ring of constant radius. Examples of synchrotron accelerators are the European Synchrotron Radiation Facility (ESRF) in Grenoble [43], France, accelerating electrons up to 6 GeV, the Advanced Photon Source (APS) at Argonne (USA) [44], accelerating electrons up to 7 GeV, SPring-8 in Japan [45], accelerating electrons up to 8 GeV, the SOLEIL synchrotron storage ring in Saclay (France), accelerating electrons up to 2.7 GeV and the Diamond Light Source in the UK [46] which can accelerate electrons up to 3 GeV around a 560 m circumference storage ring.

1.4.2 Light sources

Most of the particle accelerators use the accelerated particles as radiation sources. There are many light sources facility around the world, as can be seen from the map in fig. 1.2.

Figure 1.2: World map of major light sources.

Light sources can help provide answers to the fundamental questions: "what is the planet made of? What are the processes that sustain life? How can viruses be conquered?". Providing a very large spectral range of light (from radio-waves to hard X-rays), light sources can provide light to "see" at the molecular level enabling research on samples on a very detailed scale, in much finer detail than the human eye could possibly make out. These questions can only be answered at the molecular level; at the level of atoms and electrons. Light sources provide a tool for answering these questions. They can be compared to a 'super microscope', by providing intensely bright forms of X-ray, infrared and ultraviolet light, which enables research on samples in the tiniest detail. Each range of light is suited to a particular task. To 'see' atoms needs a form of light that has a much shorter wavelength than visible light. As a general rule, short-wavelength (hard) X-rays are most useful for probing atomic structure. Again, as a general rule, longer-wavelength (soft) X-rays and ultraviolet light are good choices for studying chemical reactions. Infrared is ideally suited to studying atomic vibrations in molecules and solids, and at its very long wavelength end (terahertz waves), it is also useful for certain types of electronic structure experiments.

These intense beams of light can be produced either using synchrotrons or FELs. Within UK the most important light facility is Diamond [46], which is a synchrotron science facility located in Oxfordshire. Worldwide, there are many light source facilities, for example, at DESY in Germany [47], the Canadian Light Source (CLS) in

Canada [48], Dafne in Italy [49], the Linac Coherent Light Source (LCLS) at SLAC [50] and at Brookhaven National Laboratory in the US [51]. LCLS was the world's first X-ray FEL, followed by SACLA, Japan [52] and under construction are the European XFEL [47], Germany and the Swiss Light Source [53] among others.

1.4.3 LWFA-driven radiation sources

There are around thirty groups working on laser wakefield acceleration worldwide as seen from fig. 1.3, but not all the groups have a high-power laser to perform laser wakefield acceleration experiments.

The LWFA community, however, is increasing quickly because of the possibility to reach high accelerating gradients (of the order of the GV/m) and therefore opening the way to table-top accelerators and light sources. Between the LWFA light sources, there are (i) betatron sources [54-58], which is the radiation produced by the electrons while oscillating in the plasma, (ii) bremsstrahlung sources [59-61], which is the so called "stop-and-start" radiation produced when a charged particle is accelerated or decelerated, (iii) undulator sources [62-65], which is the radiation emitted by an electron bunch forced to oscillate in an alternating pole magnetic structure, (iv) THz sources [66-70], which is the radiation emitted by electrons upon passing through a material and (v) Thomson scattering sources [71-76], which is the radiation produced by collisions between electrons and photons.

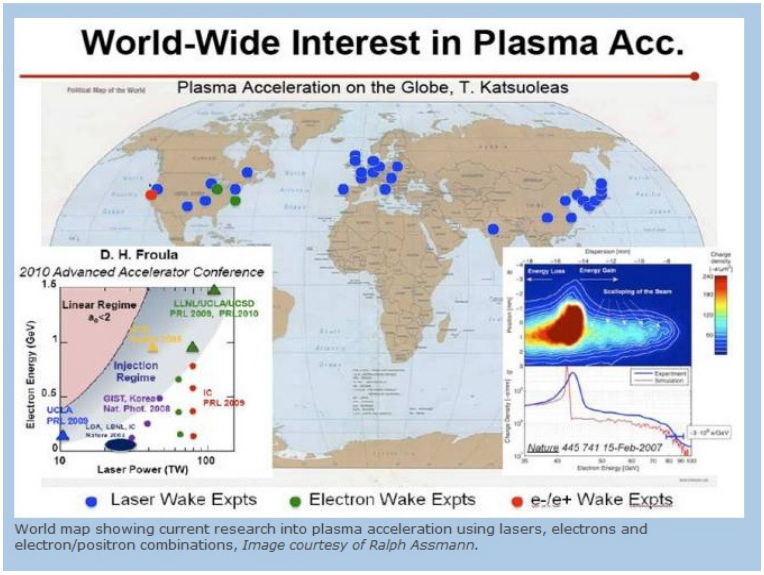

World map showing current research into plasma acceleration using lasers, electrons and electron/positron combinations, *Image courtesy of Ralph Assmann.*

Figure 1.3: World map showing the situation (January 2011) of current research into plasma acceleration: blue dots for LWFA, green dots for the plasma wakefield acceleration and red dots for electron/positron combinations [77].

The most common phrase in wakefield acceleration is certainly "table-top"; the same word is applied to the radiation sources: from the terahertz regime to gamma-rays. Radiation can be emitted by several different sources, as indicated in the previous paragraph.

1.5 Research in the ALPHA-X project

The ALPHA-X (***A****dvanced* ***L****aser-****P****lasma* ***H****igh-energy* ***A****ccelerators towards* ***X****-rays*) project aims to develop laser-plasma accelerators and apply these to produce coherent short-wavelength radiation sources, for example, in a free-electron laser. To realise these objectives, an interdisciplinary programme involving advanced plasma, laser and electron beam physics has been set up. The ultra-short pulses of short wavelength radiation from these compact sources have the potential of revolutionising time-resolved studies in a wide range of applications.

To meet the challenge of producing coherent X-rays in a free-electron laser (FEL), a very high quality electron beam is required. The electron energy must be sufficiently high to enter the short-wavelength regime. Clearly, this is where plasma-based techniques offer a great advantage because of the high accelerating fields. The ALPHA-X programme investigates the feasibility of using plasma-based acceleration for producing ultra-short electron bunches with high charge, low energy spread and low transverse emittance suitable for driving an FEL, or as an injector for other accelerators. A wide range of state-of-the-art diagnostic equipment is being developed to characterise the very high quality, short duration electron bunches and to measure the plasma and FEL radiation properties.

1.5.1 Monoenergetic electron beams

High quality electron beams have been produced using the ALPHA-X laser-plasma accelerator driven by a femtosecond laser with a peak power of 26 TW. The electrons have an energy up to 150 MeV and have been produced with a 2 mm gas jet accelerator and the measured rms relative energy spread is less than 1%. Shot-to-shot stability in the central energy is 3% [78]. The experimental set-up is shown in fig. 1.4.

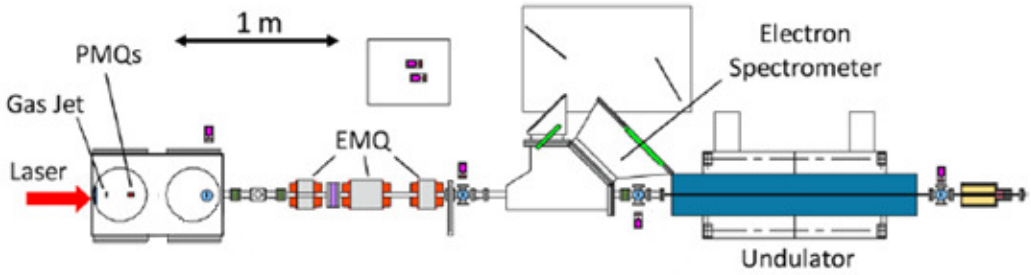

Figure 1.4: Layout of the ALPHA-X beam line experimental set-up.

The laser beam is focused at the leading edge of a 2 mm round gas jet to a spot radius of 20 µm by an on-axis F/18 spherical mirror. At the focus, the laser peak intensity is 2×10^{18} W cm^{-2}. Electrons are self-injected from the background plasma

into the plasma density wake trailing behind the laser pulse through the combined action of the ponderomotive force and the restoring force of the plasma.

The beam line, as shown in fig. 1.4, is composed of a triplet of permanent magnet quadrupoles (more detail on the design of this triplet can be found in chapter 4), a triplet of dynamic quadrupoles, a high resolution electron spectrometer, one undulator section and a low resolution dipole which is used to measure the electron beam energy and to dump the electrons.

1.5.2 LWFA-driven undulator radiation

In 2008 the Strathclyde ALPHA-X group has collaborated in an experiment with FSU Jena in Germany on the production of incoherent synchrotron radiation in the visible range from electrons accelerated by the laser wakefield technique as they propagate through an undulator.

The experimental layout is shown in fig. 1.5. The experiment has been carried out with the JETI laser, which delivered 430 mJ energy on target, in 85 fs duration, focused by an off-axis parabola to a 95 μm^2 FWHM spot, yielding a peak intensity of 5×10^{18} Wcm^{-2}. At the focus, there was a 2 mm diameter supersonic helium gas jet, generating a super-Gaussian gas density profile with peak density of 2×10^{19} cm^{-3}.

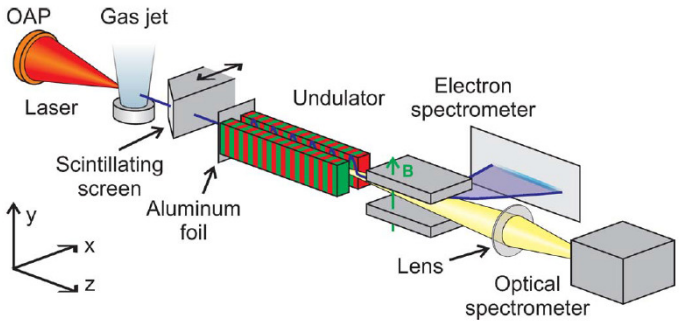

Figure 1.5: Layout of the LWFA undulator experiment in Jena [62].

The electrons are accelerated in the range of energy 55-75 MeV. At a distance of 30 cm after the gas jet, there was a scintillating screen imaged by a CCD camera; the scintillating screen could be removed to let the electron beam travel through the

undulator. The undulator (50 periods of 2 cm each, peak magnetic field strength 330 mT and an undulator parameter of 0.6), was placed 40 cm from the accelerator. After the undulator, there was an electron spectrometer (permanent magnet dipole with a detectable electron energy [14-85] MeV): it was placed 185 cm from the gas jet. Undulator radiation was collected and focused into the entrance slit plane of a symmetrical 200 mm Czerny-Turner spectrometer which was coupled by a thermoelectrically cooled CCD camera (Andor D0-420 BN). In fig. 1.6a, there is a typical radiation spectrum (red line) produced during the experiment, together with the measured electron spectrum (black line). As can be seen, the radiation produced is in very good agreement with the theoretical expectation (green line).

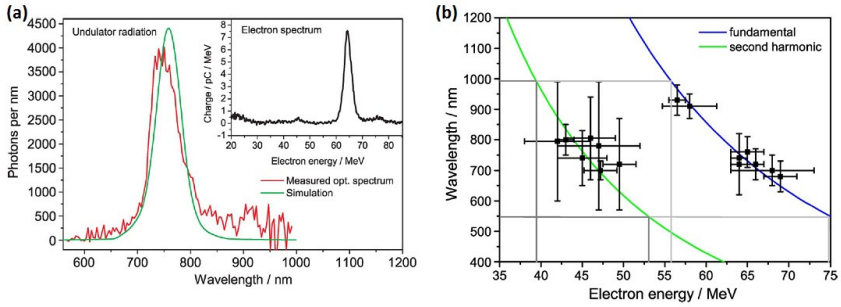

Figure 1.6: (a) typical undulator radiation measured during the Jena experiment and (b) first and second harmonic central wavelength for different electron beam energies.

Displayed in fig. 1.6b are, for different shots, the central wavelength measured for the first and second harmonics (blue and green line respectively) of the undulator radiation. Also in this case, the agreement between measurement and expectation is very good.

1.6 Work presented in this thesis

This thesis is divided into two parts, a theoretical and simulation part and an experimental part. The first part is represented by chapters 2 to 4, while the second part is represented by chapters 5 to 7. Finally, in chapter 8, there is a summary of

the thesis and some considerations on the work that has been carried out and that which could be done in the near future.

In particular, this thesis focuses on the FEL radiation, which is a powerful and tuneable radiation source. Electron bunches accelerated in a laser wakefield can have a very high peak current, due to the fact that the duration of these beams is very short. In fact, both simulations and experiments [79] show that an electron bunch duration down to 2 fs is achievable. This means that, by designing the transport section well, the very short duration of the bunches can be preserved, as studied in this thesis. High peak current, together with a matched transport in the undulator section and a low energy spread, could, in theory, ensure FEL operation in a very short distance (the table-top FEL).

Another important aspect discussed in this thesis is the choice of the accelerator, which is of paramount importance. Recent studies in laser wakefield acceleration shows that there are several different accelerators that can be used in order to efficiently accelerate electrons, which mainly are gas jets, capillaries and gas cells [11-15]. In particular, work in this thesis has focused attention on gas jets, mainly to minimise complexity while optimising the diagnostics.

Further detail on the work presented in this thesis is as follows:

In Chapter 2, the theory of the laser wakefield acceleration is given. Femtosecond duration lasers will be described in section 2.2, where the CPA technique will also be described together with self-guiding in plasmas. Section 2.3 contains relevant theory of laser-plasma acceleration, starting from self-injection of electrons and ending with the limits of this accelerating technique, which are dephasing and pump depletion. Finally, in section 2.4, processes determining the high quality of LWFA-accelerated electron bunches are given.

Chapter 3 is devoted to FEL theory: in section 3.2, spontaneous undulator radiation will be treated, in section 3.3 the principle of FEL operation will be described, with particular attention given to high-gain theory, self-amplified spontaneous radiation, the limits of the FEL and the requirements in terms of electron beam quality and, eventually, the two-wave model will be described. In section 3.4, the difference

between incoherent and coherent undulator radiation will be discussed. Latterly, section 3.5 is dedicated to FEL simulations; in particular, two different codes have been used to simulate the FEL performances for the ALPHA-X accelerator and the results, together with the code limitations, will be described at the end of this chapter.

Chapter 4 is the last theoretical chapter and is devoted to electron beam transport design and simulations; at the beginning of the chapter, all the simulations performed with the beam line designed prior to this thesis will be discussed and, in particular, the need of a permanent magnet quadrupole triplet to be placed as close as possible to the accelerator will be explained. The simulations performed to design this triplet of quadrupoles will be detailed in section 4.3 while, in section 4.4, all the simulations carried out on the updated beam line will be described. In particular, the simulations have been performed with models as accurate as possible, so to be able to have very accurate transport simulations. Also, pointing instability is taken into account and the angular acceptance of the permanent magnet triplet is shown. Eventually, the main simulation code used for the design exercise and simulations has been benchmarked with a well-known transport code and the last part of this chapter is devoted to highlighting the agreement between the two codes.

The experimental part of this thesis starts from Chapter 5, which is fully dedicated to the experimental set-up description. In particular, section 5.2 is dedicated to the femtosecond laser system and the diagnostics used to check its performance. Section 5.3 is dedicated to the ALPHA-X beam line, starting from the choice of the accelerator, to all the diagnostics present on the beam line to diagnose the quality of the electron bunches. Lastly, section 5.4 is dedicated to the free-electron laser section and describes the undulator module and detection systems.

Chapter 6 is devoted to the generation and the transport of ultra-short electron bunches. Section 6.2 shows the electron bunches exiting the accelerator and shows how, also from an experimental point of view, it is of paramount importance to use the permanent magnet quadrupole triplet: the results of the transport using the

triplet of permanent magnet is described in section 6.3, where two different set-ups for the permanent magnet triplet are described. In the same section, the experimental transport results obtained with the two set-ups will be compared to simulations: the agreement is very good in both cases but, while in the first case, the comparison is much easier, the second case has been much more complex mainly due to energy instability of the electron bunches from shot-to-shot. Section 6.4 describes electron bunches quality measurements: energy, energy spread, emittance, duration and charge have been characterised. In section 6.5, the transport of electron bunches through the undulator is described and, in particular, in section 6.6 all the transport issues are described, with special attention paid to undulator misalignment and the effect of laser beam filters on the electron beam quality.

Chapter 7 is devoted to the undulator radiation experimental results. There are a few different setups described in this chapter, starting from a very basic experiment where the undulator radiation has been detected using a CCD camera to the most complex experiment where radiation has been detected with a monochromator spectrometer optimised to detect UV and VUV wavelength. In the last part of this chapter, the beam quality dependence on the measured radiation will be presented as well as the output scaling. The results presented will show that the measured radiation is incoherent, but the brilliance is up to two orders of magnitude higher than expected.

Chapter 8 is the final chapter and summarises all the conclusions and possible future upgrades and directions of research.

Chapter 2

Laser wakefield acceleration theory

2.1 Introduction

A milestone in laser technology was the introduction of chirped pulse amplification (CPA) by Strickland and Mourou in 1985 [84] that enabled the latest revolution in the production of ultra-high peak power lasers, amplifying very short pulses (femtosecond) to energy previously available only for longer pulses. However, CPA has already encountered some limits set by the damage threshold of the diffraction gratings of the compressor and the bandwidth of the amplifier gain media.

A promising new amplification scheme that could replace or integrate into CPA is Raman amplification in plasma [80]. This technique is based on a long pump beam and a short probe beam counter-propagating in an under-dense plasma, that can tolerate much higher laser intensity than solid-state devices, having a plasma frequency equal to the difference in frequency of the two laser pulses. The two pulses interact via stimulated Raman backscattering and a large fraction of the energy of the pump beam is transferred to the probe beam. Recent numerical studies [81] predict the feasibility of multi-petawatt lasers based on Raman amplification within a parameter window that prevents unwanted plasma instabilities.

But the question is: why to go for higher and higher power? High-power, ultra-short pulse lasers can open the frontiers to new physics: electron-positron plasma production, inertial confinement fusion, table-top ion and electron accelerators based on laser-solid target or laser-plasma interactions as well as new ultra-compact light sources.

2.2 High-power femtosecond lasers

Realisation of the laser-plasma accelerator is inherently connected to the development of high-power laser systems of pulse duration in the range ~10-100 fs.

As will be described in section 2.3, optimal acceleration performance requires matching the laser pulse duration to the plasma wavelength which is governed by the plasma density. With typical densities of 10^{18}-10^{19} cm^{-3} produced in gas jets, gas cells and capillary waveguides, this calls for laser pulse durations of 10s of fs.

The first sub-picosecond laser pulses were produced in the 1970s [82] but two significant technological developments in the 1980s paved the way for the rapid sophistication and commercialisation of high-power fs lasers. These were Kerr-lens mode-locking (KLM) and CPA. The most common gain medium applied in such systems is Ti:sapphire because it has a very wide gain bandwidth (>400 nm giving a minimum possible pulse of 4 fs), high thermal conductivity for effective heat removal and high saturation fluence.

In the past decade, 10 fs pulses have been achieved from a Ti:Sapphire laser [83] using the CPA technique first suggested for lasers in 1985 [84] in order to amplify short pulses. In this scheme the femtosecond laser pulse is firstly stretched in time (chirped in frequency), then amplified and finally recompressed. Details of the chirped pulse amplification are given in the next paragraph.

2.2.1 Chirped Pulse Amplification

The development of CPA has to be credited to Strickland and Mourou [84]. This technique, used in microwaves devices for many years, enabled the latest revolution in production of high peak powers from lasers through amplification of very short (femtosecond) laser pulses to pulse energies previously available only from long-pulse lasers. CPA has rapidly bridged the gap from the initial low power systems to multi-terawatt and petawatt scale systems.

The idea of CPA is simple and beautiful at the same time: given the damage threshold limitations encountered by ultra-short laser pulses while propagating through the laser amplifier, the ultra-short pulse will be manipulated in a controllable and reversible fashion so that the laser amplifier never encounters a short, high power pulse, and only the laser system components compatible with

such high peak powers will be exposed to it. A schematic layout of CPA is shown in fig. 2.1.

The CPA technique is based on the idea of using reversible manipulation of the temporal characteristics of ultra-short laser pulses. An ultra-short laser pulse is firstly stretched in time introducing a frequency chirp in the beam; this is done using a pair of diffraction gratings arranged so that the low-frequency component of the laser pulse travels a shorter path than the high-frequency ones.

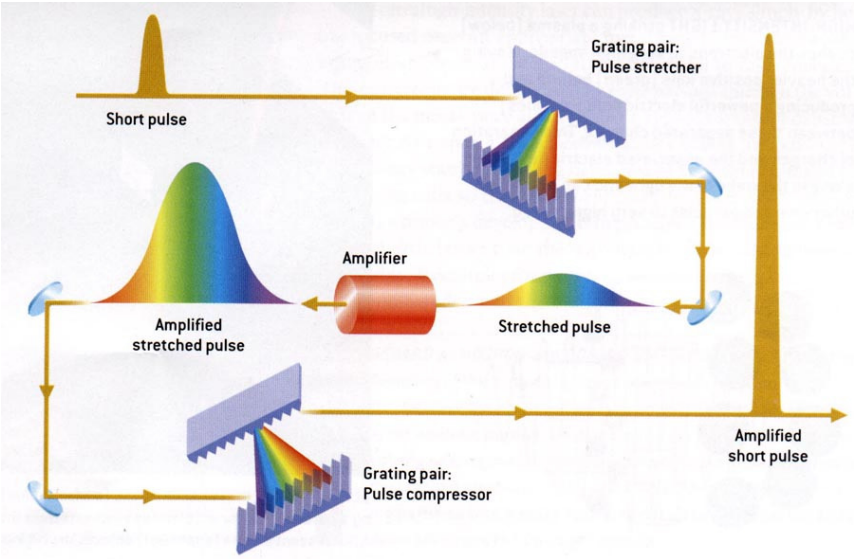

Figure 2.1: Layout of the CPA technique showing the stretching, amplification and compression sections.

After passing through the grating pair, the laser pulse is much longer (typically 100-200 ps) than the original by a factor of 10^3 to 10^5. After this operation, the pulse now has an intensity sufficiently low compared with the intensity damage limit of gigawatts per square centimetre for optical components, and, therefore, can be safely introduced into the gain medium and amplified by a factor 10^6 or more.

Finally, the amplified laser pulse is recompressed back to the original pulse width through the reverse process of that used for stretching, that is, a grating pair introduces a frequency chirp to the beam of equal magnitude but opposite sign to

the one introduced at the stretcher. The final output pulse is therefore of high energy and ultra-short duration with peak power many orders of magnitude higher than that achievable before the invention of CPA.

2.2.2 Self-guiding in plasma

Propagation of ultra-high intensity laser beams in plasmas is a very interesting process because of their potential applications for the development of X-ray lasers [85,86], plasma-based accelerators [7,9,11,12], and "fast-ignition" [87,88]. All these applications need high intensity laser beams to propagate controllably over a long distance with high directionality. If the laser peak power is high enough, a laser beam can overcome the natural limit of refraction and focus in the plasma due to non-linear self-interaction [89-93]. The balance between this self-focusing and diffraction can provide a condition for the long-distance propagation of the beam with peak intensity higher than otherwise achievable by focusing in vacuum: this is crucial for realising "table-top" GeV-class laser wakefield accelerators.

Even though the accelerating gradients can be very large in a LWFA, if the interaction length is short, the overall energy gain will be modest. To reach the high intensity necessary to create the plasma waves, the laser pulses must be focused tightly and thus the interaction length will be short, limited by diffraction to the Rayleigh range $\left(Z_R = \pi r_0^2 / \lambda\right)$. Several methods have been proposed and demonstrated to extend the propagation distance beyond the diffraction limit, most notably pre-formed channels [7,9,94-101] and relativistically self-guided channels [89,91,102-104]. In general, the difference between these two schemes is the way to ionize the gas: in pre-formed channels the gas is externally ionized and the laser is used only to drive plasma waves while in self-guided channels is the laser that both ionizes the gas and drives the plasma waves.

The method described here is the self-guided channel. When a laser propagates through a plasma, the index of refraction, $n = \left(1 - \omega_p^2 / \omega_0^2\right)^{1/2}$ depends on the laser frequency, ω_0, and the plasma frequency, ω_p. For low laser power, the index is

essentially constant; however, if the laser power is higher, the index varies with the radius, because the laser intensity varies with radius while the plasma frequency is a function of the relativistic mass factor. Under these conditions, the plasma acts like a positive lens and focuses the beam. This effect, known as relativistic self-focusing, has been shown to have a power threshold given by $P_c = 16.5 n_c / n_e$ GW, where n_c is the critical density and n_e is the electron density [98-100]. Recent simulations [105] have shown that this effect has different properties, depending on the laser power. At the critical power threshold, only the focal intensity increases. However, when the incident laser power is increased ($P/P_c = 3-4$), the beam extends and forms a second focus. As the laser power is increased further, multiple foci occur, which eventually merge into a single channel.

It can therefore be concluded that relativistic self-guiding [3] can extend the propagation distance of high-power pulses due to self-consistent modification of the plasma refractive index; however, this process is limited by nonlinear effects such as the erosion of the leading edge of the pulse. Obtaining GeV energies without guiding channel requires, therefore, the laser spot size to be large, so as to increase Z_R, but this also increases the required laser power to PW levels [13,14]. In addition, using a large laser spot size can result in an undesirable increase in the electron beam emittance.

2.3 Laser plasma acceleration

In contrast to conventional radio-frequency (RF) linear accelerators (linacs), ionised plasmas can sustain electron plasma waves with fields in excess of $E_0 = c m_e \omega_p / e$ or:

$$E_0[V/m] \simeq 96\sqrt{n_e[cm^{-3}]}\,, \qquad [2.1]$$

where

$$\omega_p = \left(n_e e^2 / \varepsilon_0 m_e\right)^{1/2} \qquad [2.2]$$

is the electron plasma frequency, n_e is the ambient electron density, m_e and e are the electron rest mass and charge, respectively, and ε_0 is the permittivity of free space. Equation 2.2 is referred to as the cold non-relativistic wave breaking field [80]. For example, using a plasma density of $n_e = 10^{18} cm^{-3}$, it is found that the accelerating gradient is $E_0 \simeq 96\ GV/m$, which is approximately three orders of magnitude higher than that obtained in conventional linacs. Experiments based on laser plasma accelerators have shown an accelerating gradient of the order of $100 GV/m$ [3,105]. In order to achieve such a high accelerating gradient, a high power laser is needed. Using CPA, it is possible to achieve high enough energy by simply stretching and recompressing the pulse. Once that the laser pulse is compressed, it can travel in vacuum and be focused to a few tens of μm spot size. If the laser is focused into a neutral gas (such as helium), self-ionisation can occur and, due to the ponderomotive force, electrons can be expelled and accelerated to ultra-relativistic energies. In this section, what happens in the small region of interaction between the laser and the gas will be described, starting with a plasma.

A plasma can be thought of as a fluid of positively and negatively charged particles, generally created by heating a gas. If there are no external fields, the plasma will be macroscopically neutral. But if an external electric field is applied, the plasma will separate, and the charged particles will move with respect to the external field. If a particle is injected into such a plasma, it would be accelerated by the charge separation; however, since the magnitude of this separation is generally similar to that of the external field, nothing is gained in comparison to a system that simply applies the field directly to the particle, which is the case in existing accelerator designs.

What makes the system potentially useful is the possibility of introducing waves of very high charge separation that travel through the plasma. Such a wave can be created by applying a high-power laser into a properly prepared plasma. As this driving beam travels through the plasma, its electric field separates the electrons and ions in the same way that an external field would. However, as the electrons are much lighter than the ions, they move much further during this short period,

leading to a charge separation as in the case of an external field. As the driving laser beam leaves the vicinity, the electrons are pulled back toward the centre by the now-remaining positive charge of the ions that did not move. As they "fall" into this positive area they pick up speed, so when they reach the centre they "pile up" briefly before losing this energy in collisions and eventually flattening out into a more even distribution.

Even if the particles are not moving very quickly during this period, macroscopically it appears that a "bubble" of charge is moving through the plasma at a speed close to the speed of light. The bubble is the region cleared of electrons that is positively charged, followed by the region where the electrons fall back into the centre and is thus negatively charged. This leads to a small area of very strong potential gradient following in the wake the driving beam.

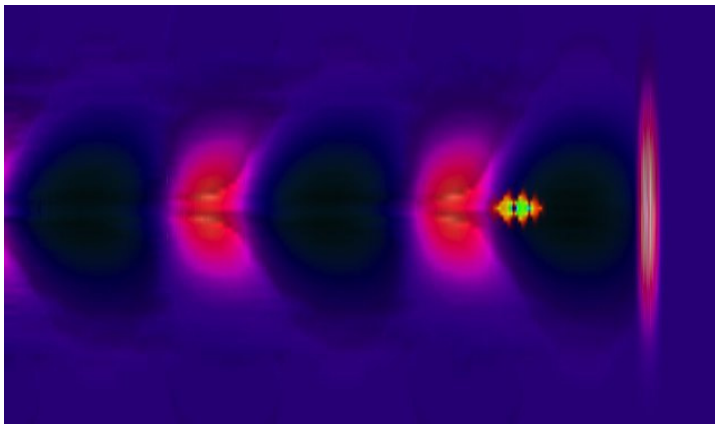

Figure 2.2: Wake created by a laser beam in a plasma [106].

It is this "wakefield" that is used for particle acceleration (see fig. 2.2). A particle injected into the plasma near the high-density area will experience an acceleration toward (or away) from it, an acceleration that continues as the wakefield travels through the column, until the particle eventually reaches the speed of the wakefield. It is possible to reach even higher energies if the particles are injected to travel across the face of the wakefield, much like a surfer can travel at speeds much higher than the wave they surf on by travelling across it. Accelerators that take advantage of this technique have been referred as "surfatrons" [107].

2.3.1 Dephasing and pump depletion

Consider an electron accelerated by a laser beam along the z axis (laser-propagation axis) by a linear electrostatic plasma wave of the form $E_z = E_{\max} \sin\left[\omega_p \left(z/v_p - t\right)\right]$. While the electron is accelerated, its velocity will increase and approach the speed of light, $v_z \to c$. If the phase velocity of the plasma wave is constant with $v_p < c$, the electrons will eventually outrun the plasma wave and move into a phase region of the plasma wave that is decelerating. This limits the energy gain of the electron in the plasma wave and is commonly referred to as electron dephasing [112].

The dephasing length L_d is defined as the length the electron must travel before its phase slips by one-half of a period with respect to the plasma wave. Therefore, the dephasing length is the length needed for a particle to oscillate on the orbit where there is the maximum acceleration (the so-called $\gamma_{\max}$ orbit [112]). In order to find those values, the 1D equation for single particle motion can be written as:

$$\frac{d}{cdt} u_z = \frac{\partial}{\partial z} \Phi \qquad [2.3]$$

where $\Phi = \Phi_0 \cos k_p \left(\tilde{z} - v_p t\right)$ and where $\tilde{z} = \tilde{z}(t)$. Considering now that the laser pulse and the plasma do not move together in time because the laser pulse moves at a group velocity that is close to the speed of light c but is not exactly the speed of light, the equation for the total energy of the system is described by the Hamiltonian written as:

$$H = \gamma - \beta_p u - \Phi \qquad [2.4]$$

where $\gamma = \left(1 + u^2\right)^{1/2}$. Using this equation and solving the differential equation, the following solution is found:

$$u_z = \beta_p \gamma_p^2 \left(H + \Phi\right) \pm \gamma_p \left[\gamma_p^2 \left(1 + \Phi\right)^2 + 1\right]^{1/2}. \qquad [2.5]$$

If now only the laser front is considered, a fluid model (H=1) can be used yielding the solution shown in fig. 2.3 [108].

In fig. 2.3 the solid curve represents the separatrices which separate the flying particle from the trapped particle inside the bubble. The maximum energy [108] will be given by:

$$\gamma_{\max} = 4\gamma_{phase}^2 \Phi = 4\left(\frac{\lambda_0}{\lambda}\right)^2 \frac{E_z}{E_0} \qquad [2.6]$$

where Φ is the amplitude of the wave.

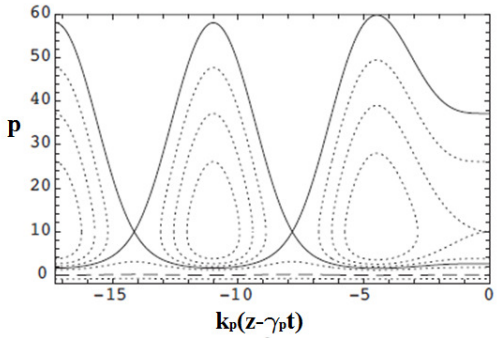

Figure 2.3: Single particle orbits in phase space for an electron in a small amplitude sinusoidal plasma wave. Dashed curve is the cold fluid orbit. Solid curve is separatrix [108].

To quantify the dephasing length, let's introduce the slippage $L_d\left(1-\frac{v_p}{c}\right)$ and let's assume that this slippage is $L_d\left(1-\frac{v_p}{c}\right)=\frac{\lambda_p}{2}\frac{2\lambda_p^2}{\lambda^2}$. In this way, it is found that the dephasing length [109] is:

$$L_d = \frac{\lambda_p^3}{\lambda^2} = \gamma_p^2 \lambda_p . \qquad [2.7]$$

Once the dephasing length is known, the maximum energy gain after a dephasing length can be established. This will be easily given by:

$$\Delta E \simeq eE_{\max} L_d \simeq 2\pi\gamma_p^2 \left(E_{\max}/E_0\right) m_e c^2 \qquad [2.8]$$

assuming $E_{\max} < E_0$. So, for example, a density of $10^{18} cm^{-3}$ gives a maximum energy gain of $\gamma_{\max} = 6400$ which corresponds to an electron energy of 3.2 GeV.

Another factor, together with the dephasing process, that can limit the single stage energy gain is laser pump depletion. The pump depletion length L_{pd} can be estimated by equating the laser pulse energy to the energy left behind in the wakefield:

$$E_z^2 L_{pd} = E_L^2 L \qquad [2.9]$$

where E_L is the laser field.

If it is assumed that the LWFA is driven by a linearly polarised square profile laser pulse with $L \simeq \lambda_p / 2$ (1D limit), then the dephasing length and the pump depletion length are given by:

$$L_d \simeq \frac{\lambda_p^3}{2\lambda^2} \times 1 \quad for\ a_0^2 \ll 1 \qquad [2.10]$$

$$L_d \simeq \frac{\lambda_p^3}{2\lambda^2} \times \left(\sqrt{2}/\pi\right) a_0 \Big/ N_p \quad for\ a_0^2 \gg 1 \qquad [2.11]$$

$$L_{pd} \simeq \frac{\lambda_p^3}{\lambda^2} \times 2/a_0^2 \quad for\ a_0^2 \ll 1 \qquad [2.12]$$

$$L_{pd} \simeq \frac{\lambda_p^3}{\lambda^2} \times \left(\sqrt{2}/\pi\right) a_0 \quad for\ a_0^2 \gg 1 \qquad [2.13]$$

where a_0 is the normalized laser amplitude and N_p is the number of plasma periods behind the drive laser pulse. In eq. [2.10] and [2.11], the factor $\lambda_p^3 / 2\lambda^2$ arises from requiring a highly relativistic electron (travelling at the speed of the light) to phase slip by $\lambda_p / 4$ (since only a quarter of a plasma wave period is both accelerating and focusing). In the $a_0^2 \gg 1$ limit of eq. [2.11], the factor $1/N_p$ relates to the plasma wave period increasing as the laser pulse steepens, which is the dominant effect in determining the plasma wave phase velocity in the nonlinear limit.

In the linear regime $\left(a_0^2 \ll 1\right), L_d \ll L_{dp}$ and the electron energy gain is limited by dephasing, not pump depletion, assuming an axially uniform plasma. However, by appropriately tapering the axial plasma density profile, dephasing limitations could be overcome, resulting in a larger single-stage energy gain [110-111].

The ideal energy gain in a standard LWFA can be estimated by $\Delta W = eE_z L_{acc}$, where L_{acc} is the acceleration length and $E_z = E_0\left(a_0^2/2\right)\left(1+a_0^2/2\right)^{-1/2}$ is the maximum electric field amplitude driven by an optimised flat-top, linearly polarised pulse in the 1D limit [17,112]. If the acceleration distance is limited by diffraction, $L_{acc} \simeq \pi Z_R < L_d, L_{dp}$, the energy gain is:

$$\Delta W_R\left(MeV\right) \simeq 740\left(\lambda/\lambda_p\right)\left(1+a_0^2/2\right)^{-1/2} P\left(TW\right) \qquad [2.14]$$

If the acceleration distance is limited by dephasing, $L_{acc} \simeq L_d$, the energy gain is:

$$\Delta W_d\left(MeV\right) \simeq \frac{630 I\left(W/cm^2\right)}{n\left(cm^{-3}\right)} \times 1 \quad for\ a_0^2 \ll 1 \qquad [2.15]$$

$$\Delta W_d\left(MeV\right) \simeq \frac{630 I\left(W/cm^2\right)}{n\left(cm^{-3}\right)} \times \left(2/\pi\right)/N_p \quad for\ a_0^2 \gg 1 \qquad [2.16]$$

And, lastly, if the acceleration distance is limited by depletion, $L_{acc} \simeq L_{pd}/2$, the energy gain is:

$$\Delta W_{pd}\left(MeV\right) \simeq 3.4\times 10^{21} \Big/ \left[\lambda^2\left(\mu m\right) n\left(cm^{-3}\right)\right] \quad for\ a_0^2 \ll 1 \qquad [2.17]$$

$$\Delta W_{pd}\left(MeV\right) \simeq 400 I\left(W/cm^2\right) \Big/ n\left(cm^{-3}\right) \quad for\ a_0^2 \gg 1 \qquad [2.18]$$

These equations are valid with the idealised assumptions made above and neglecting various non-ideal effects, such as self-focusing and laser-plasma instabilities. Moreover, for the above equations, the laser pulse is assumed to be broad $\left(k_p^2 r_0^2 \gg 1\right)$ propagating in a density channel that supports guiding. For sufficiently high powers $P \gg P_c$ (where P_c is the critical power), it can be possible to guide the laser pulse over multiple Rayleigh lengths without the use of a density channel due to a combination of relativistic self-focusing and ponderomotive self-channelling (section 2.2.2).

Although ΔW is limited by depletion and dephasing for both a channel-guided LWFA (when gas has been externally ionized and the laser only drives the plasma waves) or a self-guided LWFA (when the laser both ionizes the gas and drives the plasma waves) with $P \gg P_c$, there may be additional advantages to using a channel

instead of relying on self-guiding. One difference is that the additional constraint $P \gg P_c$ needs not be satisfied when using a channel. This implies that the channel-guided LWFA may be operated at lower intensities (lower a_0), which may be a more stable regime. Also the channel may provide some resistance to instabilities. Without the channel, the laser pulse will be subject to some amount of diffractive erosion since the head of the pulse will not be self-guided, which can limit the propagation distance.

2.3.2 Self-injection of electrons

Self-injection is a non-linear effect that occurs during the laser-gas propagation at laser powers above the critical power and which is useful to give rise to linear self-focusing of the laser beam in gas. The use of this non-linear effect for the electron beam production eliminates the need for an external injector like a RF gun [113].
As described above, the dynamics of an electron in the presence of a plasma wave and a laser pulse are determined by the Hamiltonian in the co-moving frame:

$$H = \left(\gamma^2 + p^2\right)^{1/2} - \beta_p p - \varphi. \qquad [2.19]$$

The orbit of an electron with initial normalised momentum p_t will then be defined by:

$$H = \left(\gamma^2 + p_t^2\right)^{1/2} - \beta_p p_t = H_t. \qquad [2.20]$$

Trapping (or self-injection) of the electron will occur when the orbit defined by H_t coincides with a trapped orbit defined as lying within the separatrix orbit (Fig. 2.3), defined by H_s when $H_t \le H_s$. Solving $H_t = H_s$ it is found that the minimum initial electron momentum for trapping in the plasma wave [114] is given by:

$$p_t = \gamma_p \beta_p \left(\gamma_\perp - \gamma_p \varphi_{\min}\right) - \gamma_p \left[\left(\gamma_\perp - \gamma_p \varphi_{\min}\right)^2 - 1\right]^{1/2} \qquad [2.21]$$

where $\varphi_{\min}$ is the minima of the plasma wave potential. The threshold momentum required for trapping decreases for larger plasma wave amplitude and for lower

plasma wave velocity. Curvature of the plasma wave fronts in two dimensions can enhance trapping into the focusing and accelerating regions [114].

As the driver propagates into the plasma, more charge will be trapped until the amplitude of the wave is substantially reduced due to beam loading (see next section for details). The beam loading limit is defined as the number of the accelerated electrons required to produce a wakefield that cancels the accelerating field of the plasma wave [115].

2.4 Electron beam quality

The quality of a relativistic electron beam used as a radiation source driver in a synchrotron or FEL light source is characterised by two important parameters: emittance and peak current. Longitudinal emittance is related to the energy spread of the beam while the transverse emittance is related to its focusability. Peak current is determined by the beam charge and duration (longitudinal structure). Underpinning all of these properties is the concept of beam loading which can drastically change the quality of the electron bunches exiting the accelerator as well as the number of electrons trapped and accelerated in the wakefield.

2.4.1 Beam loading

The process by which the wake produced by the accelerated bunch significantly modifies the fields of the accelerating plasma wave is referred to as beam loading. Beam loading can place severe limitations on the beam current that can be accelerated, the quality of the accelerated particle bunch, and the efficiency of the plasma-based accelerators. In 1986 Katsouleas et al. [110] gave a very interesting explanation of this effect. They found the limits on the beam radius, beam number and beam loading efficiency imposed by emittance and energy spread constraints taking into account two different beams: a wide uniform beam and a beam with

arbitrary width. In particular, he showed that the total number of particles that can be accelerated in a relativistic plasma wave, for ultra-short beams is given by:

$$N_0 \cong 5\times10^5 \sqrt{n_0} A_{eff} \frac{n_1}{n_0} \qquad [2.22]$$

where A_{eff} is the effective area of the beam and n_1/n_0 is the normalised wave amplitude (<1). Moreover, it was found that for ultra-short unshaped bunches, the energy spread increases with the number of particles as N/N_0 while the maximum efficiency scales as $N/N_0\left(2-N/N_0\right)$.

Katsouleas et al. also argued that by employing special shapes for the bunches (so that all the particles in the bunch feel the some accelerating field), the energy spread can be reduced, and the contributions to it will only be phase slippage, shaping errors and transverse field variation. Emittance requirements may also restrict the radius of the accelerating beam. To meet this requirement while keeping the beam loading efficiency from becoming too low [115,116], they considered waves of width c/ω_p and narrow beams. It was calculated that, in this case, the effective area of the beam becomes of the order of c^2/ω_p^2. The beam loading efficiency that results for mismatched beam and wave cross section is illustrated for two cases in fig. 2.4.

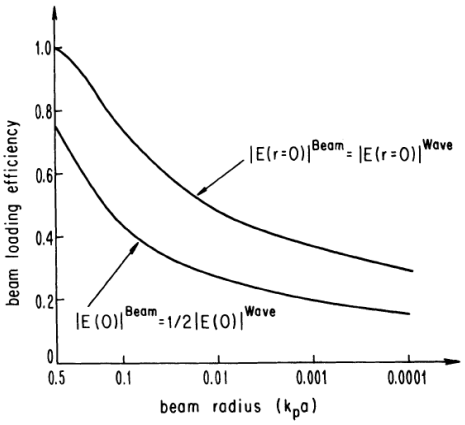

Figure 2.4: Beam loading efficiency as function of the beam radius in a wave of diameter c/ω_p. The upper curve represents an ultra-short beam with $N = N_0$ electrons, while the lower curve can represent both a short beam with $N_0/2$ electrons or a shaped beam with $3N_0/4$ electrons [116].

Another important result was that the overall efficiency of the accelerator depends on the efficiency of the free energy source and the efficiency of converting the source energy into plasma waves.

2.4.2 Energy spread and emittance

The self-injection and acceleration scheme of the laser wakefield accelerator is ideally suited for the formation of the electron beams with low energy spread and low emittance.

Consider once again the separatrix curve of fig. 2.3. There is a region, under the solid curve defining the separatrix, where the fluid model is valid. Two different regions can be distinguished: an accelerating region from $-\pi$ to 0 and a decelerating region from 0 to π. Therefore, the electron beam should be in the left part of the curve to be accelerated and should not reach the decelerating right part of the curve. At $-\pi$ and π there are no net forces (those points correspond to the maximum of the sinusoidal fluid model curve) and, as far as the separatrices are concerned, these are the unstable points.

So the electron beam should arrive just after $-\pi$, be trapped in one of the orbits marked with the dashed curves and leave the bubble just before the deceleration process starts (the 0 point).

To get the electron trapped inside the separatrix and let it oscillate inside the oval curves (which correspond to different electron energies), it is necessary to accelerate the beam, break the wake and trap all the electrons inside the bubble.

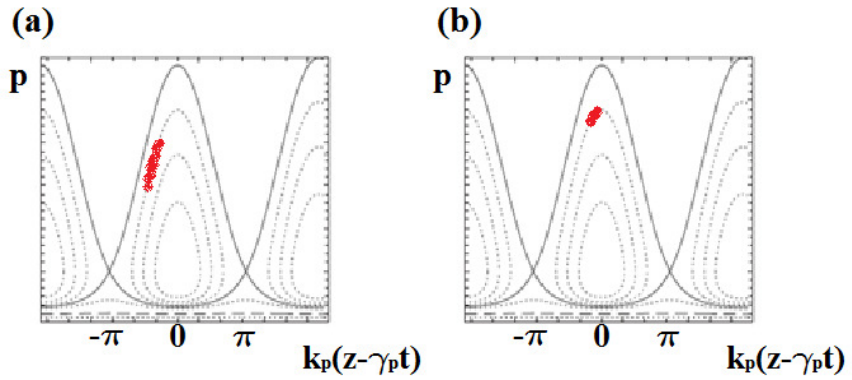

Figure 2.5: Cold fluid orbits and separatrices with an injected electron beam. (a) electron beam with large energy spread and emittance far from the dephasing point; (b): electron beam with low energy spread and emittance close to the dephasing point.

To obtain beams with low energy spread and emittance, the electrons should leave the bubble just before or exactly at the dephasing point, which is the point of maximum in the separatrix curve. The images in fig. 2.5 show clearly that, if the electrons exit the bubble too early, the overall electron beam (particles in red) has a high energy spread and emittance (the y axis is in fact the momentum) while just before or at dephasing, (or just after), the beam is more confined in momentum which means that the energy spread and the emittance are minimal. Once the particles cross the dephasing point, they will start to feel a deceleration force and the beam will spread again, causing a growth in emittance and energy spread.

2.4.3 Bunch length

From fig. 2.5, it can be seen that if the bunch exits the bubble significantly before dephasing, the bunch has a very high momentum spread. Because the momentum is proportional to the velocity, it is clear that, in the case of fig. 2.5a, then the bunch will have a long length/duration while, in the case of fig. 2.5b, the momentum spread is smaller (the x axis represents the longitudinal spatial coordinate), because higher velocity electrons will act to move. This difference in bunch length is worsened by the velocity spreading of the beam caused by the higher velocity electrons at the head of the beam moving farther out in front and, likewise, lower

velocity electrons at the rear trailing behind progressively more. The shorter the momentum spread, the shorter will be the bunch duration exiting the accelerator, i.e. accelerating up to but not beyond the dephasing point impacts strongly on the bunch length as well as the energy spread and emittance.

2.4.4 Charge and peak current

The other important factors regarding the quality of the electron bunches are the charge and the peak current. The charge Q is simply the number of electrons in the bunch times the electron charge *e*, while the peak current is related to the charge and the bunch duration of the electron beam as follows:

$$I_{beam} = Q/t\,. \qquad [2.23]$$

In order to get a high charge from the accelerator, the trapping of electrons inside the bubble needs to be maximised, while to have a high peak current, it is necessary to have a high charge in a minimum longitudinal extend (duration).

Chapter 3

Free-Electron Laser theory and simulations

3.1 Introduction

As outlined in section 1.3.1, Madey proposed that an undulator structure working as an amplifier at optical wavelengths could replace the active medium between the mirrors of the laser optical cavity, calling such a device a *free-electron laser*.

In 1979 Madey [117] gave much greater generality to his quantum-mechanical gain formula by being able to show that gain of an undulator used as an amplifier is proportional to the derivate with respect to the electron energy (or, within an acceptable approximation, with respect to the radiation frequency) of its spontaneous emission, a result which has since become known as Madey's theorem [117]. In particular, Madey proved that, to second order in perturbation theory:

$$\left\langle \mathscr{E}_f - \mathscr{E}_i \right\rangle = \frac{1}{2}\frac{\partial}{\partial \mathscr{E}_i}\left\langle \left(\mathscr{E}_f - \mathscr{E}_i\right)^2 \right\rangle \qquad [3.1]$$

where $\mathscr{E}_i$ and $\mathscr{E}_f$ are the initial and final energies of an electron, before the entrance and after the exit of the undulator respectively, and angular brackets denote an average over all the electrons in the input beam. Since it can also be shown that $-\left\langle \mathscr{E}_f - \mathscr{E}_i \right\rangle$ is proportional to the stimulated emission and $\left\langle \left(\mathscr{E}_f - \mathscr{E}_i\right)^2 \right\rangle$ is proportional to the spontaneous undulator emission, eq. [3.1] affords a very quick way to calculate the gain which turns out to be approximately proportional to:

$$\frac{d}{dx}\left(\frac{\sin x}{x}\right)^2 \qquad [3.2]$$

Madey derived his theorem just as his previous results, from quantum mechanics.

3.2 Spontaneous undulator radiation

It is well known that when an electron beam changes direction it emits (spontaneous) radiation in a continuous frequency band. The most noticeable example is the intense radiation produced by electrons in a synchrotron orbit. In

many facilities, this synchrotron radiation, channelled tangentially out from the accelerator, is used in solid state physics, chemistry, biology, etc. for experiments needing intense X-ray illumination [118]. It is sometimes concentrated in a certain frequency range by oscillating the beam as it leaves the machine with the help of magnets so as to follow a shape like the outline of a camel's back. This kind of device is called an undulator or wiggler depending on the magnetic field applied to the particle. In an undulator, the magnetic field is low and the deflection of the electrons from the main axis is small, while in a wiggler, the magnetic field applied to the particle is high and the deflections are large. The use of these devices help to concentrate the radiation spatially in a narrow cone and spectrally in a narrow frequency interval.

In the simplest case the undulator structure consists of a succession of magnet pairs of alternating polarity, as illustrated in fig. 1.

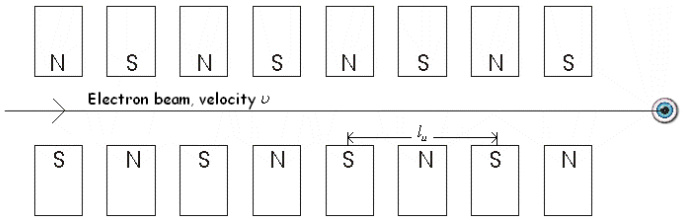

Figure 3.1: The basic planar undulator structure.

With proper pole pieces, the magnetic field near the axis is very nearly sinusoidal; the spatial period of the sine wave will be nominated l_u. The exact determination of the orbits of high-energy electrons of velocity υ passing between the pole pieces leads to near-sinusoidal orbits in a plane perpendicular to that of the figure.

The particularity of the spontaneous undulator radiation is that the amount of the power radiated even by a very energetic beam of electrons is not large. Indeed, if the electrons were spaced uniformly along the beam, there would be no power emitted at all: when the beam has a steady current, for each electron emitting radiation with a given phase, there is another which radiates a field exactly out of phase, so that the two fields null each other. Incoherent radiation arises because

the current is not exactly uniform – it is the fluctuations in particle current or density which account for the net radiation and it is well known that the mean-square size of these fluctuations is proportional to the average electron density [119]. Hence the rms radiation field strength scales as $n^{1/2}$ rather than n and the incoherent net power radiated scales as n. If the electrons spend an infinite amount of time in the undulator, the spectrum would be a delta function at the wavelength given by:

$$\lambda_r = \frac{1}{2\gamma^2}\left(1 + a_u^2\right) \qquad [3.3]$$

where γ is the electron beam relativistic factor (or Lorentz factor) and a_u is the dimensionless undulator parameter, defined as:

$$a_u = \frac{e}{mc^2}\frac{\lambda_u B_u}{2\pi} \qquad [3.4]$$

where λ_u is the undulator period, B_u is the magnetic peak field of the undulator, m and e are the mass and charge of the electrons respectively.

However, the electron experiences only *N* periods in the finite undulator of length $L = Nl_0$. There is, therefore, a finite transit time $t = L/\beta_{//}c$, where $\beta_{//}$ is the electron motion along the axis, $v_{//}/c$, and the power spectrum is broadened when the Fourier transform is extracted. Using the approach in Jackson's text [120], the power spectrum varies as:

$$\frac{\sin^2\left(N\pi\xi\right)}{\xi^2} \qquad [3.5]$$

where:

$$\xi = \left[\frac{\omega}{k_0 c}\left(1 - \beta_{//}\cos\vartheta\right) - 1\right] = \left(1 - \frac{\lambda_r}{\lambda}\right) = \left(1 - \frac{\gamma_r^2}{\gamma^2}\right) \qquad [3.6]$$

in which λ_r is the resonant wavelength for a given energy γ, and γ_r is the resonant energy for a given wavelength λ. This is the spectrum of the spontaneous or noise radiation and it has a fractional width $\sim 1/N$.

3.3 Principle of FEL operation

The principle of work of an FEL will be described here. This consists firstly of the high-gain theory, which explains the mechanism needed to reach exponential growth of the radiation and Self-Amplified Spontaneous Emission (SASE), which is the process to amplify spontaneous emission starting from noise. Then the electron beam criteria, which defines the limitations in electron beam quality for an operating FEL will be described. Finally, the two-wave model, which is of fundamental importance in order to understand the slippage processes, is analysed.

3.3.1 High-gain theory

The theory of the high-gain regime for a single pass FEL is analysed here and it is shown that the phase bunching mechanism can lead to exponential radiation production. The high-gain mechanism is an instability which can occur with appropriate beam parameters. One of the features of the high-gain regime is that the electrons in the beam affect one another via the radiation field.

A single-pass FEL can be represented by: accelerator, beam optics, undulator, optical beam, electron beam dump and optical diagnostic, as shown in fig. 3.2.

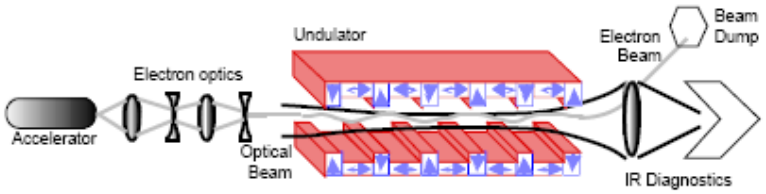

Figure 3.2: Schematic representation of a single-pass FEL.

To study the FEL theory, it is not necessary to consider the acceleration process or electron beam transport up to the undulator entrance. The electron beam will be considered as a collection of particles and the undulator as a device that produces a periodic magnetic field. Of course, since the beam transport is not taken into

account, the beam at the undulator entrance has to be described as fully as possible. This can be done simply by describing the beam momenta and position (six-dimensional phase space) of the electron beam, i.e., the beam is represented by macroscopic parameters: transverse emittance, beam current, longitudinal energy and FEL phase. Usually an undulator is described by the period λ_u, the magnetic field strength B_u, the total length L_u and the gap (magnet separation) g. In reality it is not necessary to proscribe both the magnetic field strength B_u and the gap height g, because they are related by the formula:

$$B_u = 1.55 e^{-\pi g/\lambda_u}. \qquad [3.7]$$

and λ_u is defined in eq. [3.4].

Here other important parameters that will be involved in the following discussion will be defined. The first parameter is the modified relativistic plasma frequency:

$$\omega_p = \left(n_e e^2 / \varepsilon_0 m_e\right)^{1/2}. \qquad [3.8]$$

Then there is the universal FEL parameter:

$$\rho = \frac{1}{\gamma_r}\left[\frac{a_u \omega_p}{4 c k_u}\right]^{2/3} \qquad [3.9]$$

first introduced by Bonifacio [121]. The last parameter is the energy detuning parameter:

$$\delta \equiv \frac{\gamma_0^2 - \gamma_r^2}{2\gamma_r^2 \rho}; \qquad [3.10]$$

which refers to behaviour in an FEL oscillator where an input energy γ_0 tunes the FEL wavelength away from resonance.

Following the Bonifacio et al. paper [121] and introducing the variables:

$$X = \left\langle \delta\vartheta_i e^{-i\Psi_{0j}} \right\rangle \qquad [3.11]$$

$$Y = \frac{1}{\rho}\left\langle \eta e^{-i\Psi_{0i}} \right\rangle \qquad [3.12]$$

$$\Psi_{0i} = 2\pi(i-1)/n_e \qquad [3.13]$$

$$\eta_i \equiv \frac{\gamma_i - \gamma_r}{\gamma_r} \qquad [3.14]$$

$$\tau \equiv 2ck_u\rho\left(\frac{\gamma_r}{\gamma_0}\right)^2 t \qquad [3.15]$$

the linearised, collective FEL equations can be written as:

$$\frac{dX}{d\tau} = Y + i\rho A \qquad [3.16]$$

$$\frac{dY}{d\tau} = -A \qquad [3.17]$$

$$\frac{dA}{d\tau} = -i\delta A - iX - \rho Y \qquad [3.18]$$

and the above equations can be solved by assuming solutions of the form $e^{i\lambda\tau}$ to yield the characteristic equation:

$$\lambda^3 - \delta\lambda^2 + \rho\lambda + 1 = C \qquad [3.19]$$

whose roots provide the characteristics of the FEL interaction. Those roots need to be negative imaginary in order to have exponentially growing solutions which therefore means that now the problem is to find the conditions under which the exponential growth occurs.

The detuning component $\delta\lambda^2$ of eq. [3.19] is actually misleading for a single-pass, high-gain FEL since the energy of the beam is, by definition, the resonant energy. The detuning term is relevant for determining the width of the gain versus energy curve and not in understanding the peak growth rate of the instability. By neglecting this term in the characteristic equation, the maximum growth rate occurs when $\mathrm{Im}\,\lambda = \sqrt{3}/2$ for $\rho < 0$. This significant result means that the exponentially growing part of the field as a function of the distance down the undulator, is given by:

$$|A| \propto \exp\left(\frac{4\pi\rho}{\lambda_u}\frac{\sqrt{3}}{2}z\right). \qquad [3.20]$$

Therefore the exponential power gain length (which is proportional to $|A|^2$) depends on the FEL parameter as:

$$L_g = \frac{\lambda_u}{4\sqrt{3}\pi\rho} \qquad [3.21]$$

and the total unsaturated power gain is simply related to the number of undulator periods, N_u :

$$G = 4\pi\sqrt{3}\rho N_u . \qquad [3.22]$$

The unsaturated power growth can be expressed as:

$$P(z) = P_0 e^{z/L_g} \qquad [3.23]$$

where P_0 is the initial power within the bandwidth and angular acceptance of the FEL.

There are two interesting regimes as shown in fig. 3.3: the start-up regime that occurs at the beginning of the FEL where the instability (the growing exponential) has not yet dominated over the decaying exponential and the linear terms. Then there is the saturation, which occurs when the nonlinear forces damp the instability. Usually saturation occurs at 10 or 11 power gain lengths after the beginning of the undulator. In reality, the saturation length is dependent on the FEL parameter and the number of gain length within the saturation length can vary depending on the device.

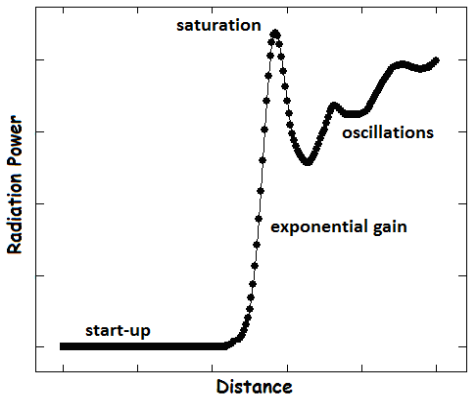

Figure 3.3: Power growth in the FEL showing the start-up from a small signal input, the exponential growth and saturation.

3.3.2 Self-amplified spontaneous emission

Starting an FEL from noise relates to the process of amplifying the spontaneous emission produced by the beam in the undulator: so-called Self Amplified Spontaneous Emission (SASE). To model SASE, theoreticians have introduced a scale length, called the cooperation length, over which microscopic variations are averaged by the FEL [117]:

$$L_c = \frac{\lambda_r}{4\pi\rho}. \qquad [3.24]$$

The cooperation length is in fact the amount of slippage that occurs in a gain length and describes the interplay between gain and slippage effects: it determines the scale over which the slippage tends to smooth out any non-uniformity along the radiation. If the initial noise exhibits fluctuations on a smaller length scale, the slippage process tends to smooth these variations on a scale length $\sim L_c$. The cooperation length can therefore be thought of as a measure of the portion of the electron beam sampled by the FEL process during a gain length.

The model of the SASE FEL is relatively simple: the first gain length of the undulator can be thought of as the spontaneous radiator. A portion of the spontaneous emission produced in the first gain length is amplified by the reminder of the undulator, as shown in fig. 3.4. The result is a partially coherent output signal. It has already been shown that an FEL has a limited bandwidth and a limited acceptance angle: the FEL will only amplify a signal which lies within the bandwidth and coherence angle comprised of the remainder of the undulator.

The process of Self-Amplified Spontaneous Emission can be seen as one that permits the start-up at arbitrary wavelengths without the need for an external seed radiation signal.

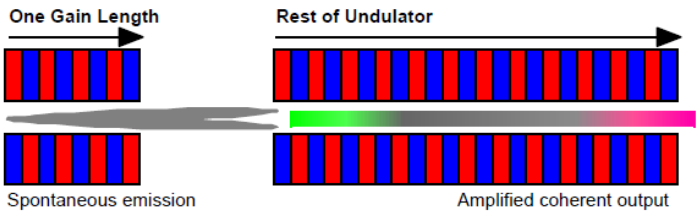

Fig. 3.4: SASE FEL model: the spontaneous emission produced in the first gain length is amplified by the remainder of the undulator.

The SASE FEL is based on the random phase factors, ϑ_l, of the electrons in the ensemble at the beginning of the undulator, resulting in a broadband spectrum for the spontaneous emission (undulator radiation) as the seeding signal. The SASE FEL not only drives the radiation at the resonance frequency, but it also amplifies all frequencies within the acceptance bandwidth of the FEL [119]. The relative bandwidth of the SASE FEL under standard conditions of single transverse mode excitation is given by the FEL parameter ρ, typically on the order of $10^{-2}-10^{-3}$ at VUV or X-ray wavelengths.

The initial ponderomotive phase of the electrons in the ensemble is random, therefore, the electrons will group together randomly. The emitted radiation from these random groups will be dominated by the groups with the most electrons. These fluctuations lead to variations in beam current and are also present in the output radiation energy. Since the SASE FEL starts from the shot noise in the electron beam, the output energy distribution also displays fluctuations that follow the gamma distribution. In this statistical treatment of the SASE FEL, the gamma probability distribution of the radiation energy has a dependence on the number of modes in a radiation pulse (denoted by M).

The explicit value of M is determined by the slippage in the SASE FEL. If the electron bunch length is longer than the slippage, $N_u\lambda$, the radiation's temporal distribution is comprised of numerous modes. The modes, or spikes, originate from the random noise variations in the beam current and the intensity fluctuations follow a gamma distribution.

3.3.3 Electron beam criteria

The electron beam needs to be of sufficient quality in order to enable bunching on the scale of the radiation wavelength thus driving the FEL process. The first beam criterion under consideration is the current which should be as large as possible to maximise the gain parameter ρ (eq. [3.9]). In order to successfully operate an FEL, a high peak current is required, typically a few kA [122]. The current is simply the ratio of the bunch charge over the bunch duration so it will decrease if the electron bunch lengthens. One effect that can vary the length of the bunch is the longitudinal space charge that will tend to lengthen the pulse with increased current (see Chapter 4) and reduced charge weakens this effect.

Being able to vary the beam current is a way to investigate the FEL operation; in fact varying the current is analogous to varying the length of the undulator that the beam traverses. With a shorter bunch length, the bunch sees an undulator that is much longer and therefore, the gain length becomes shorter. Likewise, with increased charge, the beam current increases and again the gain length (eq. [3.21]) becomes shorter (effectively changing the undulator length). In the SASE FEL model, the shorter gain length means there will be more electrons to contribute to the spontaneous emission and, again, if the gain length is shorter, the electrons will effectively see a longer undulator.

Another important beam criterion to satisfy is related to the electron beam size. Injecting the beam into the undulator with an incorrect beam size causes a mismatch with respect to the natural focusing in the non-wiggle plane. In the wiggle plane, the envelope will evolve ballistically (neglecting the space charge), causing a lower average density through the undulator. Usually mismatches in the beam envelope in the non-wiggle plane are fairly negligible when the mismatch Δy is $\leq 10\%$ (envelope oscillation amplitude compared to the nominal beam envelope). A larger mismatch will degrade the FEL performance. An estimation of the mismatch can be made by requiring that the error in the beam size $\Delta\sigma$ be much smaller than the nominal beam size (σ_{nat}):

$$\Delta\sigma < \sigma_{nat} = \sqrt{\frac{\sqrt{2}\varepsilon_n \lambda_u}{2\pi k_u}}, \qquad [3.25]$$

where ε_n is the normalised emittance. Another limit on FEL operation concerns the bandwidth. In fact, it is known that the exponential growth of the FEL drops to zero when the detuning parameter exceed ~ 2 [123], which means that, to have exponential growth:

$$\frac{\gamma_0^2 - \gamma_r^2}{2\gamma_r^2 \rho} < 2 \quad \Rightarrow \quad \frac{\Delta\gamma}{\gamma_r} < 2\rho \qquad [3.26]$$

and, by using the resonant condition, the limit on the bandwidth emerges as:

$$\frac{\Delta\omega}{\omega_r} < 4\rho \,. \qquad [3.27]$$

Two considerations arise from these equations; firstly, if the beam has an energy spread larger than $\sim 2\rho$ then the high-gain FEL performances will be greatly reduced from the ideal (no energy spread) case. Secondly, if an input signal has a frequency spread (bandwidth) greater than $\sim 4\rho$, only a portion of the signal (the frequencies within the FEL bandwidth) will be significantly amplified. The bandwidth spread also influences the angular acceptance of the FEL and to calculate the angular acceptance, the wavelength radiation as a function of the observation angle can be introduced:

$$\lambda_r(\vartheta) \cong \frac{\lambda_u}{2\gamma^2}\left(1 + a_u^2 + \gamma^2\vartheta^2\right) \qquad [3.28]$$

and the angular acceptance (or coherent angle) can now be estimated by inverting the above relation to obtain:

$$\vartheta_{ca} = \frac{2}{\gamma_r}\sqrt{\left(1 + a_u^2\right)\rho} \qquad [3.29]$$

The *coherence angle* determines the largest angle of radiation which can be incident upon the undulator and still be amplified by the FEL: in fact, the coherence angle is directly related to the gain bandwidth of the FEL.

The FEL efficiency can be expressed as:

$$\eta \equiv \frac{\gamma_0 - \gamma}{\gamma_0} = \frac{\Delta\gamma_0}{\gamma_0} \approx \rho \quad , \qquad [3.30]$$

where it is assumed that the difference between the initial and the final energy of the electron beam is the largest energy spread allowed by the FEL. Under this assumption, the conservation of the energy may be extended to the conservation of the power. The power lost in the electron beam is equal to the power gained by the optical beam, so the saturated optical power is given by:

$$P \simeq \rho P_b = \rho I_b mc^2 \gamma / e \qquad [3.31]$$

$$B_L = \frac{eN_b}{2\pi\gamma\sigma_z\sigma_E} \qquad [3.32]$$

$$I_A = \frac{mc^3}{e} \qquad [3.33]$$

$$k_1 = \frac{\rho}{\sigma_E} \qquad [3.34]$$

$$k_2 = \frac{4\pi\varepsilon_n}{\gamma\lambda_r} \qquad [3.35]$$

$$k_3 = \frac{\beta}{L_g} = \frac{4\pi\rho\beta}{\lambda_u} \qquad [3.36]$$

where B_L is the longitudinal beam brightness, I_A is the Alfven current, k_1, k_2 and k_3 are constants, ε_n is the normalised emittance, β is the beta function (Rayleigh length) and λ_u is the undulator period.

Using these parameters, it is possible to find a more precise equation for the FEL parameter respect to eq. [3.9], since now electron beam parameters has been taken into account. The new equation can be expressed as:

$$\rho = \frac{1}{k_1 k_2 k_3} \frac{a_u^2}{\left(1 + a_u^2\right)^2} \frac{B_L}{I_A} \quad . \qquad [3.37]$$

A bunching parameter can be estimated by taking advantage of the collective variable description. From the exponential grow of the field, it is expected that other parameters in the FEL instability might have an exponential behaviour: the

most important is the scaled bunching parameter, since it is directly related to the field by:

$$b(z) \approx \sqrt{\frac{\sqrt{2\pi}\sigma_z}{\rho e N_b \gamma m c^3} P_0 e^{z/L_g}} \qquad [3.38]$$

where P_0 is the start-up power of the FEL.

A number of beam criteria can be summarised at this stage:

1. Detuning parameter: $\frac{\Delta\gamma}{\gamma_r} < 2\rho$ (which is related to the limitation in energy spread)
2. Bandwidth: $\frac{\Delta\omega}{\omega_r} < 4\rho$
3. Energy spread: $\sigma_E \tilde{<} \rho$
4. Rayleigh range: $Z_R \tilde{>} L_u$ since the Rayleigh length must be of the order or longer than the undulator length so that the diffraction effects can be safely ignored. The Rayleigh length can also be related to the gain length: $Z_R \tilde{>} L_g$
5. Beam emittance: $\varepsilon_{beam} < \varepsilon_{optical} \Rightarrow \varepsilon_N \tilde{<} \lambda_r \gamma$. This limitation is analogous to ignoring diffraction and it is assumed that the radiation emittance is $\simeq \lambda_r$. This limit mainly means that the electron beam and the optical beam overlap well in phase space. However, this limit is rarely significant, and this will be clear while looking at the scaling. In fact, the beam emittance scales as the inverse of the beam energy, while the radiation emittance scales as the radiation wavelength. However, the radiation wavelength scales as the inverse of the beam energy squared (from the resonance equation). Hence, the above emittance limit is only significant for the very high energy case (X-ray regime).

   The limit on the beam emittance can be expressed in terms of external focusing strength such as: $\varepsilon_n \leq \frac{\beta\rho\left(1+a_u^2/2\right)}{2\gamma}$.

Lastly, time-dependent effects must be taken into account. Time-dependence is significant when the relation between the undulator field, radiation field and beam changes explicitly with time and therefore with the distance along the undulator. An example of a time-dependent effect is slippage: when the radiation field slips by the beam bunch a significant amount in the length of the undulator (see section 3.3.4), then time-dependent effects become consequential. Slippage can be ignored when the limit: $\sigma_{beam} \gg L_s = \lambda_r N_u$, where L_s is the slippage length.

In general, time-dependent effects can be ignored when the beam bunch length is much longer than the gain length.

3.3.4 Two-wave model

This model describes the interaction of a single particle (electron) with an optical field and an undulator field; it includes the effect of the slippage, a time-dependent phenomenon introduced above. The model illustrates the forces exerted on the particle by the optical and undulator fields and how it is then driven. Figure 3.5 shows the trajectory of an electron (in black) in an undulator field (the grey arrows) in different stages which also interfere with an optical electric field (in pink).

In frame 1, the electron is off axis and feels no force from the optical field since the electric field is zero: the force is only from the undulator. In frame 2, the electron has advanced ¼ of the undulator period, while the optical field has advanced ¼ of a period relative to the electron: the electric field is now at maximum and the electrons feels a retarding force and radiates. In frame 3, the electron has advanced ½ of the undulator period and the optical field has advanced ½ of a period relative to the electron: the electric field is again zero, so the electron feels no force, and loses no energy. In frame 4, the electric field has reached the maximum: the electron feels a retarding force, but opposite with respect to frame 2, and again loses energy to the optical field. Eventually, in frame 5, the configuration is the same of frame 1, but the optical field has “slipped” one wavelength and has gained energy equal to the energy lost by the electron.

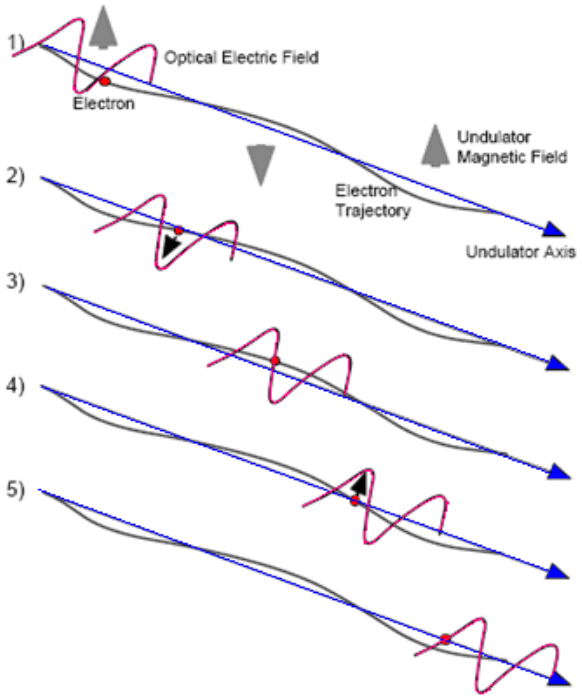

Figure 3.5: Five frames of single particle motion in an FEL under the influence of the optical and undulator fields.

The effect of slippage can significantly affect the FEL interaction. Also to be taken into account is the real beam temperature which causes a distribution in electron energy and position. The importance of this can be seen by looking again at fig. 3.5 and considering more than one particle: not all the particles will exchange the same amount of energy with the optical beam, but some will gain energy while some will lose energy. Therefore, as the electrons gain/lose energy, the trajectory of each electron is affected. Thus, the electron trajectory is determined by both the undulator and the radiation fields. The coupling of the electron motion and the radiation field (through the undulator field) implies that energy can be exchanged between the beam and the radiation, indeed, conservation of energy requires that if the beam loses energy, the radiation field will gain the equivalent amount of energy and vice versa. Therefore gain in the radiation field can be defined as the change in the electron kinetic energy divided by the radiation energy.

The next step is to introduce the concept of the “resonant energy”. At the resonant energy, the electrons don’t exchange any energy with the radiation field. Therefore electrons with energy greater than the resonance energy will lose energy to the radiation field and, similarly, electrons with energy less than the resonance energy will gain energy from the radiation field. The effect that is responsible for the energy loss and gain is the ponderomotive potential.

The ponderomotive potential (fig. 3.6) will tend to bunch the beam. High gain (gain much larger than 1) is then produced through an instability (bunching) and the phase bunching leads to coherent emission. Low gain, when the bunching is not required, can still be achieved by injecting a beam at an energy above the resonance.

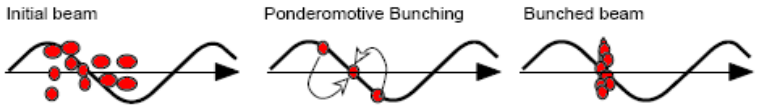

Fig. 3.6: Phase bunching of a particle distribution in a ponderomotive potential.

Radiation from a distribution of charged particles can display collective effects which enhance the total number of photon radiated, as well as affecting the frequency and angular spectrum. The coherent effect is due to the emitted radiation of separated electrons being in phase with each other. Distributions which lead to coherence are often referred to as being bunched. The extend of coherent enhancement of a radiation process can be crudely estimated by a number of electrons located within a longitudinal half-wavelength and a transverse half-wavelength divided by the Lorentz factor. Therefore the definition of bunching can be expressed as the clustering of the electron longitudinal distribution in groups separated by a resonant wavelength.

3.4 Coherent spontaneous emission

In order to give rise to stimulated emission, it is necessary for the electron beam to respond in a collective manner to the radiation field and to form coherent bunches. This can occur when a light wave traverses an undulatory magnetic field such a wiggler because the spatial variation of the wiggler and the electromagnetic wave combine to produce a beat wave, which is essentially an interference pattern. It is the interaction between the electrons and this beat wave which gives rise to the stimulated emission in free-electron lasers. In the case of a magnetostatic wiggler, this beat wave has the same frequency as the light wave, but its wave number is the sum of the wave numbers of the electromagnetic and wiggler fields. As a result, the phase velocity of the beat beam is less than that of the electromagnetic wave and, hence, it is called the ponderomotive wave. Since the ponderomotive wave propagates at less than the speed of the light in vacuum it can be in synchronism with electrons which are limited by that velocity.

The interaction between the electron beam and the ponderomotive wave is governed by a nonlinear pendulum equation (which can be found considering the Lorentz force equation of an electron subject to an idealised wiggler field):

$$\frac{d\gamma}{dz} = -\frac{\omega_r}{2c}\frac{a_r a_u}{\gamma}\sin\vartheta \qquad [3.39]$$

where ϑ is the ponderomotive phase, defined as:

$$\vartheta = \left(k_r + k_u\right)z - \omega_r t + \varphi_r + \varphi_u \qquad [3.40]$$

and where a_r and a_u are the dimensionless parameters for the radiation and undulator field respectively.

The problem with many electron bunches is that, at the wiggler entrance, they have a random longitudinal distribution, besides finite energy spread and emittance. For simplicity, consider an electron bunch entering the wiggler that has a duration longer than the slippage length $N_w\lambda_s$ so that the slippage between the radiation and the electrons can be neglected. This means that the electron phases with respect to the radiation phases are randomly distributed over each radiation

wavelength. So, if the electron beam is nearly monoenergetic and resonant, then half of the electrons will decelerate and half will accelerate (because of the sine-like magnetic field imposed by the wiggler), resulting in no net gain. If the wiggler is short and the electron peak current is low, amplification can be obtained by the injection of the particles with average energy slightly above resonance, $\langle\gamma\rangle_0 > \gamma_r$, such that gain slightly prevails over absorption. This is the so-called Madey's small signal regime [124].

But, if the wiggler is long enough and the electron peak current is sufficiently high, energy modulations leads to spatial modulations and the electrons will self-bunch on the scale of a radiation wavelength. This bunching turns out to occur around a phase corresponding to gain. Since most of the electrons have nearly the same phase, they emit coherent collective synchrotron radiation.

There are, however, collective instabilities of the system that lead to electron self-bunching and to exponential growth of radiation until non-linear saturation effects set a limit on the conversion of electron kinetic energy into radiation energy and therefore on the efficiency on the FEL process. In the saturated high-gain regime, the radiated power from *N* electrons scales as $N^{4/3}$ instead of *N* as in the case of nearly uncoupled particles. With a variable parameter or tapered wiggler, this scaling goes as $N^{5/3}$ [26]. However, when propagation effects and slippage are relevant, under proper conditions, a novel superradiant regime may occur, in which the radiation scales as N^2 [26].

3.5 FEL simulations

This section will summarise FEL simulations, based on experimental parameters, carried out using two different codes: GENESIS and SIMPLEX. The first part will show simulations with the well-known GENESIS code [125] and limitations of this code will be discussed, in particular the problems in running it for the time-dependent solutions. In the second part, simulations with the SIMPLEX code [126] are presented and compared with those from GENESIS. Despite the limitations, it is

hoped that simulations can convey useful information with regards to the experiments.

3.5.1 The GENESIS code

Developed at DESY in Germany and further extended at UCLA and DESY, GENESIS is a simulation code used to calculate the performance of FELs. A 4^{th}-order Runge-Kutta solver integrates the equation of motion for the electron energy and phase while a symplectic solver tracks the transverse variables through the magnetic lattice of the undulator. There are other two features incorporated with the propagation of the electron beam. The effect of energy loss due to spontaneous radiation and the growth of the energy spread due to the quantum fluctuation of the spontaneous radiation follow an analytical model [127] and is applied to the particle distribution without introducing unphysical bunching effects in the longitudinal phase space. The second feature is the effect of wakefields on the electron beam which is mainly modelled by a mean energy loss per integration step [128].

GENESIS 1.3 supports two modes of calculations: steady-state and time-dependent simulations. Steady-state simulations are based on the assumption of an infinitely long electron bunch and a radiation field with no longitudinal variation of any parameter. The longitudinal description can be reduced to a single wavelength (bucket) with periodic boundary conditions in the ponderomotive phase of the macro-particles.

Time-dependent simulations consider the beam to have a finite long beam (bunch length); GENESIS 1.3 discretises the radiation field and electron beam in time, referring to them as slices. Because information on the local electron distribution is carried by the radiation field only in the forward direction (slippage), time-dependent simulations rolls over the electron bunch starting from the back. Advancing the radiation field is split into two parts: solving the steady-state field equation and copying the field to the next slice. By using this method, only a single slice of an electron beam and the radiation field over the total slippage length,

which can be significantly shorter than the bunch length, needs to be kept in memory. Although the spacing of the slices can freely be chosen with GENESIS 1.3, some conditions have to be fulfilled for a valid time-dependent simulation.
The considerations about the code limitations are discussed in section 3.5.4.

3.5.2 The SIMPLEX code

SIMPLEX is application software developed to support the design of accelerator components in FEL facilities and help the FEL user community estimate the optical properties of FEL radiation. It has been written to investigate phenomena such as radiation power growth, electron motion in phase space, evolution of angular and spatial profile of the radiation field, etc. and has been developed at Spring-8 in Japan.
SIMPLEX has the following functions for FEL simulations: steady-state simulation with seeding, time-dependent simulation with shot noise implementation for the SASE regime, wakefield implementation, error sources related to phase slippage between undulator segments, field discrepancy and trajectory straightness. It is equipped with a full graphical user interface for pre- and post-processing and does not need any commercial software or libraries [129]. In fact, SIMPLEX is written in the C++ language with the standard template library (STL). This solves the equations describing the FEL process in the 3-dimensional (3-D) form.
The simulations can be divided into two types (steady-state and time-dependent) according to how to deal with the slippage between electrons and radiation emitted by them. With SIMPLEX, it is possible to have both a rigorous simulation and a rough one. The latter is useful not only to check if the parameters introduced for the simulation are valid but also to understand the meanings of parameters. As in the GENESIS code, SIMPLEX as well introduces the concept of “slice” for the time-dependent simulations and a slice has a longitudinal length of the order of the undulator period, and the FEL equations are solved for the radiation field (complex amplitude) and macro-particles within that slice [129].

3.5.3 Simulation results

To evaluate the conditions under which a FEL driven by a wakefield accelerator can work, the ALPHA-X undulator parameters have been used together with the typical electron beam parameters measured on the ALPHA-X beam line (see Chapter 6). Of course, both the beam parameters and the undulator specifications used in the simulations are the same for the GENESIS and the SIMPLEX codes. The parameter list used is summarised in table 3.1.

Electron Energy	100 MeV
Bunch length	0.3 μm
Peak current	1500 A
Bunch charge	5 pC
x emittance	1 π mm mrad
y emittance	1 π mm mrad
Energy spread	0.01
x beta function (average)	1.5 m
y beta function (average)	1.5 m
Seeding	Shot noise with λ = 203 nm
FEL ρ parameter	0.01114

Table 3.1: Initial parameters used during the FEL simulations.

The other important parameters needed for the codes, are the Twiss parameters α, β, γ and ε at the undulator entrance. These parameters describe the phase space ellipse orientation along the beam line (fig. 3.7) [130].

There are two ways to calculate the Twiss parameters. The first is to calculate the area and angular spread of the particles at the accelerator output and then use Liouville's theorem [131] to determinate the location and distribution of particles at the beginning of the undulator. The initial Twiss parameters can be used to deduce the new Twiss parameters after drift spaces or magnets using an appropriate

transformation matrix. The second method is to determine the phase-space ellipse at the undulator entrance using a particle tracer code (such as GPT or TRANSPORT, see Chapter 4).

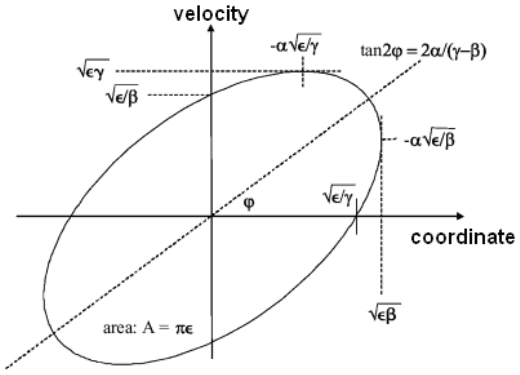

Figure 3.7: Phase space ellipse highlighting the Twiss parameters.

From fig. 3.7, fig. 3.8a and fig. 3.8b, we can determine α_x and α_y:

$$\begin{aligned} -\alpha_x\sqrt{\varepsilon_x/\beta_x} &= -0.03 \quad \& \quad \sqrt{\varepsilon_x/\beta_x} = -0.002 \quad \Rightarrow \quad \alpha_x = -15 \\ -\alpha_y\sqrt{\varepsilon_y/\beta_y} &= -0.028 \quad \& \quad \sqrt{\varepsilon_y/\beta_y} = -0.002 \quad \Rightarrow \quad \alpha_y = -14 \end{aligned} \qquad [3.41]$$

We now in fact have a set of two parameters with two unknowns for each axis which can be easily solved.

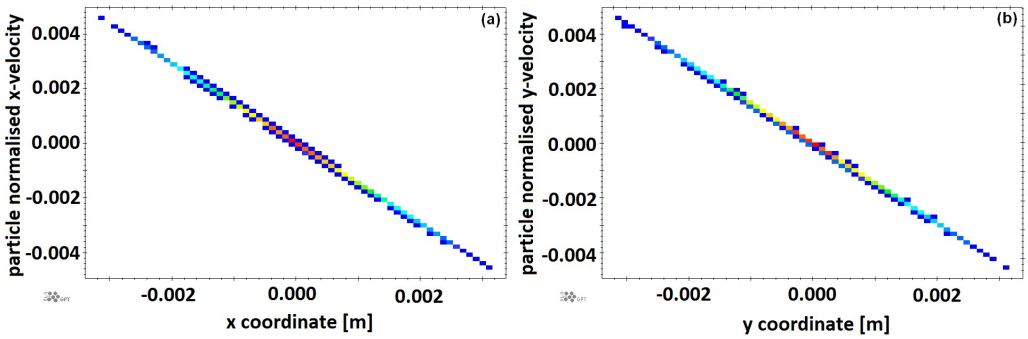

Figure 3.8: Phase space ellipse for the updated ALPHA-X beam line at the undulator entrance on the (a) x axis and (b) y axis.

The first simulations have been performed in the steady-state regime using the GENESIS code. Figure 3.9 shows the radiation power and the bunching factor as function of the distance inside the undulator. Note that simulation has been run for a longer undulator length (the ALPHA-X undulator is extendable to 3 m) in order to reach saturation.

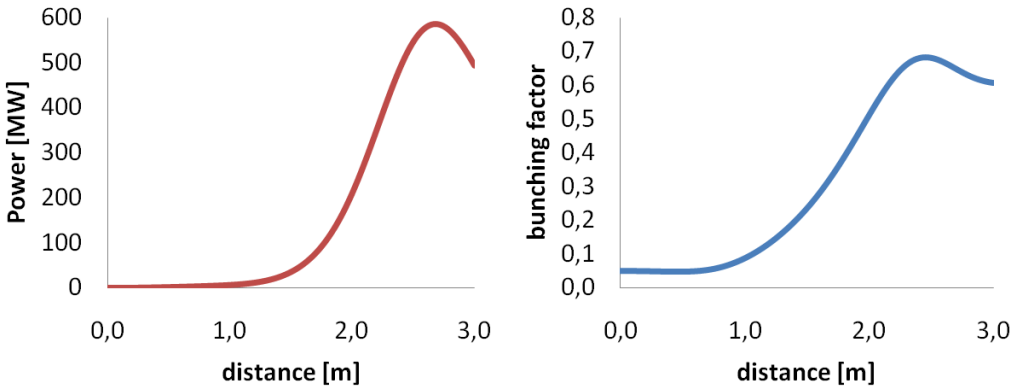

Figure 3.9: FEL simulations in the steady-state regime with GENESIS 1.3.

As shown in fig. 3.9b, the initial bunching factor for those simulations has been taken to be non-zero (initial value is 0.05). This assumption comes from the fact that the beam at the entrance of the undulator has a very short length and therefore the initial bunching has a small initial value. The simulation predicts a saturation power of 600 MW at a distance of 2.8 m, which means that saturation may not be observed using only a 1.5 m undulator (as realised experimentally, see later chapters). However, at a distance of 1.5 m, some gain is apparent and the predicted output radiation power is of the order of 50 MW. As far as the bunching factor, this gives similar information: the electron beam will be well bunched at a distance of 2.8 m and, at the end of the ALPHA-X undulator (1.5 m), it will be of the order of 20%.

The same set of simulations have been conducted using SIMPLEX and the results of the radiation power as function of the electron energy are shown in fig. 3.10. At 100 MeV, which is the energy used for the GENESIS simulations as well, the saturation will occur at 2.8 m, as predicted by GENESIS. The big difference between

the two codes is the predicted output power. SIMPLEX predicts an output power at saturation of 5 GW, while for GENESIS the power at saturation is only 500 MW which is 10 times lower. This difference can be due to the fact that with SIMPLEX the entire lattice section (composed by the triplet of permanent magnet and the triplet of electromagnet) have been simulated. This gives a much better description of the twiss parameters at the undulator entrance and inside the undulator, giving therefore a better description of the electron beam evolution, which can lead to a better and more accurate FEL simulation.

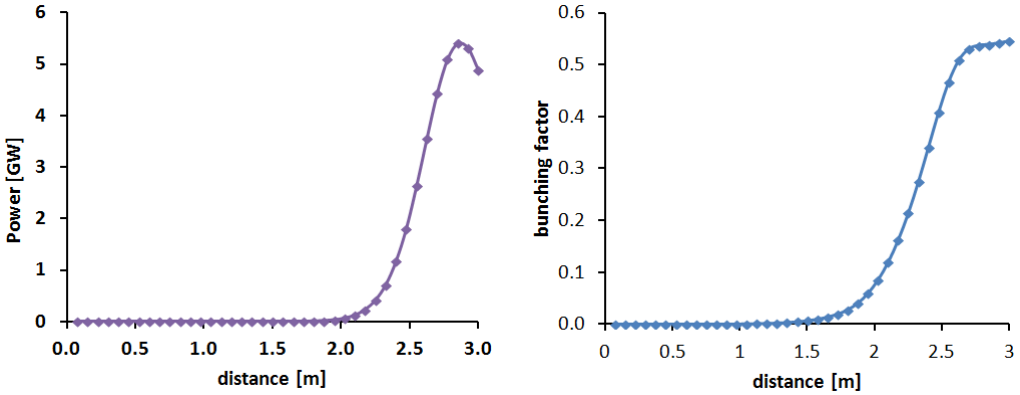

Fig. 3.10: FEL simulations in the steady-state regime with SIMPLEX.

The results for the time-dependent simulations are shown in fig. 3.11, where the radiation powers of the first, second and third harmonics have been plotted. The saturation power for the first harmonic is about 20 GW, at a saturation distance of about 1.8 m with a bunching factor that is ≈ 0.7 (fig. 3.11b), as expected for an FEL.

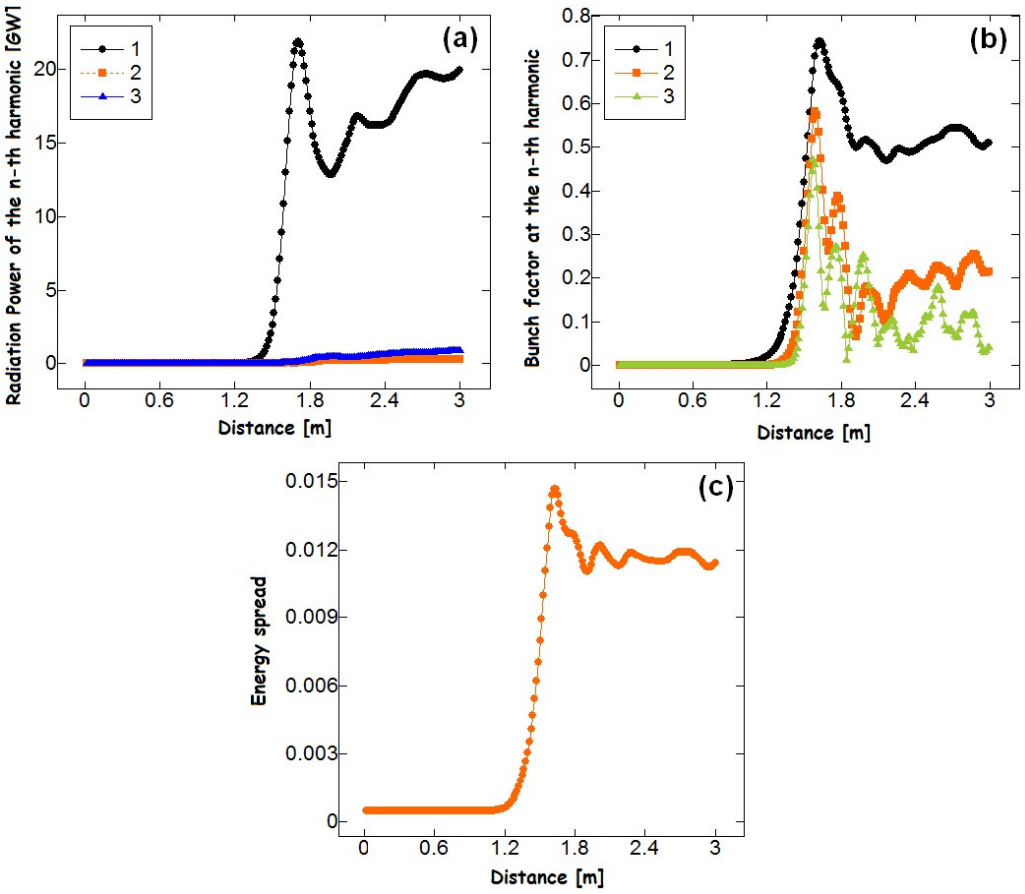

Figure 3.11: SIMPLEX time-dependent simulation results for the (a) radiation power, (b) bunching factor for the first three harmonics and (c) electron beam energy spread.

Figure 3.11c shows that the energy spread, which is initially 0.1%, reaches a value of about 1.5% at saturation, which is of the order of the FEL ρ parameter, as expected. The difference between steady-state and time-dependent regimes in terms of saturation length and output radiation power is very high. The reason can be the very short duration of the bunch, which, being so short, enhances the FEL operation.

3.5.4 Code limitations

Large problems were found when the time-dependent mode simulations for the GENESIS 1.3 code were attempted. The main difference between the time-

independent and the time-dependent simulations is that, in the first case, the beam is considered to have an infinite extension in time (filling the whole undulator). In the time-dependent simulation, the beam has a finite extension (a real bunch length) and the code divides the beam into slices and propagates the slices through the undulator. The propagation of the radiation field has to be done frequently to avoid collective instabilities of the steady-state field solver per integration step within a single slice. The first code limitation is on the integration step size, which is required to be much smaller than the gain length:

$$\Delta z \ll \frac{1}{2k_u \rho} \qquad [3.42]$$

where k_u is the undulator wave number. Also, the separation Δt between the slices (which is related to the integration step size by the inequality $c\Delta t \geq (k_u/k)\Delta z$, where k is the radiation wave number), is required to be:

$$\Delta t \ll \frac{1}{2ck\rho}. \qquad [3.43]$$

Another important limit regarding the code is on the time window of the simulation. Because GENESIS does not know anything about the field, which slips through the back of the time window, it suppresses the output over the first slippage length. To obtain therefore a valid output, the time window must be at least as long as the slippage length ΔT_s, yielding the constraint:

$$\Delta T \geq \Delta T_s = \frac{k_u}{k}\frac{L_u}{c} \qquad [3.44]$$

In practice, the time window should be significantly larger that the limit given above to allow a frequency analysis of the radiation. The typical width of the FEL spectrum is ρ. To resolve the spectrum, the time window must fulfil the more stringent constraint:

$$\Delta T \gg \frac{\lambda}{c\rho} + \Delta T_s \qquad [3.45]$$

The main problem comes from the fact that the code requires each slice to have a thickness that is at least one radiation wavelength λ. Therefore, the time-

discretisation has to be $c\Delta t \geq \lambda$ to avoid overlapping of the slices. Applying the experimental parameters to these limitation formulas and considering a 100 MeV electron bunch (which yields a radiation wavelength of around 200 nm), in order to fully slice the ultra-short electron bunch (1-3 fs duration), there will be only 4 slices which is not enough to be able to have a valid time window and to resolve the spectrum (20 slices being the minimum required number for the time window).

3.5 Discussion

FEL theory has been summarised in this chapter with particular attention on the spontaneous undulator radiation which is the radiation that comes from an undulator when the bunch current is not uniform (SASE); for this kind of radiation, the spectrum is very broad and the amount of power emitted is very low or even null if the electrons are uniformly spaced along the beam (because the radiation field and the undulator field cancel each other).

The high-gain theory has been discussed and the mechanism to have exponential radiation production has been explained. Contrary to spontaneous emission, in this case, the electrons in a bunch affect each other through the radiation field establishing this non-linear effect. In this case the radiation is emitted in a very narrow cone and the amount of power emitted is very large. In particular, the case of SASE FEL, which occurs when the initial power is null, has been introduced and the so-called gain length, which is the length that occurs to have spontaneous emission, has been defined. In particular it has been shown that for SASE radiation the undulator can be seen as divided in two parts: the first one has a length equal to the gain length and is used to produce spontaneous emission and the second one is the rest of the undulator representing the part where the radiation emitted before will be amplified.

The two-wave model has been introduced, which describes the interaction of a single electron with the optical and the undulator fields and the slippage effect has been explained, which is the effect of an electron travelling in an undulator field at

a different velocity compared with the radiation field. Eventually, the coherent radiation emission has been presented, which is a stimulated emission process arising from an electron beam responding in a collective manner to the radiation field forming coherent bunches.

Finally, simulations that have been conducted using the experimental parameters have been presented. In particular, two different codes, SIMPLEX and GENESIS, have been introduced. These two codes have been used in two regimes, the steady state and the time-dependent. As far as the steady state is concerned, both codes predict the same saturation length, while the saturation power is 10 times lower in the case of GENESIS with respect to SIMPLEX. This can be due to the fact that the lattice section has been simulated in more details with SIMPLEX. Time-dependent simulations have been conducted with the SIMPLEX code: the results show a saturation power of about 20 GW at a saturation distance of 1.8 m. It was not possible to use GENESIS for time-dependent simulations because of the restrictive limitations given by the input parameters and, in particular, on the electron bunch duration; the length of the beam was too short for the code slicing technique to generate valid time and frequency results.

The results shown with the FEL simulating codes are very promising and give confidence that FEL radiation can be seen with the ALPHA-X beam line if the electron bunch parameters match that simulated.

Chapter 4

Beam transport design and simulations

4.1 Introduction

The primary beam transport section is that which is situated between the end of the plasma channel, which acts as the accelerator, and the beginning of the undulator. The aim is to effectively transport, using magnetic fields, the electron bunches generated inside the plasma channel up to and through the undulator. In particular, as discussed in Chapter 3, a beta function equal to the length of the undulator is desired (matched transport). In addition, a requirement for future application is the ability to focus a wide range of electron energies into the undulator, i.e., in the range 50 MeV to 1 GeV. This requires flexibility to accommodate hugely different beam divergences for a fixed normalised emittance (which scales linearly with beam energy).

The ALPHA-X beam line commenced operations before the start of the work presented in this thesis and the pre-existing set-up (featuring only a triplet of electromagnetic quadrupole magnets) serves as the initial beam transport system that has been investigated here. It was rapidly determined that it is insufficient for the undulator radiation studies and, using simulations, many different schemes have been investigated (with different combinations of magnetic structures) in order to upgrade the transport system. It was found that the most realistic scheme comprises a triplet of permanent quadrupole magnets followed by a triplet of electromagnetic quadrupole magnets.

In this chapter the initial scheme and those implemented experimentally examined will be presented and the differences between them will be illustrated.

4.2 Initial beam line transport simulations

The ALPHA-X beam line was initially set-up as shown in fig. 4.1. Full details of all beam line components are provided in section 5.3 but here the relevant section is simply the beam transport section from the plasma channel to the undulator. The

layout of the whole beam line, highlighting the components summarised in table 4.1, is shown in fig. 4.1.

Beam line element	Distance from the accelerator
Lanex L1	60 cm
Electromagnetic quadrupoles	1.12 m, 1.499 m, 1.878 m
Lanex L2	2.091 m
Electron Spectrometer ES1	2.386 m
Lanex L3	3.179 m
Undulator	3.411 m
Lanex L4	5.198 m
Electron Spectrometer ES2	5.304 m
Detection system	5.696 m

Table 4.1: ALPHA-X beam line components and distances from the accelerator.

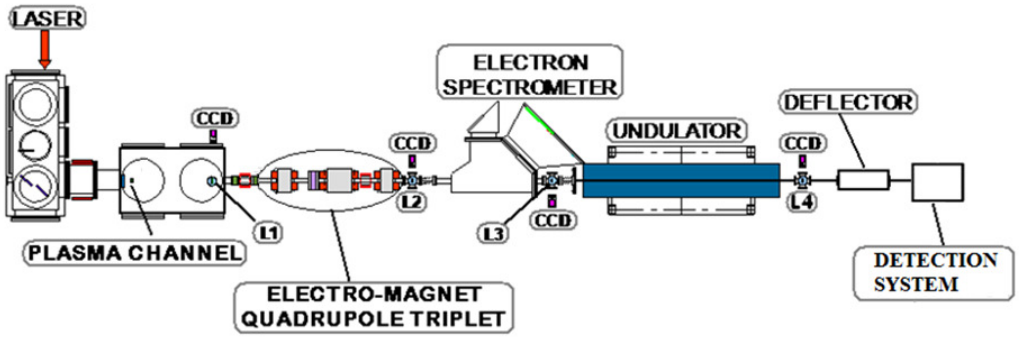

Figure 4.1: The initial ALPHA-X beam line.

In particular, as far as the quadrupoles are concerned, the length and the gradient are a function of the supply current is reported in table 4.2, where *N* is the number of coils of the quadrupoles (80 for the one in ALPHA-X), *I* is the current and *a* is the quadrupole's aperture (30 mm diameter for the ALPHA-X quadrupoles).

Quadrupole name	Total length	Gradient
DMQ1	122 mm	$\frac{4\pi N}{5\cdot 10^6}\frac{I}{a^2} \simeq 2\cdot 10^{-4}\frac{I}{a^2}[T/m]$
DMQ2	218 mm	$-\frac{4\pi N}{5\cdot 10^6}\frac{I}{a^2} \simeq -2\cdot 10^{-4}\frac{I}{a^2}[T/m]$
DMQ3	122 mm	$\frac{4\pi N}{5\cdot 10^6}\frac{I}{a^2} \simeq 2\cdot 10^{-4}\frac{I}{a^2}[T/m]$

Table 4.2: ALPHA-X quadrupole characteristics.

Using this set-up, it is possible to have matched transport for electron energies up to around 550 MeV and quasi-matched transport up to around 600 MeV, as shown in fig. 4.2, which shows the current needed to be applied to the quadrupoles to have a matched transport (a beta function inside the undulator of the order of 1.5 m). The maximum current that can be supplied to the quadrupoles is 20 A, therefore, matching is not sustained above 600 MeV.

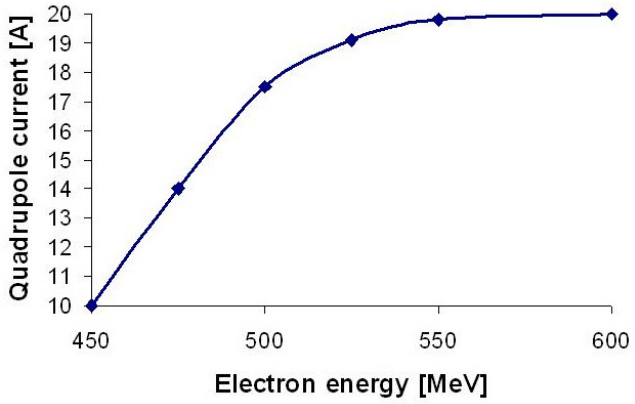

Figure 4.2: Current setting for matched transport using the initial set-up.

This transport system, therefore, is suitable for matching a fairly wide energy range, however, the bunch length of the electron beam increases drastically along the beam line, as shown in fig. 4.3.

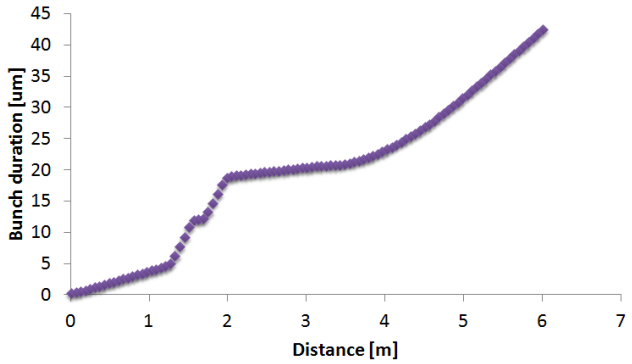

Figure 4.3: Bunch duration lengthening obtained using the initial set-up.

The bunch length simulation has been performed with an electron beam energy of 130 MeV, which is focused at the centre of the undulator, placed 4.1 m from the accelerator. The current quadruple settings for this simulations are 6.9 A for the external quadrupoles and 6.3 A for the central quadrupole. As shown in fig. 4.3, the bunch duration increases hugely from the initial value of 0.3 µm to a final value of 45 µm. This is primarily due to the large distance of the magnets from the accelerator which enables a significant amount of path length broadening to occur in the short electron bunch as it diverges from the plasma channel.

This discussion is useful to understand that this set-up is not suitable for matching the electron beam with the undulator and driving an FEL (which requires fs duration of the electron bunch to enhance the peak current). In fact, an elongation of the beam length means a lowering of the beam peak current. For this reason, it is of paramount importance to introduce a capturing system after the accelerator, in order to control and maintain the short duration of the electron bunches.

4.3 Design of a Permanent Magnet Quadrupole triplet

The idea of designing a new triplet of quadrupoles comes from the fact that if an external field is applied to the electron bunch as soon as it comes out of the accelerator, the beam quality can be maintained for a long distance. The initial

layout taken into account is shown in fig. 4.4. For test purposes, the initial layout simply consists of the accelerator, one triplet of permanent magnet quadrupole (PMQ) and a 1 m planar undulator with an entrance that is placed at a distance of 1 m from the accelerator.

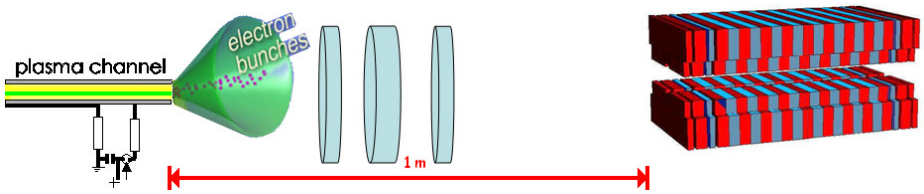

Figure 4.4: A possible design of the primary transport section.

The physical constraints of the existing beam line (accelerator located in a vacuum chamber as shown in fig. 4.1) prevent the installation of electromagnetic quadrupoles very close to the accelerator exit. Therefore, miniature PMQs [132] must be used. The added advantage of such magnets is they have very large field gradients (many 100s of T/m).

The test PMQs each have a magnetic field gradient *S* of of 500 T/m (which corresponds to a magnetic field strength of about 1.2 T) over a length L for the outer quadrupoles and L′ for the central quadrupole. In this case, the relation between the side and the central length is given by: $L' = 0.9 \cdot 2 \cdot L$.

For the simulations, the General Particle Tracer (GPT) code has been used. GPT is a software package developed to study 3D charged particle dynamics in electromagnetic fields [133]. Using this code, it is possible to define an electron bunch and propagate it through all kinds of devices, in this case, the three quadrupole magnets and the undulator.

Initially all the magnetic devices are taken as ideal: a simple model internal to the GPT code has been used. Knowing the optimum design [134-136] and the characteristics of the quadrupoles [137,138], a first simulation was set up. Before introducing the simulation, it is useful to introduce the dimensionless Lorentz relativistic factor γ. This quantity is related to the energy of the electron beam E (expressed in MeV) by:

$$\gamma = 1 + \frac{E}{0.511} \approx 2 \cdot E \,. \qquad [4.1]$$

The parameters chosen for the simulated magnets and undulator are summarised in table 4.3.

Lorentz factor	1000
Length of the outer quadrupoles	30 mm
Length of the central quadrupole	54 mm
Strength of each quadrupole	500 T/m
Corresponding magnetic field of each quadrupole	1.2 T
Position of the first magnet from the accelerator	0.1382 m
Position of the second magnet from the accelerator	0.2 m
Position of the third magnet from the accelerator	0.2719 m
Undulator length	1m
Number of periods	30
Undulator period	3 cm
Undulator field amplitude	1 T

Table 4.3: List of the parameters chosen for the first set of transport simulations.

The solution found for a 500 MeV electron beam is shown in fig. 4.5: the plot represents the evolution of the horizontal and vertical beam envelopes. The minimum of each curve represents the beam focal point which is placed at 1.5 m from the accelerator, corresponding to the centre of the undulator. Hence, this is a simple example of a matched transport system.

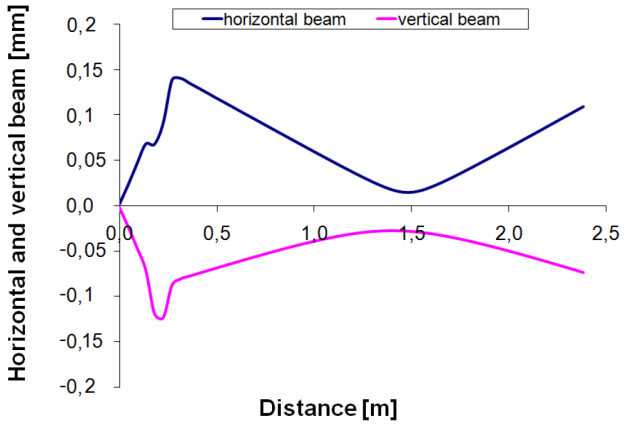

Fig. 4.5: Development of the horizontal and vertical beam envelopes of a 500 MeV plasma accelerated electron beam.

Another important beam parameter to consider in the simulations is the emittance (section 2.4.2). The emittance is the extent of momentum phase space occupied by the beam as it propagates [139]. It is related to the width of the particle beam, the dispersion function *D* and the momentum spread of the particle beam (dp/p) by:

$$\varepsilon = \frac{6\pi\left(width^2 - D\left(dp/p\right)^2\right)}{B}. \qquad [4.2]$$

Since it is difficult to measure the full width of the beam, the RMS width of the beam is measured. The emittance from this width measurement is then referred to as the "RMS emittance". For the simulation, the RMS normalised emittance was assumed to be ε = 1.0 π mm mrad.

The main goal behind this design is to efficiently transport beams with energies in the range of [50, 1000] MeV. Similar to the case of section 4.2, it is apparent that the above system will not work for such a wide range of energies: in fact, different energies will have a different behaviour when passing through the quadrupoles such that changing the electron energy will cause the transport to be not optimised anymore. As opposed to electromagnetic quadrupoles, PMQs have a permanent field strength that cannot be changed and so the way to optimise the transport for such a wide range of energies would be to separate the three quadrupoles with

respect to each other using translation stages to provide a matched transport for every energy.

In practice, the central quadrupole would be fixed and the outer quadrupoles translated over a range of millimetres as a function of the energy. This design is effective and covers all the energies using three different triplets of quadrupole magnets without overlap and ensuring 10 cm between the plasma channel and the first magnet to be sure that it is possible to move the lens without obstructions.

In particular, the three triplet of quadrupole magnets have the same gradient S = 500T/m, while the lengths are chosen as in table 4.4.

	Left Quad	Central Quad	Right Quad
Triplet 1	5 mm	9 mm	5 mm
Triplet 2	10 mm	18 mm	10 mm
Triplet 3	30 mm	54 mm	30 mm

Table 4.4: Lengths of the quadrupoles of the three triplets.

With these three triplets of quadrupoles, it is possible to cover all the electron energies ranging from 50 MeV up to 1 GeV. In particular, Triplet 1 is used to cover all the electron energies from 50 MeV to 80 MeV, Triplet 2 is used from 80 MeV up to 300 MeV and, lastly, Triplet 3 is used from 280 MeV up to 1 GeV. In order to achieve a matched transport (focus of the electron beam at the centre of the undulator with a beta function of 1 m), for each triplet, the side quadrupoles need to be moved with respect to the central one. The movement is a function of the energy; this dependence is shown in fig. 4.6.

In particular, Fig. 4.6a shows the movements of the side quadrupoles (blue line is the movement of the left quadrupole and pink line is the movement of the right quadrupole) with the central quadrupole placed 0.15 m far from the accelerator: the limit in electron energy is given from the fact that smaller distances means an overlap of the quadrupoles while larger distances means an overlap of the left quadrupole with the accelerator. Similar considerations are valid for the other two

triplets. In particular, fig. 4.6b and 4.6c show the movements of left and right quadrupole with respect to the central quadrupole for Triplet 2 when the central quadrupole is placed 0.15 m and 0.2 m from the accelerator respectively. For high energy, fig. 4.6d and 4.6e show the movement of the external quadrupoles of Triplet 3 when the central quadrupole is placed 0.2 m and 0.25 m from the accelerator.

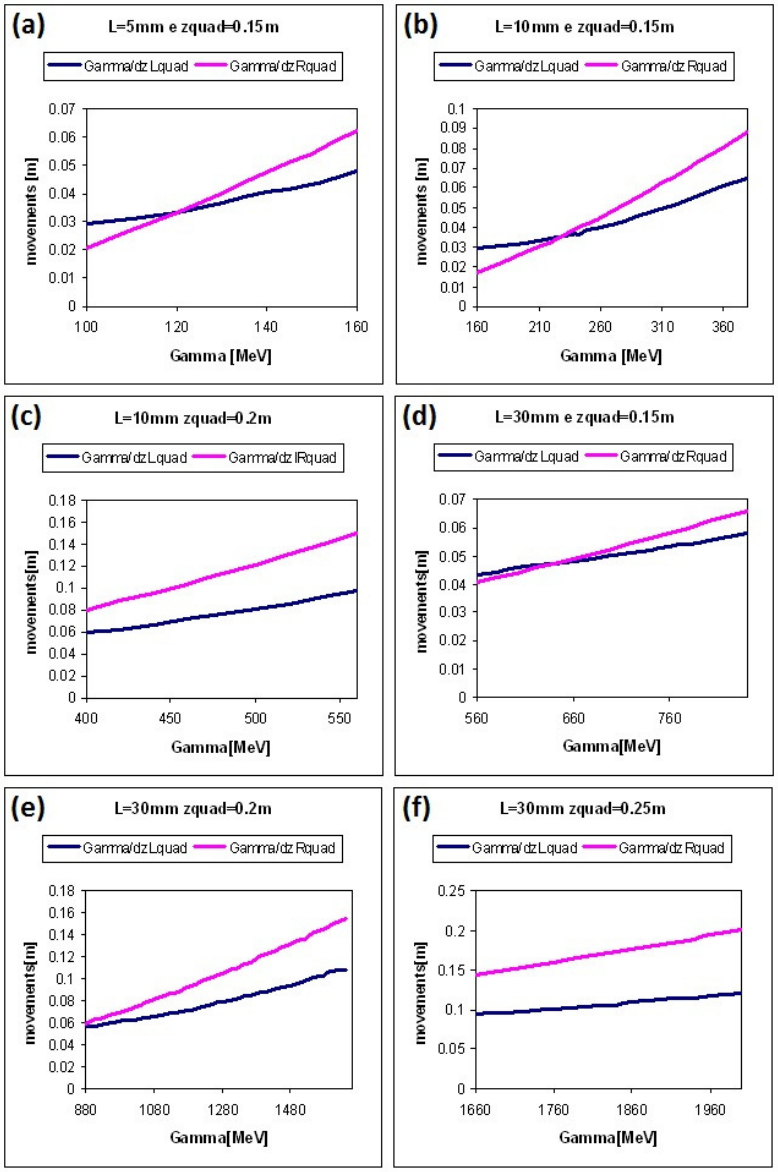

Figure 4.6: Positions of the quadrupole magnets versus energy. Lquad = length of quads, zquad = position of the centre of the triplet.

The next step in the design of the primary transport section is to use a more realistic model for the quadrupole magnets instead of the ideal GPT model. This has been achieved using CST Studio Suite, which is an electromagnetic simulation software suite that includes many tools for 3D electromagnetic design and optimisation [140]. The quadrupoles have been simulated by splitting a cylinder in 12 sectors and magnetising each sector with a magnetic field strength of 1.2 T. The magnetisation directions are shown in fig. 4.7a.

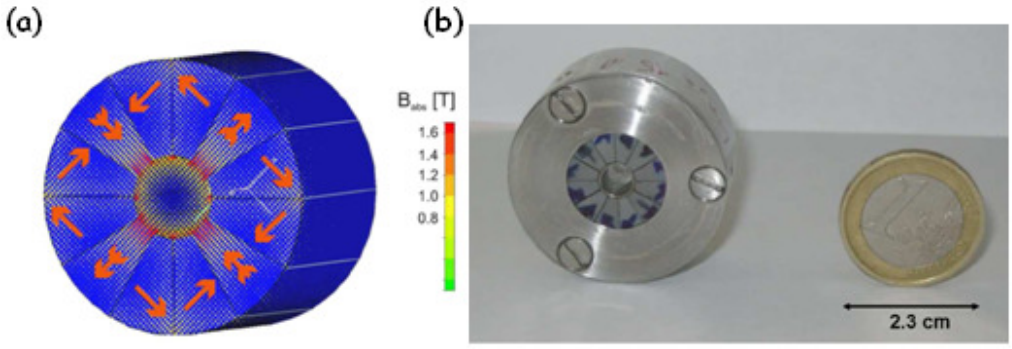

Figure 4.7: (a) Magnetisation of the permanent quadrupoles and (b) a photograph of a constructed PMQ.

The simulated quadrupoles are very compact. They have an inner bore radius of only 3 mm and an external radius of 10 mm, dimensions that are comparable to a 1 euro coin (fig. 4.7b) [135].

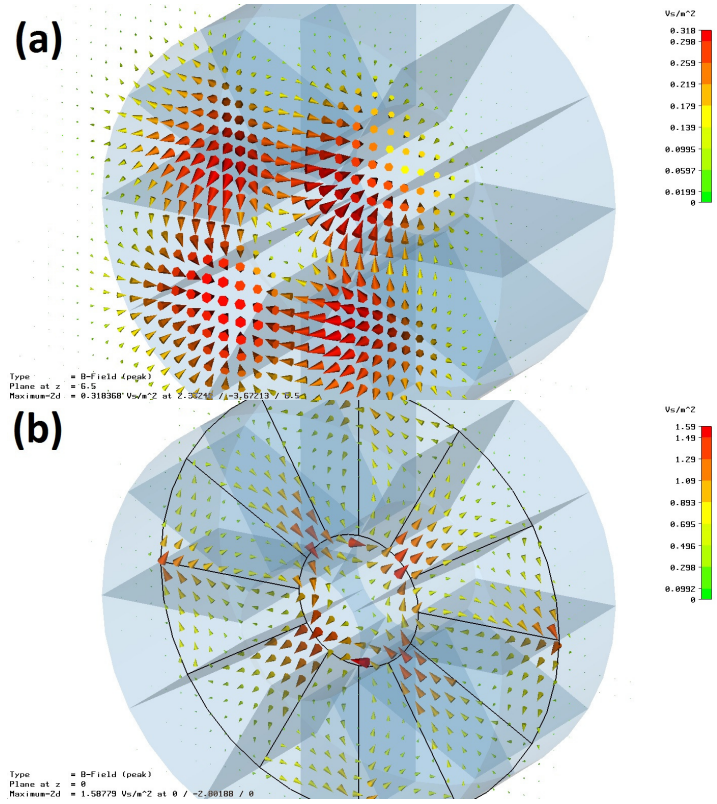

Figure 4.8: Magnetic field (a) outside and (b) inside the quadrupole lenses.

Figure 4.8 shows the magnetic field outside and inside the quadrupole magnet simulated using the CST Studio Suite software. The magnetic field map given as output of the software has been then passed to the GPT code. In particular, simulations have been carried out using the GPT internal model for the quadrupoles and the map field passed to GPT from CST Studio suite and fig. 4.9 shows the comparison between the two models.

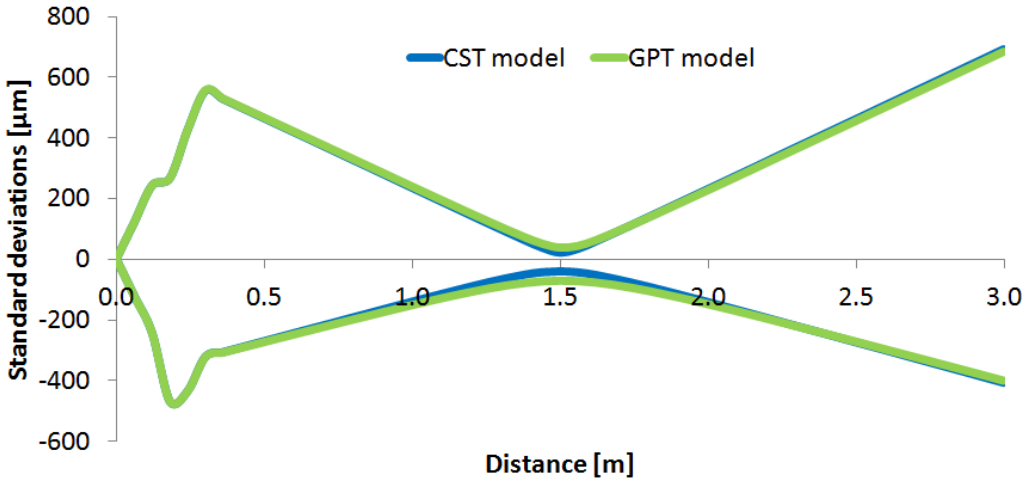

Figure 4.9: Comparison between GPT simulations using the GPT internal model for the permanent quadrupoles and the field map extrapolated by the CST Studio Suite code.

The plot shows that the two models give more or less the same results. The difference is in the spot size at the focus which is due to the fact that the GPT internal model for the quadrupoles does not include the fringing field, while in the map field, this effect is included.

Using this set-up, it is possible to have a very small spot (37 x 70 µm) at the centre of the undulator which matches very well with the FEL conditions. However, to have the focus at the centre of the undulator, the first magnet of the triplet must be placed 15 cm from the accelerator and the bunch length will be still too long, as shown in fig. 4.10. In fact, at the undulator entrance, the bunch length is of the order of 6 fs, giving therefore a peak current which is of the order of few hundreds of amperes (only 250 A), which is too low to drive the FEL.

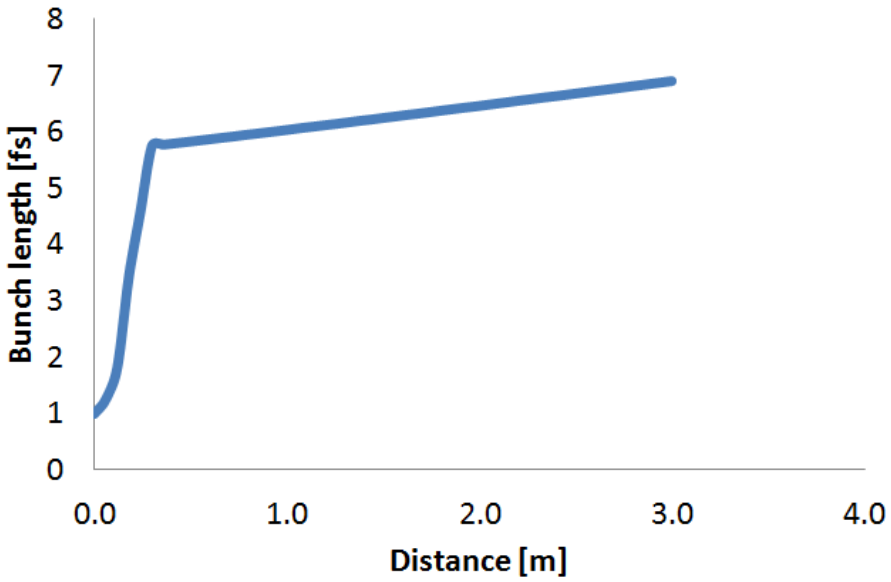

Figure 4.10: Bunch duration lengthening using only a triplet of permanent magnet.

For this reason, it becomes of paramount importance to find the right quadrupoles configuration in order to have a small and round spot at the centre of the undulator, while maintaining the short bunch duration. This configuration has been found to be the coupling of the permanent magnet triplet and the electromagnetic quadrupole triplet, as shown in the next section.

4.4 Upgraded beam line transport simulations

As stated in the last section, the electron bunches driven by laser wakefield acceleration suffer bunch lengthening due to path length differences and space-charge effects. The way to reduce this effect as much as possible is to place the permanent quadrupole triplet as close as possible to the accelerator exit without paying attention to the focal position and then use a triplet of "conventional" electromagnetic quadrupoles to place the focal position at the centre of the undulator. In this section, the final transport section is presented; this transport section has been designed to optimise the transport for the widest possible energy range, from 50 MeV up to 1 GeV. For this particular case, the role of the permanent

quadrupoles is to reduce significantly the divergence of the input beam and then use the electromagnetic quadrupole triplet to focus the beam at the centre of the undulator. In order to cover such a wide range of electron energies, two permanent magnet triplets have been used; details of the two triplets are reported in table 4.5.

	Left Quad	Central Quad	Right Quad
Triplet 1 - Low energy	10 mm	18 mm	10 mm
Triplet 2 - High energy	30 mm	54 mm	30 mm

Table 4.5: Lengths of the quadrupoles of the two triplets.

The first important difference between this design and the previous one described in section 4.3 is that, in this case, the permanent quadrupoles are adjustable just for the high energies (from 450 MeV) while, for the low energies, they are fixed in position with respect to each other.

So, for the low energies, the most important role is played by the dynamic quadrupoles, and the strength is simply changed by changing the current that flows into the coils; while for the high energies, the permanent magnets must focus the beam at the centre of the undulator directly because, as shown in section 4.2, the strength of the electromagnetic quads will not be sufficiently high to act on the electron bunch (their contribution will be very small). In fig. 4.11 are shown the results carried out using GPT for a low energy (E = 250 MeV) and a high energy (E = 750 MeV) beam. Both the beams are focused at 4 m, corresponding to the centre of the undulator.

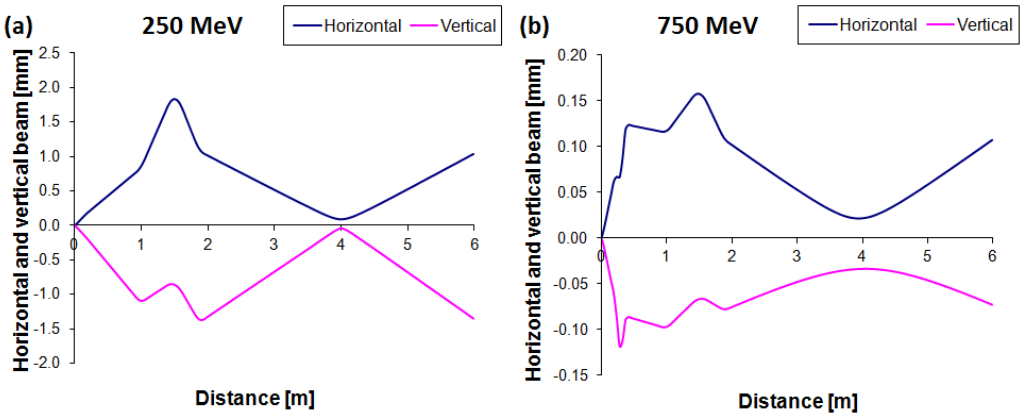

Fig. 4.11: Results for a (a) low energy bunch and (b) high energy bunch.

The corresponding bunch length is shown in fig. 4.12. The results demonstrate that the bunch length increases from 2.96 μm of the case with permanent magnets and electromagnets (fig. 4.12a) to 4.5 μm for the case with only the electromagnets (fig. 4.12b).

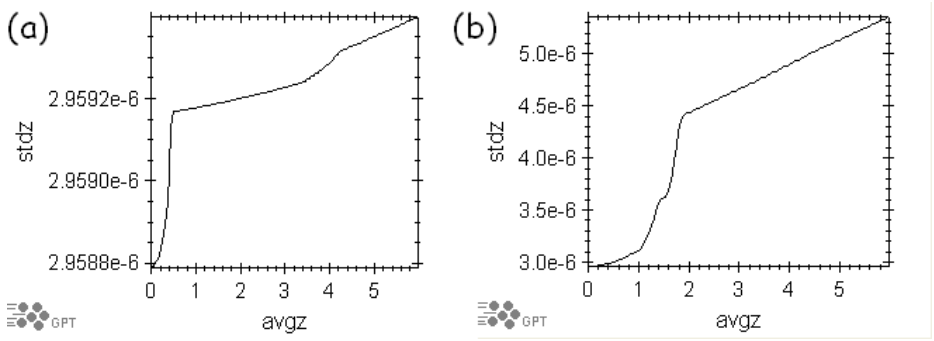

Fig. 4.12: Bunch length (stdz in meters) as a function of distance (avgz in meters) with (a) permanent magnets and electromagnets and (b) only electromagnets.

In Section 4.4.5 the final set-up to have even shorter bunch durations will be explored. However, the set-up presented in this section has been used for a wide number of experimental campaigns, including FEL experiments.

4.4.1 Undulator model

Another important step forward in the characterisation of the beam line, from a simulation point of view, has been to replace the ideal model of the undulator with a more realistic one. In fact, until now, a simple idealised model, internal to the GPT code, was used. But the ALPHA-X undulator, which acts as the amplifying medium with the electron bunches, has important characteristics such as focusing and guiding of the electron bunches, especially at low energies (up to around 90 MeV). Specifications of the ALPHA-X undulator are given in table 4.6.

Undulator length	1.5 m
Number of periods	100
Undulator period	1.5 cm
Peak on-axis magnetic field	0.27 T

Table 4.6: Real parameters of the ALPHA-X undulator.

The undulator simply consists of an array of permanent magnets with alternating polarity (fig. 4.13); the magnetic field provides a periodic transverse acceleration to the injected electrons which, in turn, produces electromagnetic radiation. Slotted pole pieces provide a constant quadrupole field to guide the electron beam.

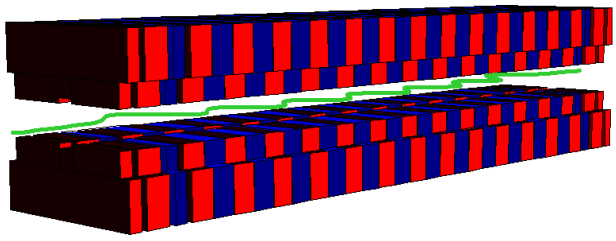

Fig. 4.13: Schematic of a planar magnetic undulator.

As in the case of the permanent quadrupoles, a magnetic field map corresponding to the real undulator was provided as input to the GPT code. The field map has been provided by the ASTeC team at Daresbury Laboratory (STFC) from the files

used to design the undulator [141]. Also in this case, many simulations have been performed, demonstrating that the design works very well and that changes to it are not required. The results carried out using the GPT code are shown in fig. 4.14.

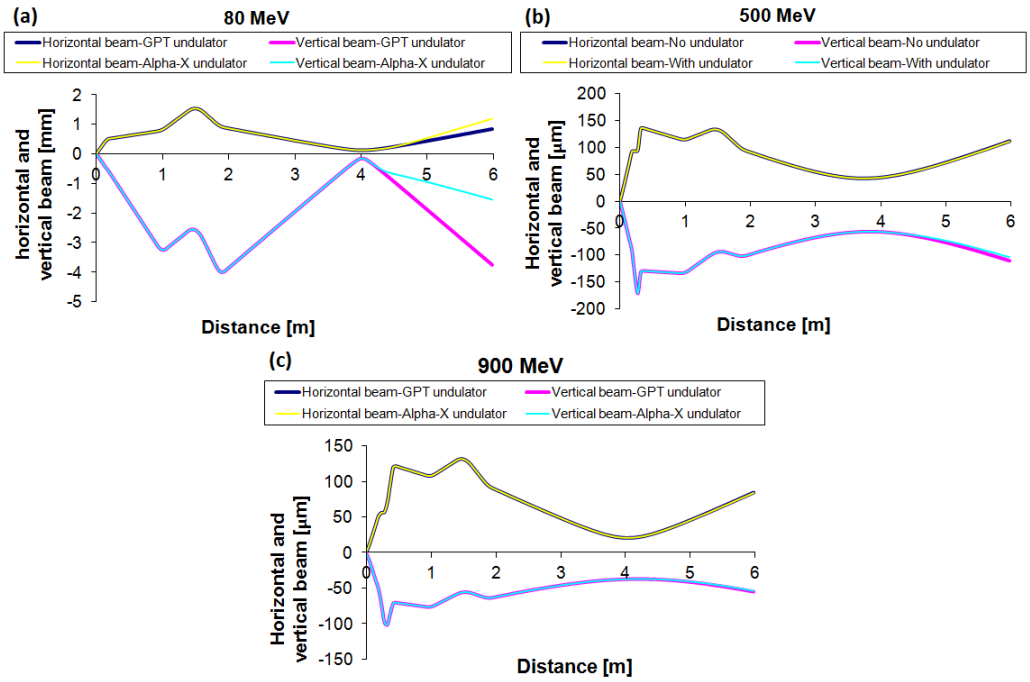

Figure 4.14: Horizontal and vertical beams envelopes at (a) low, (b) medium and (c) high energies.

It is clear that the undulator focuses the beam at low energies, while at medium and high energy, its action on the beam is negligible.

4.4.2 Off-axis propagation

Another test done with the ALPHA-X set-up was to study the electron transport of an off-axis electron bunch. In fact, until now, it have been always supposed that the beam exiting the plasma was travelling on-axis and the angle of propagation was always equal to zero, which is clearly an idealisation. In reality, the beam doesn't always travel on-axis and can be displaced by a few mrad or it can travel with a pointing angle with respect to the propagation axis. In this section the simulations performed assuming off-axis propagation of the electron beam are presented. In

particular, with the use of the GPT code, two particular cases have been simulated: i) a beam propagating displaced from the quadrupole axis by up to 250 μm and ii) an electron beam propagating at an angle up to 10° from the axis.

For the first case, describing displaced propagation, the geometry of the simulation is shown in fig. 4.15.

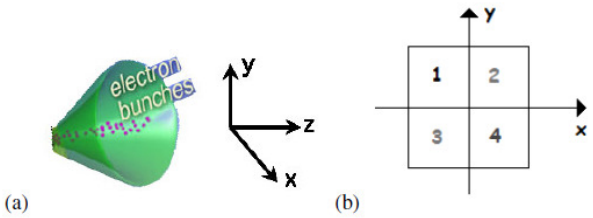

Figure 4.15: (a) The geometry used for the simulations and (b) the square in which the beam has been moved.

For the first set of simulations, the bunch has been displaced in one point of a square, as shown in fig. 4.16b. For simplicity in the simulation process, the square is divided in four quadrants. In each quadrant, a matrix of initial beam position has been simulated with a step, from one point to another, of 25 μm for a total of 625 simulations for each quadrant. Then all the 625 simulations have been plotted on the same graph to see how much the electron bunches were suffering from the displacement.

The simulations are shown for two different energies (150 MeV and 750 MeV respectively) with the electron beam displaced in different points of two different quadrants (the 3rd and the 1st respectively), as shown in fig. 4.16 and 4.17. The different lines represent the different trajectories along the beam-line for each particular initial beam position inside the quadrant.

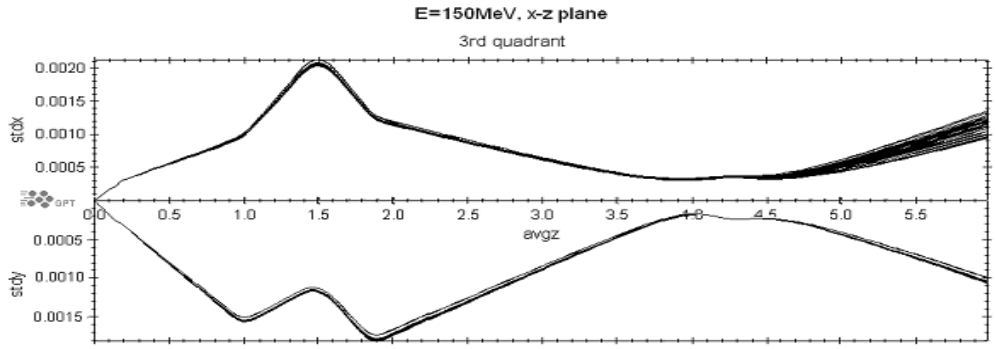

Figure 4.16: Trajectories of the electron bunches (stdx and stdy bunch size in the horizontal and vertical planes respectively) propagating off-axis inside the 3rd quadrant for an electron energy of 150 MeV.

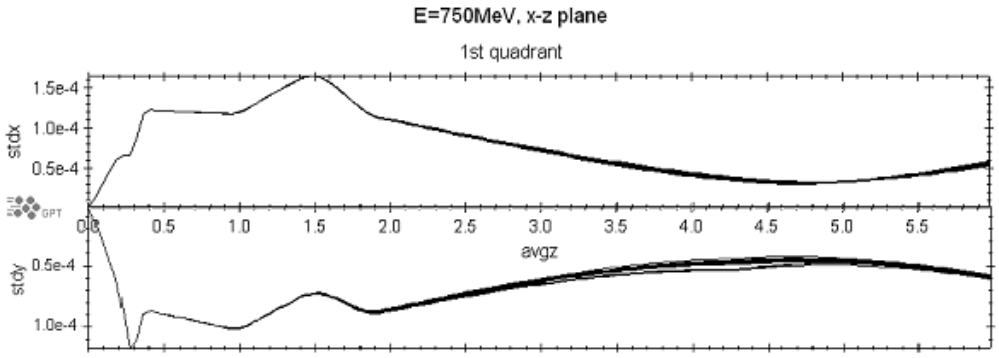

Figue 4.17: Trajectories of the electron bunches (stdx and stdy bunch size in the horizontal and vertical planes respectively) propagating off-axis inside the 1st quadrant for an electron energy of 750 MeV.

The second set of simulations has been carried out by changing the angle of propagation of the electron bunch (fig. 4.18 and fig. 4.19); the investigated angles are from 0° to 10°. Here as well, each line represents the trajectory of a beam propagating with a different angle.

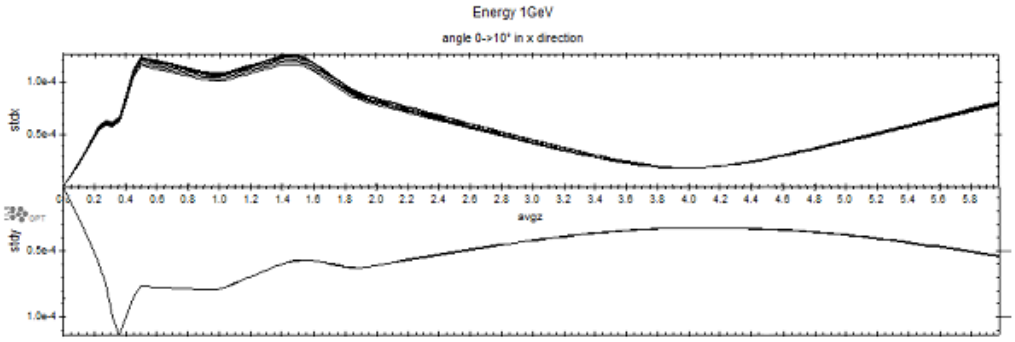

Figure 4.18: Trajectories of the electron bunches propagating with an angle in the x direction for an electron energy of 1 GeV.

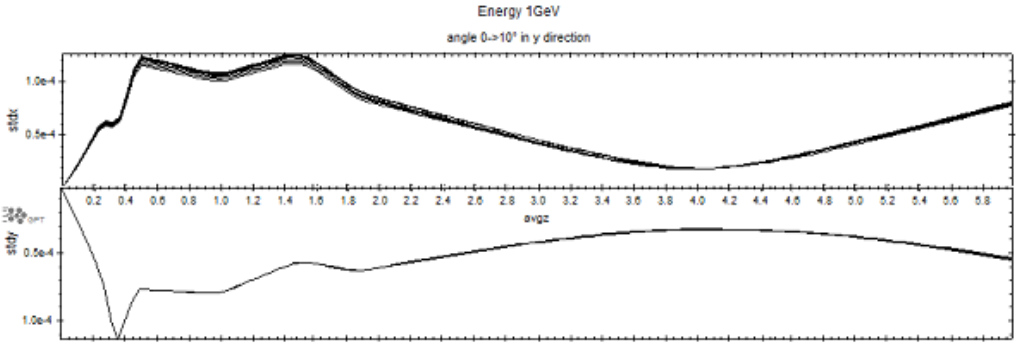

Fig. 4.19: Trajectories of the electron bunches propagating with an angle in the y direction for an electron energy of 1 GeV.

4.4.3 The electron spectrometer sections

In this section, a detailed description of the two electron spectrometers that are part of the ALPHA-X beam line are presented. The first one is a high resolution dipole imaging spectrometer that is located just before the undulator. The second one is a permanent magnet dipole spectrometer, which is a simple bending magnet with lower resolution, located after the undulator. In particular, for the first spectrometer, GPT simulations have been carried out to understand which information can be extrapolated from the spectral data while, for the second one, a more intensive study has been carried out to design the spectrometer itself for use as an electron spectrometer. For both spectrometers, a study of the resolution has

been conducted and will be presented here. Just for simplicity, in this section the "electron spectrometer" will be the one placed before the undulator and "deflector" will be that placed at the end of the beam line.

4.4.3.1 The electron spectrometer simulations

The ALPHA-X electron spectrometer has been designed by Allan Gillespie and Allan McLeod at Abertay University, Dundee. It uses a Browne–Buechner design [142] to provide strong focusing in the horizontal and vertical planes thus enabling excellent energy resolution to be maintained over a wide range of energies and has been built by SigmaPhi in France. The extra focus in the vertical plane is given by a quadrupole-like field so to focus the beam on the vertical axis, which is the direction where usually the information is lost. The final design of the spectrometer is shown in fig. 4.20.

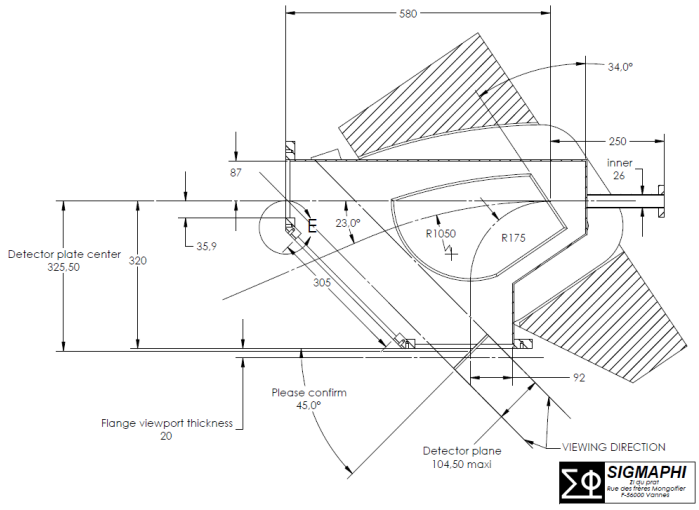

Figure 4.20: Design of the ALPHA-X high resolution electron spectrometer.

Because of the particular shape of the spectrometer and its properties, it has been necessary to simulate the actual magnet without using an internal model from the GPT code. The GPT model has been written by Bas Van der Geer and Marieke de Loos, who are the GPT's authors and active collaborators of the ALPHA-X project.

The magnetic field of this spectrometer can be modified by changing the current flowing in the coils; in this way the dynamic range of energies detectable from the spectrometer is quite large, from 0 MeV (no current supplied) up to 717MeV (at the extreme field of 1.8T and maximum supply current of 250 A).

The electron spectrometer is equipped with two Ce:YAG screens, one is the so-called “high energy window” and the other one is the so-called “low energy window”. The YAG screen of the high energy window is composed of 3 Ce:YAG crystals of 10 cm length each, while the low energy window is composed of 2 such Ce:YAG crystals. Crystal thickness is 1 mm and vertical height is 10 mm. A schematic drawing of the spectrometer field region and YAG position is shown in fig. 4.21. Electrons are deflected around 90° into the low energy window while more energetic electrons can be deflected at smaller angles into the high energy window.

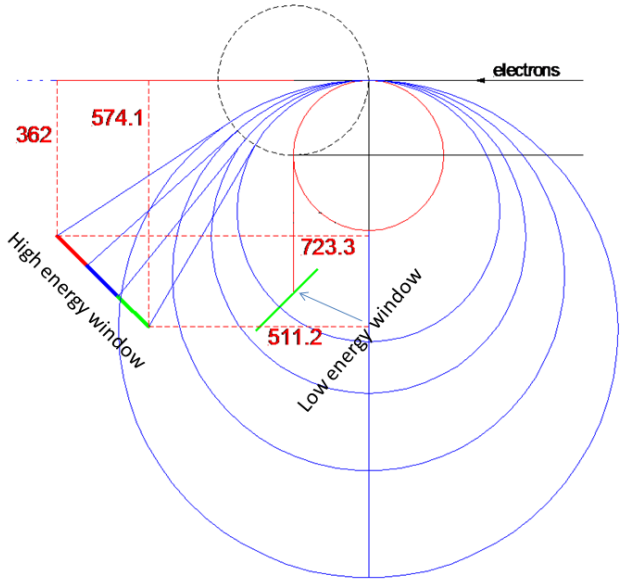

Figure 4.21: Design of the ALPHA-X high resolution electron spectrometer where the dashed circle represents the magnetic field region.

From a mathematical point of view, the magnet can be modelled as a circle. The electrons, coming from the right hand side, as soon as they enter in the magnetic field, will start to perform circular trajectories; the bending radius of a circular trajectory depends on the electron energy. Electrons with higher energy will follow

larger circular trajectories (radii of curvature) while electrons trajectories at lower energy will have a smaller radius of curvature. Once the electrons leave the magnetic field, their trajectories will be linear and, after some drift space, they will hit the scintillating screen. In particular, when the energy of the electrons is very low, their trajectory inside the magnet will follow a circumference with a radius that is close to the radius of the magnet: in that case, the electrons exiting the magnet will hit the low energy window scintillating screen.

The aim of this section is mainly to calculate the resolution of the spectrometer and to understand if, from the spectral measurement, some more important information can be obtained, apart from, of course, central electron energy and energy spread.

In particular, the case of an applied magnetic field of 0.59 T will be explored in this section, which is a typical magnetic field used during the experiments and attention will be focused on the high energy window scintillating screen.

In particular, fig. 4.22 shows the bending radius that the electrons have to follow in order to hit the edges of the three Ce:YAG crystals that compose the high energy window. The corresponding bending radii have been calculated using a simple mathematical model which, as described before, considers the magnet region as circular with a radius of 0.175 m.

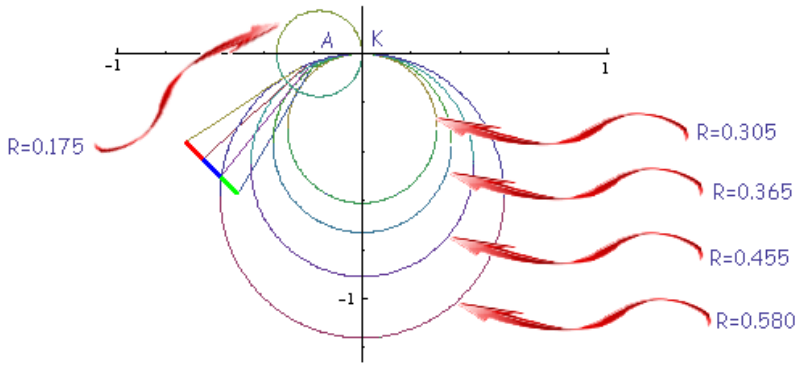

Figure 4.22: Trajectories and bending radii of the electrons subject to a constant magnetic field.

Using this information together with the *v x B* Lorentz force, the electron energy at the edges of the Ce:YAG crystals as function of the bending radius can be calculated as:

$$r[mm] = \frac{\gamma m_0 c}{eB} \cong \frac{3.34\, E_0[MeV]}{B[T]} \quad \Rightarrow \quad E_0[MeV] = \frac{r[mm]B[T]}{3.34}. \qquad [4.3]$$

Let's now change the coordinate system so that the new zero position of the coordinate system corresponds to the edge of one of the three Ce:YAG crystals composing the high energy window screen; in particular, the 0 cm position will correspond to the smallest radius and the 30 cm position will correspond to the largest bending radius, as shown in fig. 4.23 and summarised in table 4.6. In this way, it will be possible to calibrate the whole screen for energy and energy spread measurements.

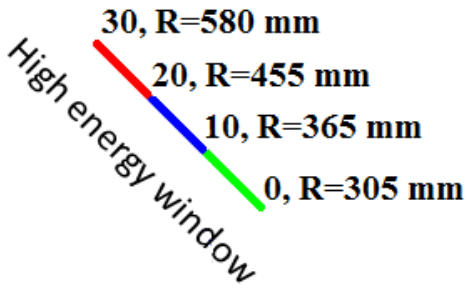

Figure 4.23: Calibration of the electron spectrometer high energy window.

Position	Energy
0 cm	54 MeV
10 cm	65 MeV
20 cm	80 MeV
30 cm	103 MeV

Table 4.7: Energy calibration of the electron spectrometer low energy window at B = 0.59 T.

This information is essential to calculate both the energy and the energy spread of the electron bunches. In fact by plotting the position as function of the energy (see fig. 4.24), a unique fitting curve can be obtained that defines the energy at each

point of the scintillating screen (which will correspond to the pixels of the CCD camera used to image the screen).

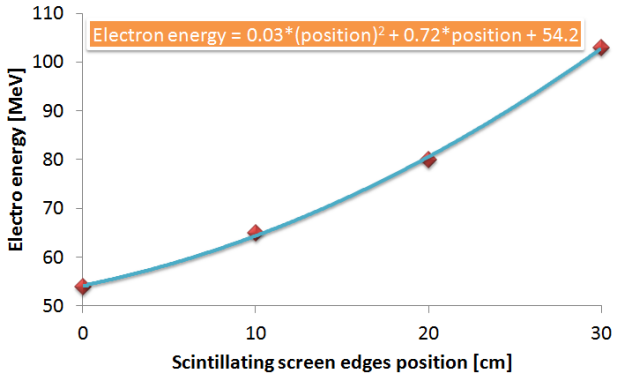

Figure 4.24: Electron energy along the high energy window as function of screen position for B = 0.59 T.

In order to calculate the resolution of the electron spectrometer, the GPT code has been used. An ideal beam has been sent through the spectrometer (no initial energy spread, emittance quasi-zero, no space-charge effects); the resolution of the electron spectrometer will then be given by the spread introduced by the system. The parameters of the bunch used for this simulation are summarised in table 4.8.

Electron energy	85 MeV
Energy spread	0 %
Initial emittance (x and y)	0.01 π mm mrad
Charge	10 pC
Beam size @ spectrometer entrance	5 mm
Initial bunch length	1 μm

Table 4.8: Parameters used for the simulation to calculate the resolution of the spectrometer.

The accelerator, for this particular simulation, is assumed to be at the electron spectrometer entrance. The GPT 2D output is shown in fig. 4.25.

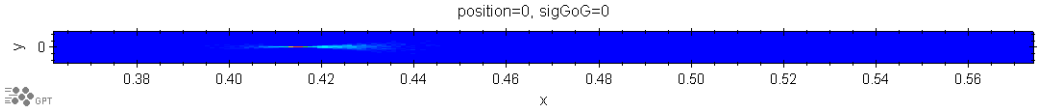

Figure 4.25: Energy spectrum of the electron bunch simulated with GPT.

The corresponding profile is shown in fig. 4.26, where the x position has been converted into energy using the calibration curve calculated from fig. 4.24. The profile is very well approximated by a Gaussian profile; the sigma of the Gaussian, divided by the peak energy, corresponds to the resolution of the electron spectrometer.

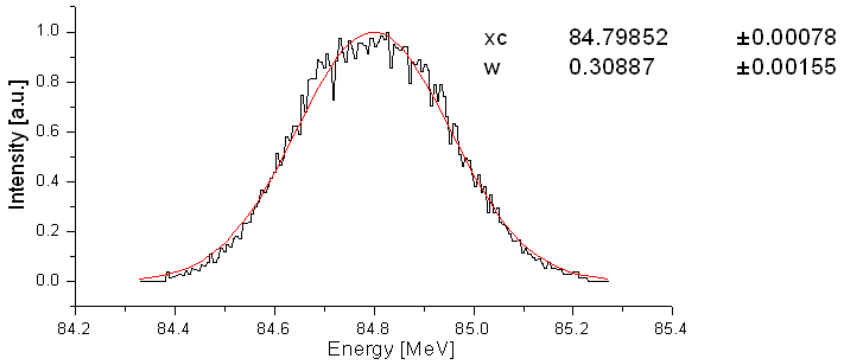

Figure 4.26: Histogram of the electron spectrum (black) approximated with a Gaussian profile (red).

The Gaussian has width w = 0.309 and central energy is xc = 84.799 MeV, which gives an energy spread of 0.182%: this, therefore, is the resolution of the electron spectrometer at a magnetic field strength of 0.59 T.

As further series of simulations has been performed changing the initial electron beam emittance and simulating the whole beam line, both in the case where the permanent magnet quadrupole triplet is in place and the case where there are only the electromagnets. The initial emittance has been changed from 0.1 to 3 π mm mrad in both cases and then investigating the corresponding electron beam profile expected to be observed on the scintillating screen. The results are shown in fig. 4.27 and show that the higher the emittance, the poorer the resolution of the electron spectrometer becomes. Moreover, when using the permanent magnet

quadrupoles, this effect is smaller, mainly because the presence of the quadrupoles helps reduce the emittance growth. The reason for this behaviour is that the emittance strongly influences the divergence of the beam such that the focal beam size will be larger in the case of higher emittance.

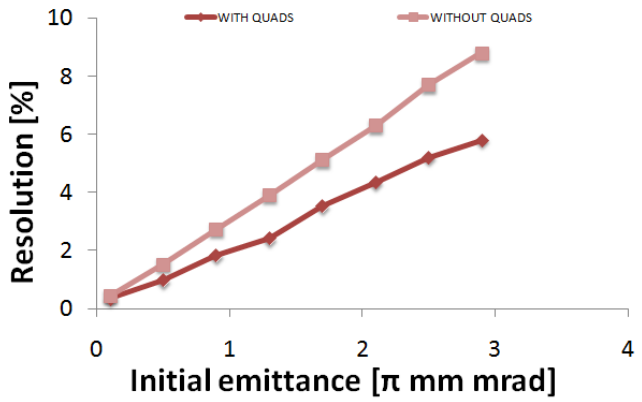

Figure 4.27: Electron spectrometer resolution as function of the initial electron beam emittance with and without the permanent magnet quadrupoles.

This is a very important result because it means that during experiments, simply by looking at the size of the electron beam on the electron spectrometer scintillating screen, it will be possible to understand if, for example by changing any laser parameter, the emittance is growing or not. Of course, this is not an emittance measurement, but it can be helpful while trying to optimise the acceleration process "on-line".

Also, if, for example, an energy spread of less than 1% is measured, then these simulations indicate that the initial emittance of the beam in that particular case should have been less than 1 π mm mrad.

4.4.3.2 The deflector simulations

The initial role of the deflector was only to bend the electrons out of the beam line without doing any spectrograph measurements, i.e. to act as an electron beam dump. In altering it to work as a compact spectrometer, the main change needed was to place a scintillating screen at the deflector output to image the electron

spectrum. To do so, a series of simulations has been performed using the GPT code changing the energy of the electrons and trying to find the optimal position both to have a very compact spectrometer and to have sufficient resolution. The bending magnet is composed of two permanent magnets with magnetic field strength of 0.75 T over a total length of 20 cm.

The GPT results are summarised in fig. 4.28. Because of the reasonably high field strength and long length of the deflector, even a 1 GeV electron beam will be slightly deflected from the propagation axis and still be visible on the scintillating screen.

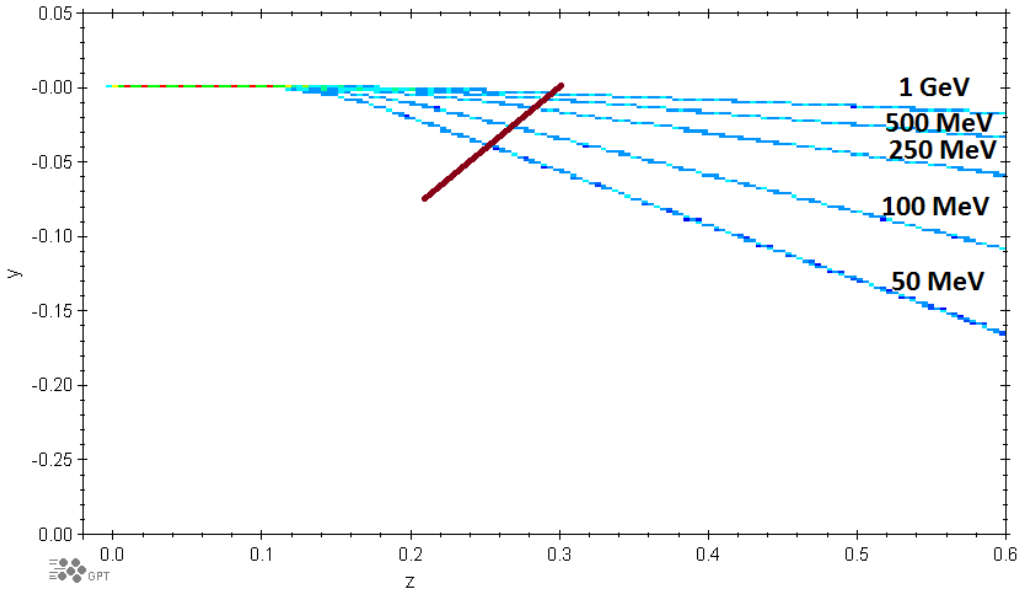

Figure 4.28: GPT simulations of the trajectories of electron bunches of different energies passing through the deflector and position of the scintillating screen (red line).

Figure 4.28 shows that the further away from the magnet is placed the scintillating screen, the better will be the resolution. However, because there is already a high resolution electron spectrometer on the beam line (as illustrated in the previous section), the final decision has been to sacrifice some resolution while keeping the compactness of the spectrometer. The red line in fig. 4.28 shows the final position of the scintillating screen. The importance of having a second electron spectrometer placed at the end of the beam line will be more evident in the next chapters but,

just to give an idea, it has allowed simultaneous measurement of the undulator radiation and electron spectra in order to have a direct comparison between these two measured quantities.

Figure 4.29 shows the design of the vacuum chamber holding the scintillating screen. Lanex is used as the scintillator in this case and, with the given viewing range of the CCD camera, the detectable energy range available here was 50 - 250 MeV. As stated above, re-positioning the CCD camera would allow higher energy electrons to be imaged if necessary.

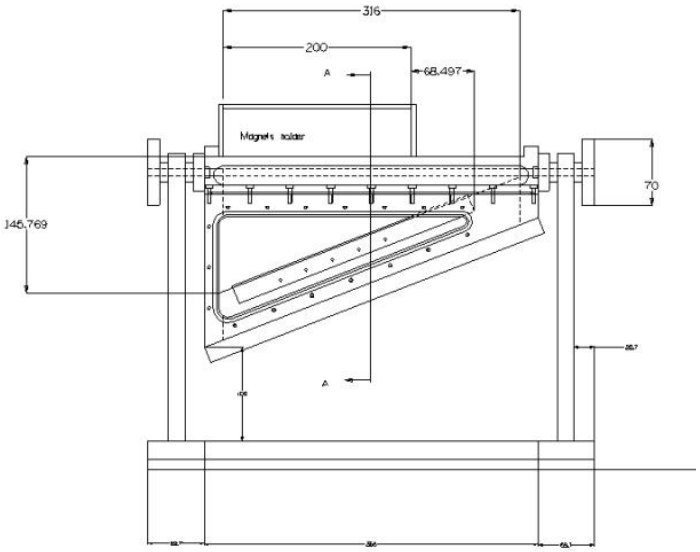

Figure 4.29: Deflector vacuum chamber design.

In order to calculate the resolution of the deflector, the same type of simulations as carried out for the main electron spectrometer has been performed. A 3.5% resolution has been calculated for a 130 MeV electron beam.

4.4.4 Benchmarking GPT against TRANSPORT

In this section, simulations that have been performed with the well-known code TRANSPORT will be described. TRANSPORT is a very powerful transport code which considers space-charge effects and first and second order solutions of the motion

equations [143]. The aim of this work is to understand if TRANSPORT and GPT are giving consistent results when considering the ALPHA-X beam line.

The first test is to have a look to the initial beam parameters defined in both codes (which are summarised in table 4.9) and understand the differences between the two codes.

GPT	**TRANSPORT**
Bunch radius dr	x radius x
Emittance ε	x divergence x'
Bunch length $d\ell$	y radius y
Lorentz factor γ	y divergence y'
Energy spread $d\gamma/\gamma$	Bunch length $d\ell$
	Momentum spread dp/p
	Momentum p_0

Table 4.9: Initial parameters for GPT and TRANSPORT.

Basically the two codes describe the beam in the same way, but GPT uses information such as emittance, Lorentz factor and energy spread, while TRANSPORT uses slightly different parameters, such as horizontal and vertical divergence, momentum and momentum spread. However, these parameters are related to each other by the following formulae:

$$p_0 = \frac{E}{c}[GeV/c] \qquad [4.4]$$

$$dp/p = dE/E = d\gamma/\gamma \qquad [4.5]$$

$$\varepsilon(rms) = \gamma\sigma_x\sigma_x' \text{ , } where\ \sigma_x = \pi dr^2 = \pi xy \qquad [4.6]$$

and, therefore, it has been easy to describe the same electron beam parameters in both codes. The other issue that makes the two code inputs different is the way of defining the magnetic field of the magnetic sources. In fact, in GPT, the magnetic field is given as the maximum magnetic field in a pole, while TRANSPORT uses the

pole tip magnetic field value. Of course, the latter is slightly higher than the maximum magnetic field in the pole (because at the tip there is a sum of magnetic fields). Once that the correspondence between the whole set of input parameters has been confirmed, it has been possible to compare the results produced by the two different codes.

Figures 4.30 and 4.31 show the beam envelopes for two different energies (250 MeV and 450 MeV) calculated using the two codes. These plots clearly show good agreement between the two codes: the only difference here is the effect of the undulator on the beam, mainly caused from the fact that, for GPT, the field map of the real undulator has been used while, for TRANSPORT, the undulator has been simulated as an array of dipoles with alternate field (internal model).

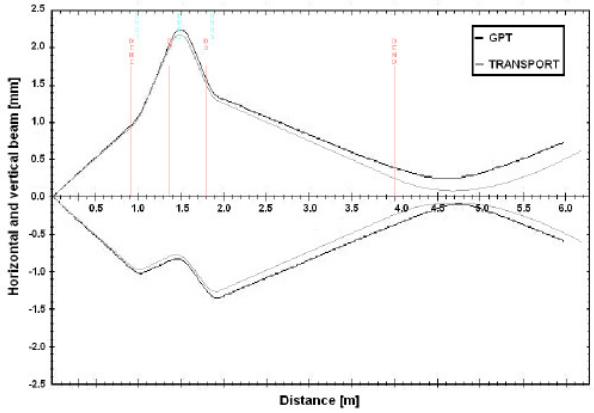

Fig. 4.30: 250 MeV energy beam envelope carried out with TRANSPORT and GPT.

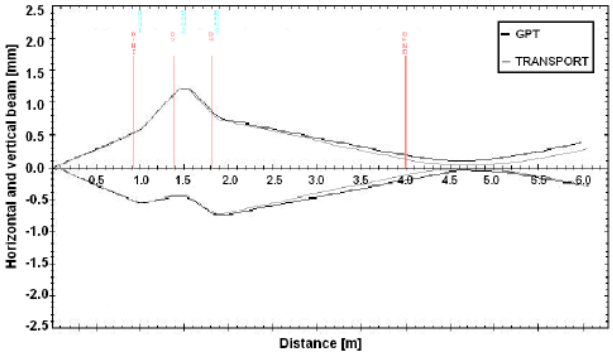

Fig. 4.31: 450 MeV energy beam envelope carried out with TRANSPORT and GPT.

4.4.5 Latest design

The last step in the design of the primary transport section is to take into account the requirements to operate an FEL and the typical energies coming out from the ALPHA-X accelerator. In particular, previous experimental campaigns have resulted in the production of stable 130 MeV electron beams. In Chapter 3, the beam quality required to drive an FEL saturating at 1.8 m from the undulator entrance has been studied and details of the electron beam quality requirements are summarised in table 4.10.

Bunch length	0.3 μm
Bunch charge	5 pC
x emittance	1 π mm mrad
y emittance	1 π mm mrad
Energy spread	0.01
x beta function (average)	1.5 m
y beta function (average)	1.5 m

Table 4.10: Electron beam quality required to operate an FEL.

The goal of this section is to see if, using the whole beam line set-up, an optimum position for the permanent quadrupoles that can satisfy the beam quality required for the FEL can be found. The parameters summarised in table 4.10 can be divided in two sets: in one set are parameters that only depend on the acceleration process and, therefore, don't change with the transport and the other set contains parameters that can be controlled by using an optimised transport. The parameters that are independent from the transport are electron energy, energy spread and partially the bunch charge (because poor transport will cause a loss in bunch charge), while the parameters that can be optimised with the transport system are bunch length, emittance and beta function.

The strategy to use in order to keep the bunch length short is to place the permanent quadrupole triplet very close to the gas jet (as already discussed in previous sections), so the problem can be to find the position of the quadrupoles in order to have a bunch length at the undulator entrance that is no longer than 0.3 µm, which corresponds to a duration of 1 fs. To do so, it is possible to iterate the GPT simulations until the output value of the bunch length is the desired value, using as variables the position of the triplet and the spacing between each quadrupole. In particular, for an energy of 130 MeV, it has been found that the optimum position of the quadrupoles with respect to the exit of the accelerator is the one summarised in fig. 4.32. Using this spacing and displacement, the matched transport obtained with GPT simulations is shown in fig. 4.33.

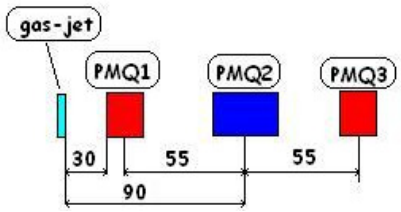

Figure 4.32: Optimal spacing between the quadrupoles for a collimated beam output at 130 MeV. Lengths in millimetres.

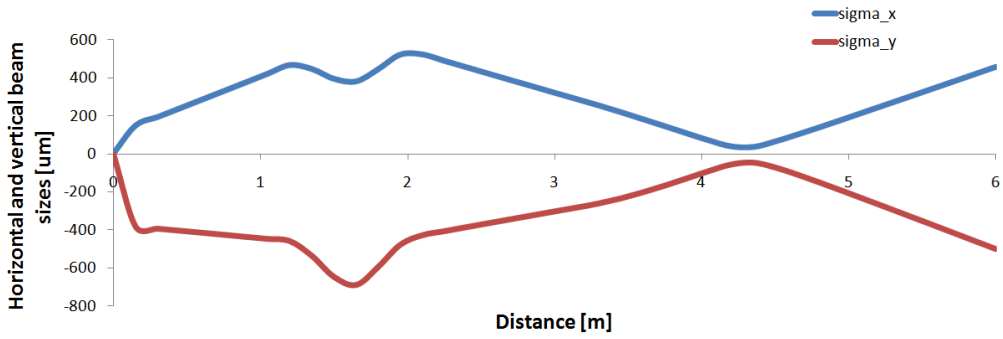

Figure 4.33: Development of the horizontal and vertical beam envelopes showing an optimised transport of an electron bunch with an energy of 130 MeV.

It is evident from fig. 4.33 that the electron bunch exiting the triplet of permanent magnet quadrupoles is a quasi-collimated beam. The focus of the bunch is obtained

using the triplet of electromagnetic quadrupole and it is placed at the centre of the undulator; moreover, the obtained beta function is close to 1 m.

The bunch length is shown in fig. 4.34: the effect of the quadrupoles is to reduce significantly the lengthening of the bunch duration (compared to fig. 4.3 and 4.10). Using the optimum spacing, it is possible, in fact, to have a bunch that is shorter than 1fs at the undulator entrance, as required from FEL simulations (table 4.10).

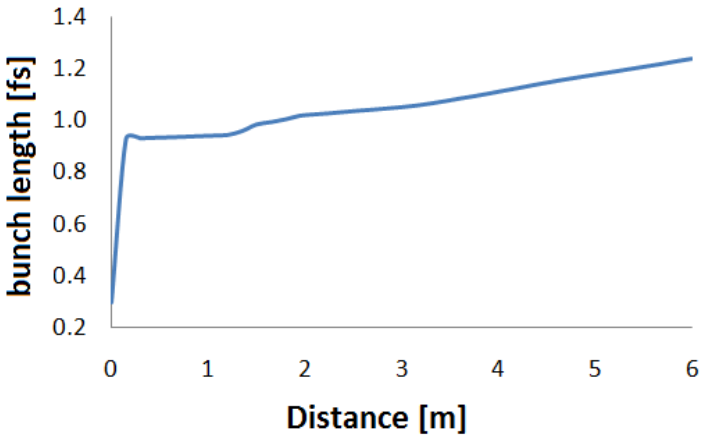

Figure 4.34: Optimised lengthening of the bunch duration of an electron bunch with an energy of 130 MeV.

4.5 Discussion

In this chapter, all the simulations that have been performed for transporting the electron bunches along the ALPHA-X beam line have been presented. In particular, the first set of simulations, that have been performed to design a triplet of permanent magnet quadrupoles, have been shown. Once the final design of the permanent magnet quadrupole triplet was ready, the whole beam line has been simulated, including the new triplet and the real model of the undulator.

A series of simulations showing the performance of the quadrupole have been presented, including the behaviour of the quadrupoles for off-axis propagation. The results show that the new triplet of quadrupoles will help for pointing instabilities, being able to always focus the electron bunch to the desired point. In particular, all

the simulations have been performed using the GPT code and eventually compared with the well-known TRANSPORT code; the results of this comparison show that there is an excellent agreement between the two codes. The last set-up for matching conditions to drive an FEL has been presented. The simulations show that it is possible to match the FEL requirements, thus, providing a strong motivation to perform the experiments.

It is important to summarise the expected beam size using two different settings for the permanent magnet quadrupoles. The first setting has the permanent magnets attached to each other (zero separation) while the second is that designed to match the FEL limits. For both cases, a comparison is made of the x and y dimensions of the beam (sigma rms). In the first case, the expected beam sizes for an electron energy of 80 MeV are given while, in the second case, the electron energy is 130 MeV. In particular, in table 4.11 and 4.12, the beam sizes are given at three different positions, which correspond to the three different imaging screens present in the beam line. These dimensions will be very useful in chapter 6, where they will be compared with the experimental data.

	Energy	L1	L3	L4
x dimension	80 MeV	1.2 mm	1.45 mm	1.3 mm
y dimension	80 MeV	1.0 mm	0.9 mm	2.0 mm

Table 4.11: Expected beam size with quadrupoles attached to each other for an 80 MeV electron beam.

	Energy	L1	L3	L4
x dimension	130 MeV	285 µm	219 µm	217 µm
y dimension	130 MeV	412 µm	232 µm	234 µm

Table 4.12: Expected beam size with quadrupoles optimised for a 130 MeV electron beam.

Chapter 5

Experimental setup

5.1 Introduction

This chapter will introduce the experimental set-up, in particular the laser system, including the laser diagnostics. It is vital to have a stable and well aligned laser beam for the experiments. A description of the ALPHA-X beam-line will detail the electron beam diagnostics: beam profile monitors, charge measurement, energy spectrum and transverse emittance. Characterisation of the beam quality, which is defined from those quantities, is important for the success of any experiment.

5.2 Femtosecond laser system

The laser system used in the ALPHA-X project is a 30 TW Ti:Sapphire chirped pulse amplification (CPA) system. A flow chart of the laser layout is shown in fig. 5.1.

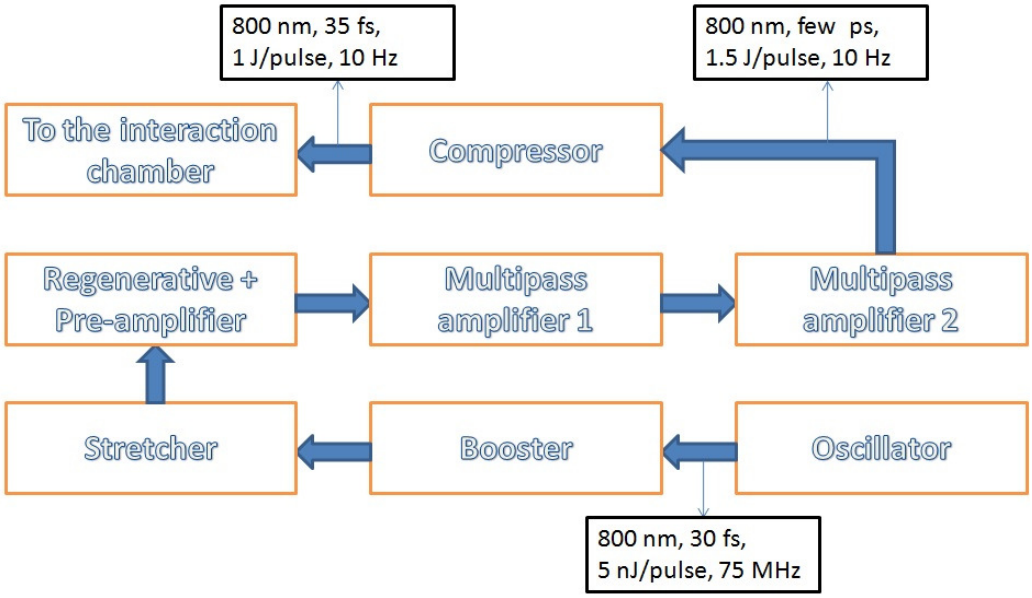

Figure 5.1: Flow chart schematic of the ALPHA-X laser chain.

The first element of the laser chain is the oscillator, that uses the Kerr self-mode locking mechanism [144], to produce a pulse train at a repetition rate of 75MHz.

Each pulse has a central wavelength of 800 nm, energy of about 5 nJ and duration around 30 fs.

The booster follows the oscillator. This element is not a standard element of a CPA-based laser system, but has been introduced to optimise the temporal contrast ratio between the main femtosecond pulse and pre- and post-pulses and pedestals on the picosecond and nanosecond timescales. It mainly consists of a multi-pass amplifier that amplifies the laser pulse train by a factor of 10^4 followed by a saturable absorber to clean the pulse. The saturable absorber is a filter that has different transmission properties according to the incident laser intensity; it behaves as an opaque filter at low intensity and become transparent at high intensity. In this way, the saturable absorber does not transmit the pedestal and pre- and post-pulses but only the main pulse. The specified contrast ratio for the laser system is 10^6:1, i.e., the ps background is 6 orders of magnitude less intense than the main pulse. A low contrast ratio in a LWFA is definitely something to avoid, because it inhabits the acceleration process, as investigated in references 145, 146 and 147. Finally, in the booster, there is also a Pockels cell ("pulse picker") that generates a pulse train of 10 Hz from the input 75 MHz train of the oscillator.

After the booster, the laser pulses enter the stretcher. The objective of this element is to produce a temporal chirp on the beam. This is achieved mainly by two diffraction gratings: they stretch the beam in time such that the output pulse is much longer than the input one. In this way, it is possible to amplify the signal without destroying the amplifier optics, since the energy of the pulse will be distributed in time as well as the pulse. This is the basis of the CPA scheme developed in the 1980s [148] (section 2.2.1).

After the stretcher, there are a series of amplifiers to reach the high peak power. Firstly, the regenerative amplifier and the pre-amplifier amplify the laser pulse by a factor of 10^4. At the output of this element, the laser pulse energy is around 25 mJ.

Then there are two multi-pass amplifiers (located between them is a spatial filter). The first multi-pass amplifier increases the laser pulse energy from 25 mJ to 300 mJ. The spatial filter cleans spatially the pulse profile before the final amplifier that

amplifies the pulse energy up to 1.5 J. In this case, the amplifying medium is a Ti:Sapphire crystal cooled to -150°C by a cryogenic pump.

Once the pulse is amplified, it needs to be compressed again in time. From this stage on, the beam needs to be in vacuum to avoid both damage on the optics and beam profile degradation. Compressed beam travelling in air can, in fact, can easily ionize the surface of the mirrors and cause the burning of the coating. The compressor introduces a chirp to the beam that has the opposite sign with respect to that in the stretcher: now the beam has a very short pulse duration with a very high peak power. This beam is transported to an f/18 on-axis spherical mirror, which will focus the pulse to a 40-50 μm spot size (diameter at $1/e^2$). The pulse energy at the interaction point is about 1 J, with a pulse duration of about 35 – 40 fs.

5.2.1 Laser diagnostics

In order to constantly check the laser status, there are many different laser diagnostics. Some of those are used as a daily procedure and some are used periodically.

The first daily diagnostic is the laser power meter to read the oscillator output power. It is very important to take this measurement every day because a drop of power in this point will cause a drop of power in the whole laser chain. If this power drops, it is important to check the oscillator for misalignment or simply clean some key optical components.

The energy of the laser is also measured every day at some key points in the laser chain: at the output of the preamplifier, after the spatial filter and at the output of the final amplifier. Any energy drop requires a check of the alignment and, possibly, a clean of the optical components. Also, this diagnostic can be used to measure the efficiency of the laser pulse transport, in particular, for the compressor efficiency that typically is ≈ 65%. An ultraviolet cleaning system is in place to periodically clean the gratings in the compressor chamber.

Another important diagnostic is the laser spectrum before the final amplifier: this measurement will give information on the laser spectrum shape and bandwidth. A typical laser spectrum is shown in fig. 5.2. The central wavelength of the laser is around 810 nm, the spectrum bandwidth is 35 nm and the spectrum is flat top. The spectrum can easily drift in band and the farer it is from 800 nm, the worse will be the transmission in the laser chain. In fact, all the laser optics is designed to transport (with 99% efficiency) a laser with a central bandwidth of 800 nm. That's why it is so important to diagnose the bandwidth in a daily based procedure.

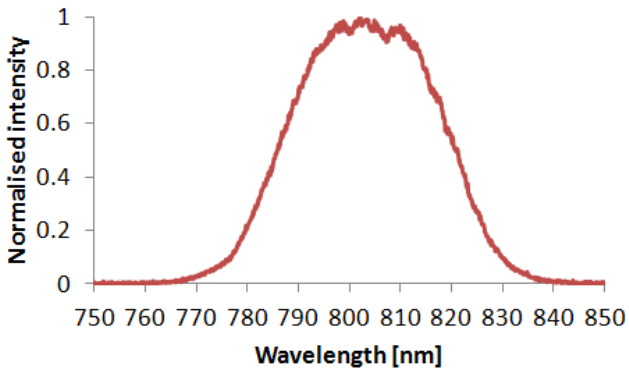

Figure 5.2: Typical laser pulse spectrum from the ALPHA-X laser system before the final amplifier.

The shape of the spectrum is also very important. It is fundamental to have a flat-top spectrum: a hole in any part of it, will make the pulse to behave like a double beam and many undesired non-linear processes can happen (for example, part of the beam could be amplified much more than the other parts). To ensure the flatness of the laser bandwidth, an optical component called a "Dazzler" is used. This is an acousto-optic modulator capable of shaping spectral phase and amplitude of ultra-short laser pulses. It is a programmable spectral filter which uses travelling acoustic waves to induce variation in the optical properties thus forming a dynamic volume grating.

The next daily based diagnostic is the imaging of the laser spot on the final amplifier crystal. The expensive Ti:Sapphire crystal needs to be carefully monitored for signs of damage. In order to constantly check its status, an imaging system enables

viewing of the back of the crystal on a video screen. Usually a damage of the crystal is immediately visible as indicated by very bright white dots on the screen. As in the case of the normal optics, those bright dots can also be due to dust on the crystal, and it is important to act on this information immediately to limit damage in the laser chain.

The other imaging system that is also used on a daily basis is placed in the acceleration chamber. In this case, a wedged mirror can be inserted and removed from the beam line with a stepper motor. A CCD camera on the top of the vacuum chamber images this mirror: in this way, the profile of the laser beam at the focus can be checked. Damage can be seen as a black spot in the imaged laser beam.

The last daily based diagnostic is represented by a couple of calibrated diodes used to check the laser energy during the experiment. Probably this is the most useful on-line diagnostic used during the experiments. One of the diodes is placed just after the pre-amplifier and the other one is placed at the output of the final amplifier. This measurement is very useful both to keep a record of the laser energy for every shot and to check that there is no drop in energy during the experiment. As in all the other cases, a decrease in energy can be caused by laser misalignment or damage in the laser chain.

The other diode is placed just after the spatial filter that is used to check the shape of the laser beam, mainly to confirm the integrity of the filter.

The first of the occasionally applied diagnostics is the measurement of the contrast ratio. This is achieved with a Sequoia that is a commercial high dynamic range third-order femtosecond cross-correlator developed by Amplitude Technologies. It is a high precision measurement tool for the temporal pulse shape of the femtosecond laser system. A high contrast ratio is a desired aspect of any laser system: this measurement can also give information about pulse pedestals, ghost pulses and pre- and post-pulses.

Another diagnostic used periodically is a SPIDER for measuring the pulse duration. SPIDER is a spectral interferometer that uses two interfering pulses to reconstruct the temporal pulse shape [149]. This diagnostic is used after the compressor.

Finally, there is measurement of the amplified laser beam profile at the output of the compressor and at the interaction point. Probably the most important one is the latter because a high quality focal spot with maximum energy in the central region is desirable for stable electron beam production.

5.3 ALPHA-X beam line components

Figure 5.3 shows the beam line set up. The laser is coming from the right hand side and is focused to a 40 µm spot by an on-axis f/18 spherical mirror. At the focus, there is the plasma channel (that is the accelerator), which is formed in the gas profile of a supersonic helium gas jet (nozzle diameter is 2 mm).

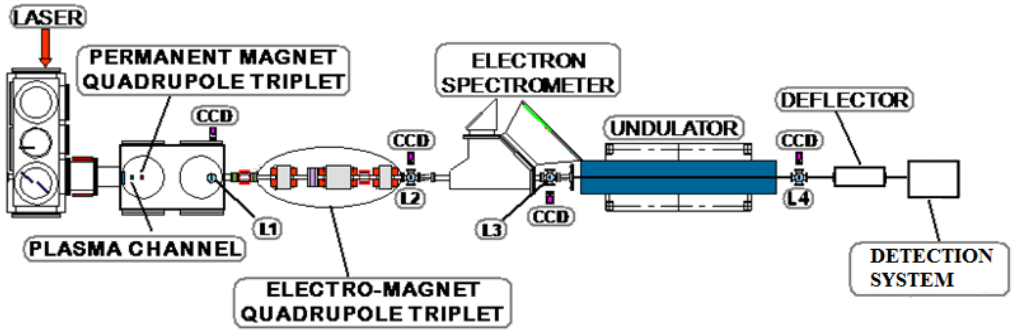

Figure 5.3: ALPHA-X beam line layout.

A table of the distances of each element with respect to the accelerator is presented in table 5.1. In particular, for the permanent magnet quadrupole triplet, two different setups are reported, corresponding to the two different transport experiments described in detail in chapter 4 and 6.

Beam line element	Distance from the accelerator
Setup 1: Permanent magnets quadrupoles	13 cm, 14 cm, 15.8 cm
Setup 2: Permanent magnets quadrupoles	3 cm, 9 cm, 13 cm
Lanex L1	60 cm
Electromagnetic quadrupoles	1.12 m, 1.499 m, 1.878 m
Lanex L2	2.091 m
Electron Spectrometer ES1	2.386 m
Lanex L3	3.179 m
Undulator	3.411 m
Lanex L4	5.198 m
Electron Spectrometer ES2	5.304 m

Tab. 1: Position of the ALPHA-X beam line components with respect to the accelerator exit.

5.3.1 Gas jet accelerator

The geometry of the gas jet nozzle (designed and constructed in-house) is shown in fig. 5.4.

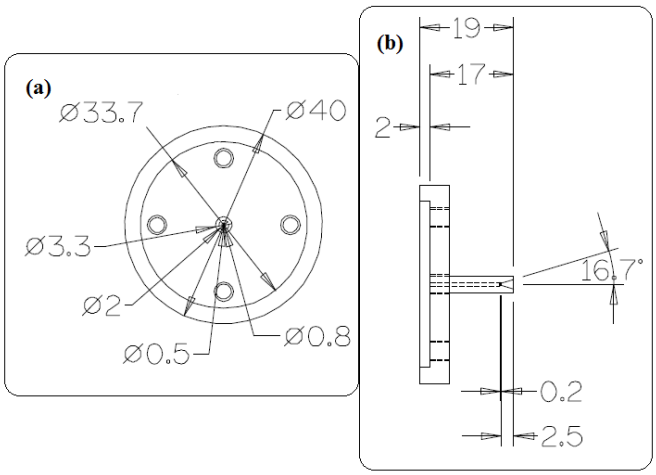

Figure 5.4: (a) Top-view and (b) side-view of the brass gas-jet nozzle. Length units in mm.

The mechanism of operation is straightforward: the gas is injected by a gas transport line, which is partially in air and partially under vacuum. To limit the gas flow into the vacuum chamber, a solenoid valve (normally closed) is used; this valve is opened just before the laser arrival, thus minimising the flow of gas onto the vacuum. Mounted on the top of the solenoid valve is the a gas jet nozzle, specially designed to have a sharp edge of the gas column. The opening angle of the nozzle defines the maximum acceleration length achievable (depending on the distance between the gas jet and the laser beam).

The laser beam is focused at the beginning of the gas column for self-ionisation and plasma wave formation (fig. 5.5). The sharpness of the gas flow is very important: a column of gas which has turbulence (shocks) inside is generally not ideal for acceleration because it creates strong plasma density variation along the laser path. This topic is studied in detail elsewhere [150].

Figure 5.5: Laser beam focused in a gas-jet.

Thomson side-scattering is used to image the plasma channel as shown in fig. 5.6. Mainly the images has been recorded using Thomson scattering of the source (due to electron-photon collisions during the laser-plasma interaction). In particular, fig. 5.6a, shows a good quality plasma channel, where the intensity of the scattered light is quite homogeneous along the whole channel (which is 2 mm long). On the other hand, the channel shown in fig. 5.6b can be considered a poor channel because of the shortness of the channel itself (only 1.6 mm with a hole in the centre) and because of the inhomogeneity in intensity.

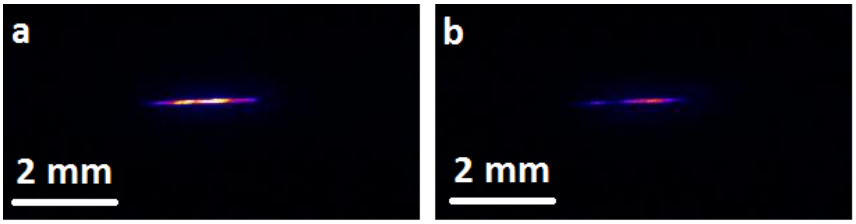

Figure 5.6: Plasma channels from a helium gas jet imaged by Thomson side scattering.

5.3.2 Electron beam diagnostics

The precise knowledge of the beam quality during the undulator experiment is of crucial importance and the most important characteristics of a bunch are the divergence, charge, energy spectrum and transverse emittance. There are many different schemes proposed in literature to measure these quantities [150-151]; in the experiments described in this thesis a single shot approach has been applied.

The methods used include imaging of the beam using scintillator screens to characterise the beam divergence and therefore the beam profile, imaging plates absolutely calibrated to determine the charge of the bunch, two magnetic spectrometers for energy spectrum measurement and a pepper-pot mask to measure the transverse emittance.

Once all those measurements have been carried out, it is then possible to use the one diagnostic to characterise more than one quantity. For example, once that the scintillator screens have been cross-calibrated using the imaging plates, they can be used to not only measure the beam profile but also its charge.

5.3.2.1 Beam profile measurement

To measure the beam profile, a series of pop-in Lanex screens have been installed in the beam line, each imaged by a CCD camera (POINT GREY, FLEA-FL2-14S3). A Lanex screen is a scintillator screen which employs a $Gd_2O_2S:Tb$ inorganic scintillator with high conversion efficiency of both X-ray and electron detection [152]. It has been reported to give similar energy absorption per electron for electron energies

from 10 MeV to 500 MeV so it is a good candidate for LWFA electron imaging [153]. Lanex emits in the blue-green spectral region with a strong component at 548 nm, which is a good wavelength for imaging with standard silicon CCD cameras.

The knowledge of the beam profile is very important because it can give a lot of information about the beam quality, mainly regarding the divergence of the beam. An example of beam imaging is shown in fig. 5.7.

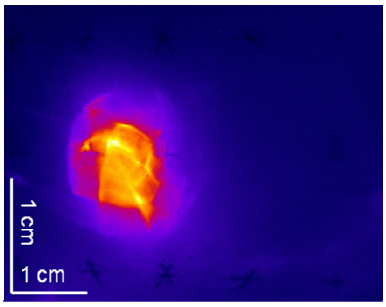

Figure 5.7: Beam profile imaged at the exit of the plasma source as measured on Lanex L1.

By knowing the initial source size (which is only few μm), the divergence of the beam can be estimated by calibrating the CCD camera, such as shown in fig. 5.7 for an electron beam profile captured on Lanex L1. There is also a qualitative measure of the quality of the beam: it can be seen, for example, if the electrons are bunching, how much wide divergence halo is present as well as the pointing stability and degree of symmetry or ellipticity.

There are four Lanex screens along the beam line, as shown in fig. 5.3. Lanex L1 is mounted at 45° with respect to the propagation axis and directly imaged by the CCD camera. All the other screens (L2, L3 and L4) are placed perpendicular to the beam with a mirror at 45° on the back side that is used for the imaging system.

5.3.2.2 Charge measurement

Measurement of the absolute beam charge has been conducted using Fuji BAS imaging plates. An imaging plate (IP) is a two-dimensional detector of ionising radiation (X-rays, energetic particles etc) consisting of a 100 μm layer of barium fluoro-halogenite doped with europium 2+ ions on a polyester substrate. Electrons

excited from EU^{2+} ions by incident ionising radiation are trapped in a metastable state and the trapped states can decay if de-excited by light at 632.8 nm, which is how IPs are read out in a scanning system to extract their stored data. As the metastable state decays, blue light at 400 nm is emitted in a process known as photo-stimulated luminescence (PSL). The number of these emitted photons in the read-out process is proportional to the total absorbed radiation energy. Since the IP scanner digitises the plate readout using a logarithmic amplifier [154,155], the measured pixel data have to be converted between this value, or quantum level (QL), to a linear PSL scale [156]:

$$PSL = \left(\frac{R}{100}\right)^2 \times \left(\frac{4000}{S}\right) \times 10^{L\left(\frac{QL}{G} - \frac{1}{2}\right)} \qquad [5.1]$$

where R is the scanning resolution in μm, S and L are the scanner sensitivity and latitude, respectively, and G is the bit depth for 16-bit. The calculated PSL value is a floating-point number that can either be above or below unity. The IP used during the experiment was covered with an aluminium foil to ensure that it was not exposed to laser light. Sometime after irradiation the stored information was read out with a reader/scanner, giving the two dimensional scanned map in QL units.

The charge has been measured in many places along the beam line. Mainly it has been measured close to Lanex screen positions L2, L3 and L4, which has allows a cross-calibration of each screen to be carried out. It is not practical to calibrate L1 in the interaction chamber because of the noise present and space and access limitations. At the other Lanex positions, a series of IPs have been mounted in a rotatable holder (carousel) located in front of the respective Lanex. Any one IP can then be rotated into the beam line axis and exposed to one electron beam shot. With the IP positioned in front of the Lanex, the electron beam will also interact with the Lanex, i.e., the charge profile is captured simultaneously on the IP and the Lanex. So this is a direct cross-calibration method for calibrating the Lanex. An example of the measurement is shown in fig. 5.8.

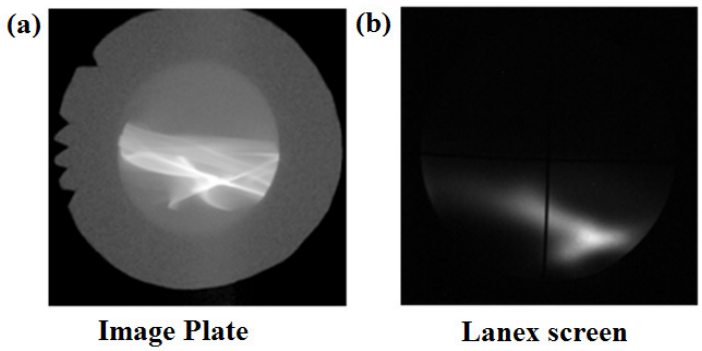

Figure 5.8: Measurement of the charge using imaging plates; (a) IP image after read out and (b) simultaneous image of the electron beam on the Lanex screen L3.

After recording data on all the image plates, they have been read using a scanner and the data has been processed using eq. [5.1]. Using this method, a charge up to 20 pC has been measured on L2 while, on L3 and L4, the maximum charge measured is 5 pC and 3.5 pC respectively.

As far as the Ce:YAG screen of the electron spectrometer (ES1) and the Lanex screen of the bending magnet spectrometer (ES2) are concerned, they have each been cross-calibrated indirectly by collecting 100 shots on the near-by calibrated Lanex (L3 for ES1 and L4 for ES2) and 100 shots on the spectrometer and comparing the number of counts. This relies on the good stability of the acceleration to assume that the average charge for each collection of shots is the same to within experimental uncertainty.

5.3.2.3 Energy spectrum measurement

The energy spectrum of the accelerated electron beams has been measured using two different spectrometers, as described in detail in section 4.4.3. The first one (ES1) is placed 2.4 m from the source and it is a high resolution imaging spectrometer. The second one (ES2) is placed 5.5 m from the source, just after the undulator, and it is a low resolution simple bending magnet spectrometer. The two spectrometers are very different in their setup and response; the first one is a dynamic electromagnetic field spectrometer, the second one is a permanent field spectrometer. This means that the resolution of the former is energy dependent

while mainly for the latter it is not. Moreover, the first spectrometer is designed to introduce, together with the dispersion field, a quadrupole-like field to focus the beam in the non-dispersive axis.

Let's consider the simple image in fig. 5.9. It shows the geometry of each configuration: x is the dispersion axis, i.e., the axis that will resolve the energy spectrum of the electron bunch; z is the propagation direction of the electrons and y is the non-dispersive axis or better the axis where, for design, ES1 will focus the beam. The geometry is the same for ES2, except for the absence of focusing in the y axis. Another important characteristic of ES1 is that it has two different scintillator screens, one is used to measure the electron bunches with a very high resolution but it is limited in energy (it can measure up to 100 MeV), while the other one has a slightly lower resolution but can measure electron bunches from 10 MeV up to 650 MeV (depending on the field strength).

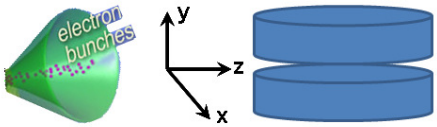

Figure 5.9: Electron spectrometer – geometry of the configuration.

The energy spectrum measurements have been carried out with different scintillator materials for the two spectrometers. The first spectrometer uses Ce:YAG crystal (thickness 1 mm) while the second one uses a Lanex screen. The main difference between these two scintillators is the spatial resolution. In fact, the spatial resolution of the dynamic spectrometer is around 50 µm while the Lanex screens are usually quoted as having 100-150 µm resolution.

5.3.2.4 Transverse emittance measurement

The measurement of the bunch emittance has beam achieved using a pepper pot mask [22]. This technique uses a mask with a grid of tiny holes laser-micromachined in a thin sheet of dense material to split the beam into small beamlets that drift to a

scintillator screen. The measurement of the beamlet's position and size yields the beam divergence which, combined with the measurement of the total beam size, gives the emittance [157]. The scintillator screen is a thin Ce:YAG crystal and the detector is a high resolution CCD camera. As in the case of the dynamic spectrometer, the spatial resolution of the scintillator screen is around 50 µm per pixel. For this kind of measurement it is very important to have a very high spatial resolution because the beamlets diverging from the mask are very small [157,158]. The size of the beamlet on the imaging system depends on the beam emittance and on the distance between the mask and the crystal; in case of zero emittance, the size of each beamlet is the size of the hole (25 ± 5 µm).

5.4 The Free-Electron Laser section

In this section, the portion of the ALPHA-X beam line devoted to the undulator and UV radiation detection system (shown in fig. 5.10) is described. The main element is the undulator, which will be described in the next section: this is where the radiation will be produced. The quality of the radiation depends on the injected electron beam and, therefore, it is very important to check the stability and size of the beam using scintillating screens. Therefore Lanex 3 and Lanex 4 are also part of this section. Another element that is part of the FEL section is the deflector ES2, which dumps the electrons from the beam line.

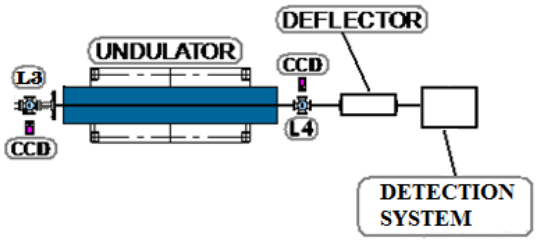

Figure 5.10: The ALPHA-X free-electron laser section.

The last element is the detection system. Many different schemes of detection have been used during the experiments and they will all be described. Lastly, as part of the detection system, filters that have been used during the experiments will be described and the problems encountered by using them will be discussed.

5.4.1 Undulator

The undulator used for the experiment is a 1.5 m long undulator designed by the ASTeC team at Daresbury Laboratory (STFC) [159]. It is a slotted pole planar design and the tuneable pole gap is set at 8.0 mm for these experiments (vacuum tube inner radius is 6 mm), made of 100 period permanent magnets with alternating field polarity with a peak on-axis magnetic field strength of 0.27 T. The undulator period is λ_u = 15 mm and therefore the undulator deflection parameter is a_u = 0.38. Moreover, the undulator is specially designed to slightly focus low energy beams (up to around 90 MeV, see fig. 4.14) which is an important aspect considering that usually low energetic beams have a larger divergence which makes them more difficult to focus with a longer beta function.
Figure 5.11 shows the design of the ALPHA-X undulator. The only difference is that the undulator is rotated by 90° in the real experiment.

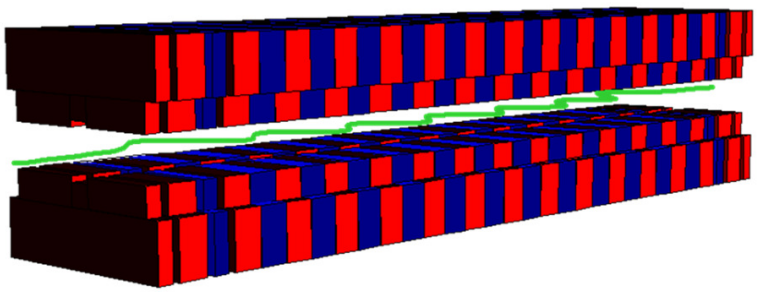

Figure 5.11: The ALPHA-X slotted pole planar undulator.

As already discussed in section 3.2, the FEL amplifies externally injected or spontaneously emitted radiation by inducing wavelength-scale micro-bunching of a relativistic electron beam with a periodic ponderomotive force arising from the

combination of a periodic undulating force and an injected electromagnetic wave. In practice, the undulator acts as amplifying medium: the magnetic field provides a periodic transverse acceleration to the injected electrons, which in turn produces electromagnetic radiation. The wavelength of this radiation is proportional to the spacing of the magnets (undulator period) and inversely proportional to the square of the electron energy. This gives a tremendous tuning range for the radiation. The possible degrees of freedom are the undulator gap size and the electron energy: by changing these two parameters it is possible to easily tune the emitted radiation wavelength. To obtain the shortest possible wavelength one can minimise the undulator period or, more effectively, maximise the electron energy.

5.4.2 Detection system

During the undulator experiment, different detection systems have been used. The simple initial set-up was a CCD camera with an objective lens to image the centre of the undulator (the focal point of the objective was around 1.5 m from the camera). Then the camera objective has been replaced with a series of lenses (a 1.5 m collimating lens followed by a 10 cm focusing lens) and the CCD camera has also been upgraded. The next step saw the replacement of the camera with an ORIEL spectrometer coupled to a 1 x 2000 pixel silicon detector. Because of the difficulties in the alignment process, the silicon detector has been replaced with a 250 x 2000 pixel HAMAMATSU detector. In this set-up, the first undulator radiation spectra have been recorded in the visible region. During the experiments, 3 different spectrometer diffraction gratings have mainly been used, all with a high transmission in the visible region. In particular, the blaze wavelength of the gratings is summarised in table 5.1.

Grating	Blaze wavelength [nm]	Line per millimetre
77491	400	600
77493	350	400
77488	350	1200

Table 5.1: Blaze wavelength of the radiation spectrometer gratings used during experiments. Grating labels refer to Newport Spectra Physics part numbers.

An example of the absolute efficiency of one of the gratings (no. 77491) is shown in fig. 5.12.

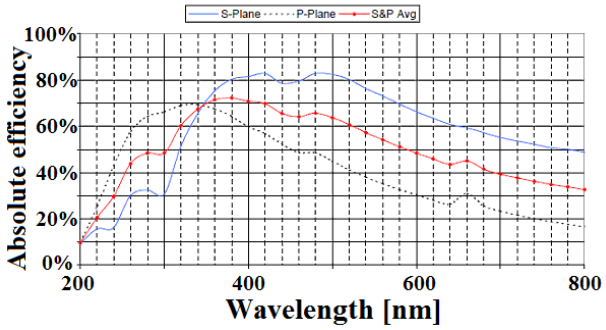

Figure 5.12: Grating efficiency of grating no. 77491 used for calibration correction.

Another important point to take into account is that every grating has its own resolution, which is represented by the number of lines per millimetre (as shown in table 5.1). The higher this number, the better is the resolution but the range of the wavelength window is reduced.

Final experiments have been conducted with a different detection system, consisting of a McPherson, 234/302 scanning monochromator with platinum-coated toroidal mirror spectrometer coupled to an Andor Newton camera. This detection system is optimised to measure radiation in the VUV region of the electromagnetic spectrum. Three elements attenuate the radiation signal: the toroidal mirror (peak reflectivity of 65%), the grating (peak efficiency of 25% at 150 nm) and, finally, the quantum efficiency of the Andor camera (25% across the relevant spectral range). The resolution of the spectrometer is better than 1 nm.

This set-up has been used by changing the electron energy and, therefore, going to shorter wavelength. In fact, with a higher electron energy and this new detection system optimised to detect radiation at shorter wavelength (the blaze wavelength in this case is 135 nm), it has been possible to measure undulator radiation in the VUV region.

The efficiency curve of one of the gratings used during the experiment is shown in fig. 5.13. In this case, the transmission is lower than in the case of the grating used to measure visible radiation, but it is a resonable transmission for the VUV radiation range.

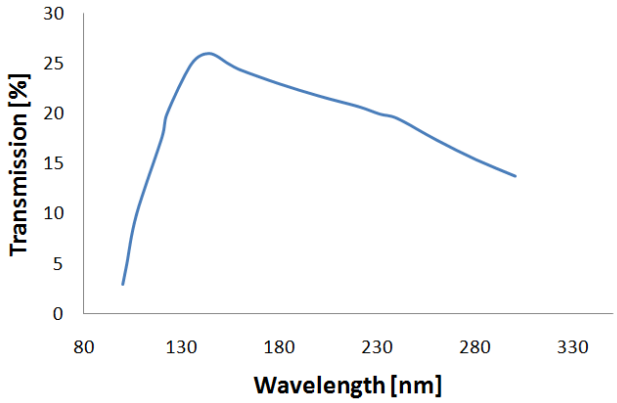

Figure 5.13: Grating efficiency curve for the VUV monochromator.

5.4.3 Filters

The main filters used during experiments are aluminium foils. The importance of this kind of filter is that it can efficiently block the laser beam light and the radiation coming from the accelerator. The only drawback of this kind of filter is that it can increase the emittance of the beam by a large factor. Simulations using the GEANT 4 code have been carried out in the group, showing emittance growth increase by increasing the thickness of the aluminium foil.

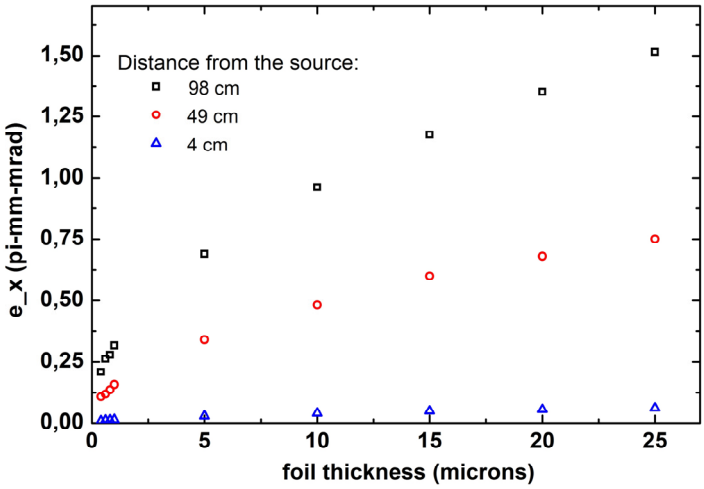

Figure 5.14: Emittance growth as function of the aluminium foil thickness (Courtesy of G. Manahan).

For the plot of fig. 5.14, an initial electron beam emittance of $1 \cdot 10^{-3}\ \pi\ mm\ mrad$ has been assumed. The simulations suggest that, to keep the emittance growth under control, it is necessary to focus the electron beam to where the aluminium foil is placed; in this way, the interaction between the particles and filter is limited and the emittance is kept at more or less the same level. Of course there is a disadvantage in doing this: if the beam is focused at the entrance of the filter, it will not be able to be focused again at the centre of the undulator (which is fundamental for efficient performance of the FEL). This will be discussed in more detail in chapter 7.

Chapter 6

Electron beam generation and transport – experimental results

6.1 Introduction

There are two experimental setups that will be discussed in this chapter. Both of them share the same laser specifications, while the beam line change concerns the spacing between the permanent magnet quadrupoles. The importance of changing this spacing is studied with respect to optimisation of the electron beam transport and, therefore, the matching conditions between the electron bunch and undulator, as discussed in Chapter 4. In that same chapter, the transport simulations have been discussed and the expected size of the beam along the beam line has been given. Here the experimental results will be shown and a comparison between the expected and measured beam sizes will be made.

6.2 Electron beams exiting the accelerator

The electron bunches exiting the accelerator are divergent and the divergence of the beam is related to the energy of the electrons: more energetic electrons have a smaller divergence because the space-charge effect is reduced. Conversely, space-charge effects are stronger at lower electron energy. In fact, considering a cylindrical electron beam, the force between each electron is given by:

$$F_r = \frac{qE_r}{\gamma^2},$$

where E_r is the radial component of the electric field (the only non-zero component of the field due to the symmetry) and q is the electron charge.

Figure 6.1 shows a typical electron bunch exiting the ALPHA-X accelerator as imaged on the first scintillating screen (Lanex L1) which is positioned 60 cm from the source. The electron beam consists of a bright central region with a surrounding halo (the low energetic electrons [160]).

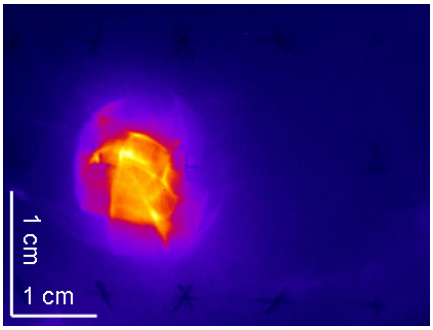

Figure 6.1: Typical electron bunch exiting the ALPHA-X accelerator as imaged on L1.

Without any strong magnetic collimation or focusing, the electron beam will keep expanding such that, even with optimal transport settings for the electromagnetic quadrupoles (EMQs) at this stage, the result on downstream scintillating screens is just a highly expanded shadow, as shown in fig. 6.2 (σ_x= 4.5 mm, σ_y=3.5 mm).

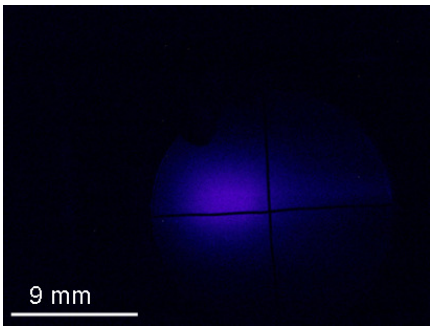

Figure 6.2: Typical electron bunch as imaged on L3 with EMQ (current settings: IQ1 = 3.2 A, IQ2 = 3.5 A, IQ3 = 3.2 A) only.

After further beam propagation passing through the undulator with imaging the beam on the final Lanex L4 (5.3 m from the source), again only a shadow is detected, as shown in fig. 6.3.

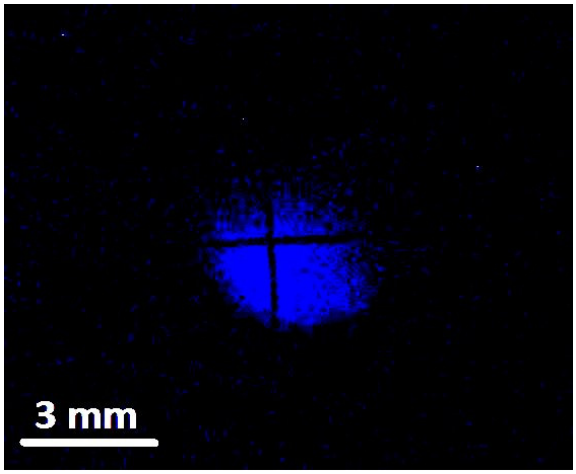

Figure 6.3: Typical electron bunch as imaged on L4 with EMQ (current settings: IQ1 = 3.2 A, IQ2 = 3.5 A, IQ3 = 3.2 A) only (colour enhanced).

It is simply concluded that it is of paramount importance, therefore, to introduce the permanent magnet quadrupole triplet into the beam line in order to be able to efficiently transport the monoenergetic part of the electron bunch through the undulator with minimal loss of charge and with beta function matching (section 4.4).

6.3 Beam transport with PMQ installation

In this section, the experiments performed using the permanent magnet quadrupole triplet introduced in section 4.3 will be introduced. In particular, two different experiments that have been carried out using those quadrupoles will be described, the first one using the permanent magnet quadrupole triplet just to reduce the divergence of the electron bunches and the second one to collimate the electron bunches (within a certain energy range) exiting the accelerator.

6.3.1 Initial results

Results have been obtained using the first layout described in section 4.3 with the PMQs attached to each other, i.e. zero separation along the beam line axis.

Figure 6.4a shows the sandwiched quadrupoles ready to be installed in the beam line and fig. 6.8b shows the quadrupoles installed in the beam line during the alignment process, which used two counter propagating He-Ne lasers as references to align both the laser beam and the beam line components.

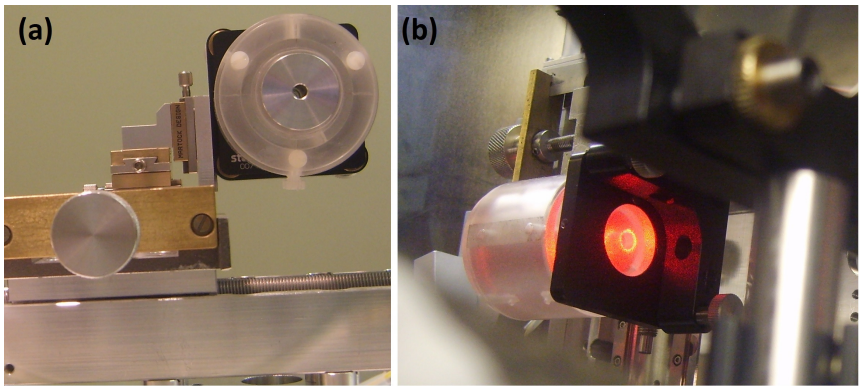

Figure 6.4: The sandwiched quadrupole configuration (a) ready to be installed in the beam line and (b) during the main alignment process.

The outer quadrupoles are attached to the central quadrupole: such a configuration is useful to reduce the divergence of the electron beam while removing the halo. This is caused by the permanent magnet quadrupoles each having a very high magnetic field gradient (≈ 500 T/m) and their effect on a low energy electron bunch is to defocus it very rapidly. In fact, as can be seen in fig. 6.5, the halo is almost completely removed after only 60 cm of propagation; only a small fraction is now visible near the main bunch.

This behaviour of the quads on a very low energy electron beam is predicted also by GPT simulations, as shown in fig. 6.6. The image shows a 3 MeV electron bunch which has encountered the triplet of quadrupoles and then is imaged on the first Lanex screen. The 3 MeV electrons pass through the quadrupoles and are immediately dispersed: there are, in fact, no electrons at all within a 5 cm radius circle centred on the propagation axis.

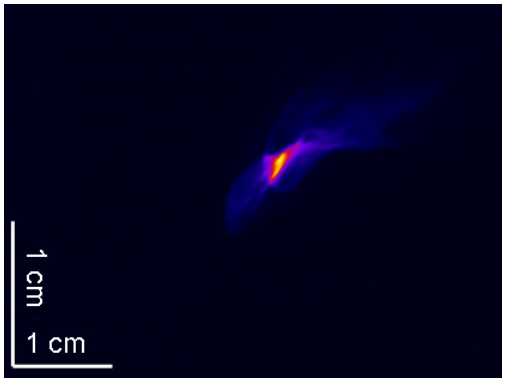

Figure 6.5: Electron beam exiting the permanent quadrupole triplet as imaged on L1.

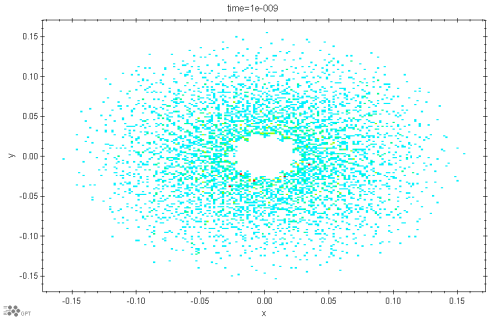

Figure 6.6: Simulation of a 3 MeV electron bunch profile (x and y in meters) after passing through the permanent quadrupoles and imaged on L1.

The electron bunch size on the first Lanex screen, which has been propagated without the use of the permanent magnet quadrupoles (fig. 6.3), can be compared to that recorded on the same Lanex but using the above described setting for the triplet of permanent magnet quadrupoles (fig. 6.5). There is a clear difference in the divergence of the beam: in the first case, the beam is quite large while, in the second case, the beam size is reduced. In fig. 6.7, there is an example of the analysed data with and without the permanent magnet quadrupoles.

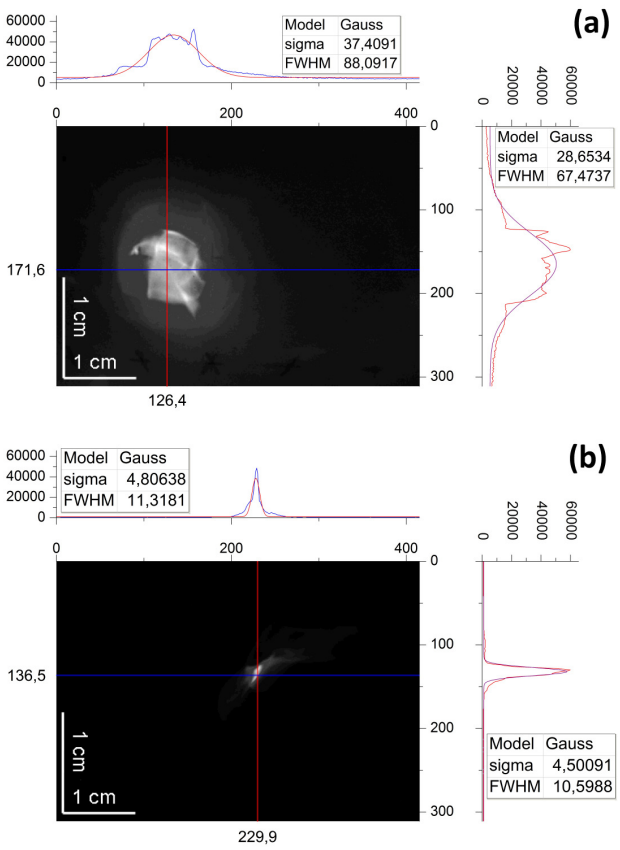

Figure 6.7: Horizontal and vertical electron beam profiles (a) without and (b) with the use of the permanent magnet quadrupoles triplet on L1.

The difference in beam size is a factor of 7.8 in the horizontal plane and a factor of 6.4 in the vertical plane. For this experiment, the mean energy of the electron bunches was 80 ± 5 MeV, as shown in fig. 6.8.

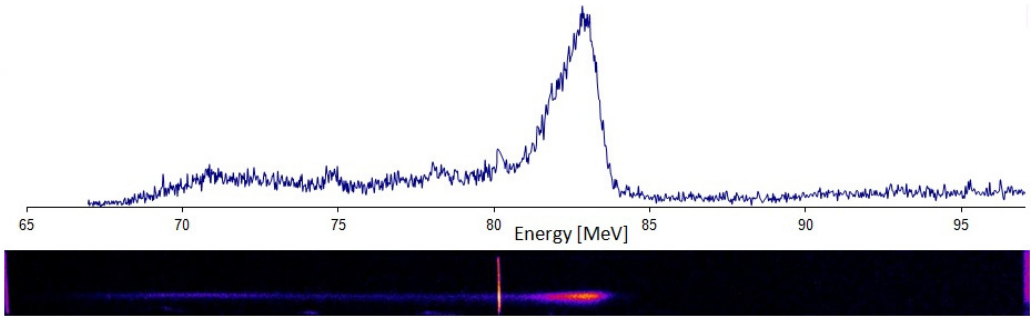

Figure 6.8: Typical electron beam energy spectrum measured during the experimental campaign with quadrupoles sandwiched as imaged on ES1 low energy window.

By removing the first Lanex screen, the electron bunch can be transported along the beam line. At Lanex L3 (3.4 m from the accelerator), the electron bunch has been transported through the triplet of permanent magnet quadrupoles and the triplet of electromagnetic quadrupoles (set using the optimisations found with GPT simulations, as described in section 4.4). An example of the electron beam on Lanex L3 is shown in fig. 6.9. The electron beam for this particular shot has the following dimensions: $\sigma_x = 663$ µm, $\sigma_y = 447$ µm.

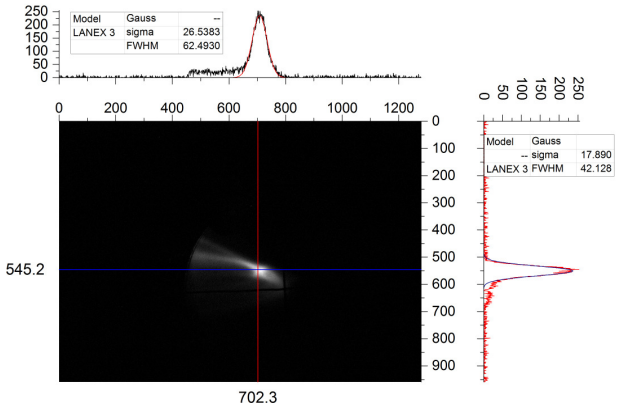

Figure 6.9: Electron beam imaged on L3, placed 3.4 m from the accelerator, before undulator.

Eventually, the beam passes through the undulator and is imaged on the last Lanex screen L4, which is 5.1 m from the accelerator, as shown in fig. 6.10. Beam radii on this shot are 750 µm in x and 1050 µm in y.

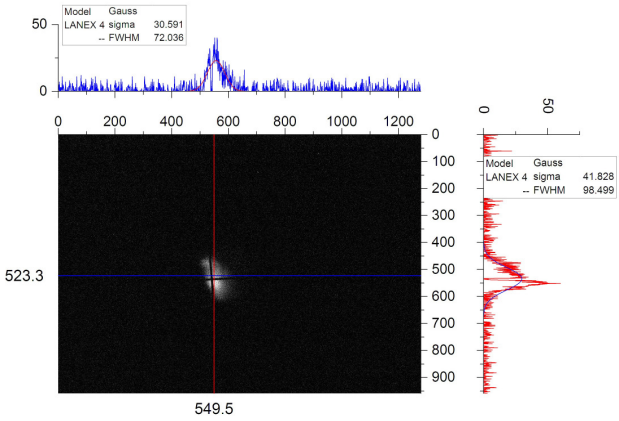

Figure 6.10: Electron beam imaged on L4, placed 5.1 m from the accelerator, after undulator.

The beam dimensions predicted by GPT simulations can now be compared to those measured. From section 4.5, the table of expected beam size has been summarised in table 6.1.

	Energy [MeV]	L1 [mm]	L3 [mm]	L4 [mm]
x dimension	80	1.2	1.45	1.3
y dimension	80	1.0	0.9	2.0

Table 6.1: Expected beam sizes on the different Lanex screens placed along the beam line as predicted by the GPT simulations.

Analysing the data recorded on the different Lanex screens (averaged over 50 consecutive shots), the measured beam radii are shown in table 6.2. The electron energy was measured in the low energy window of ES1 (also averaged over 50 consecutive shots).

	Energy [MeV]	L1 [mm]	L3 [mm]	L4 [mm]
x dimension	80 ± 5	1.4 ± 0.5	1.4 ± 0.5	1.5 ± 0.5
y dimension	80 ± 5	1.2 ± 0.4	1.1 ± 0.5	1.8 ± 0.6

Table 6.2: Measured average beam sizes on the different Lanex screens placed along the beam line.

The quoted uncertainties indicate the shot-to-shot pointing and energy fluctuations. Since the quadrupole optimisation is energy-dependent, it is seen that, with the correct electron energy (to within experimental uncertainty), there is good agreement in the predicted and measured beam sizes on both axes.

6.3.2 Results with the upgraded PMQ settings

These transport experiments refer to a different spacing between the quadrupoles, as discussed in section 4.4.5. A schematic layout including the spacing between the quadrupoles and the gas jet is shown in fig. 6.11. An image of the quadrupoles, mounted with the spacing, is shown in fig. 6.12.

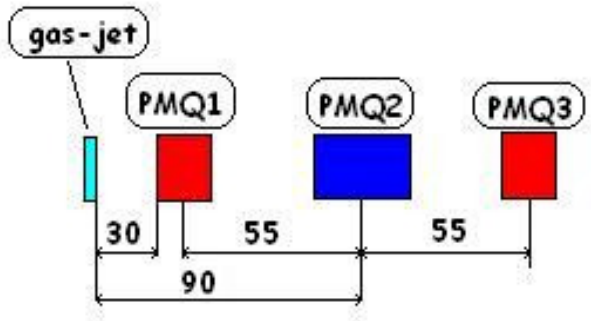

Figure 6.11: Updated spacing between the permanent magnet quadrupoles for collimation of a 130 MeV electron bunch. Dimensions are given in mm.

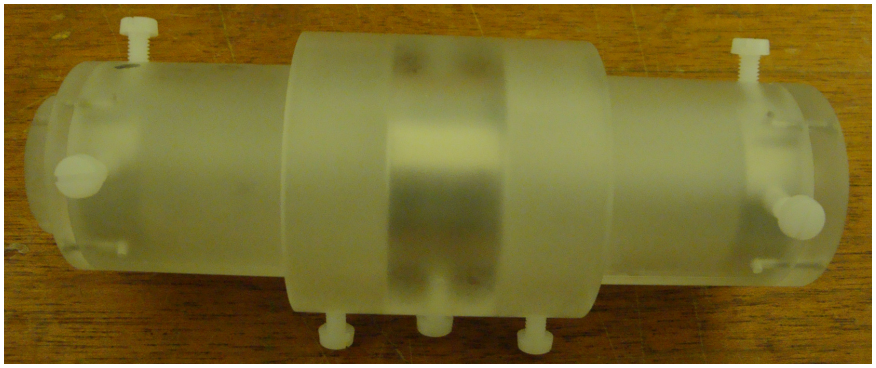

Figure 6.12: Photo of the mounted permanent magnet quadrupoles with updated spacing to produce a collimated beam at 130 MeV.

As discussed in section 4.4.5, this setting has been optimised for an electron energy of 130 MeV. The aim of this setting was to produce a collimated beam out of the permanent quadrupoles that would then be focused at the centre of the undulator with the electromagnet quadrupoles. As in the case shown in the previous section, the expected beam sizes (produced using the GPT code and summarised in table 6.3) will be compared to the measured beam sizes (table 6.4) to see if they are consistent.

Typical images as obtained on Lanex screens L1, L3 and L4 are shown in fig. 6.13.

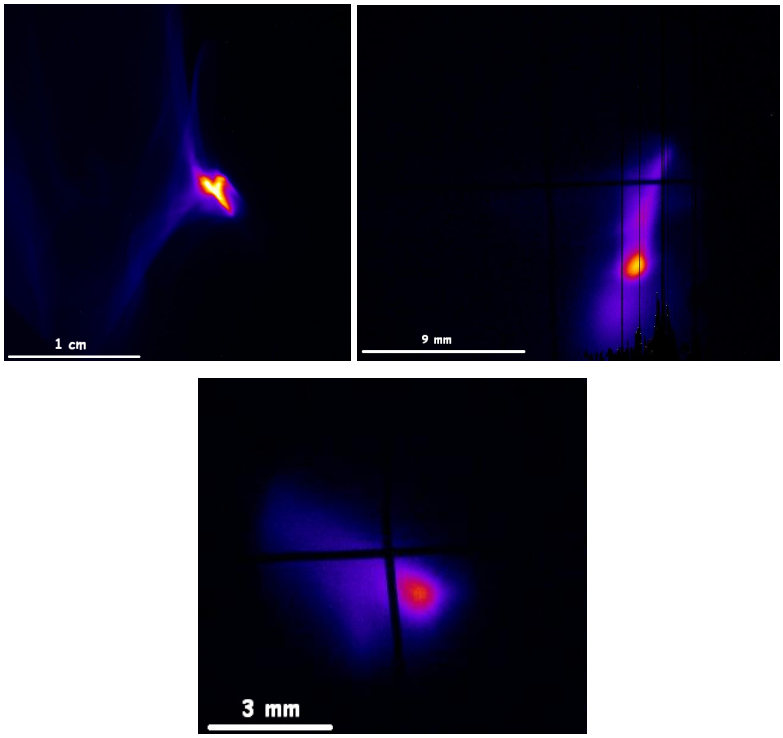

Figure 6.13: PMQs optimised using the spacing for a 130 MeV electron bunch (a) image on L1 of the electron beam exiting the accelerator and passed through the PMQs; (b) image on L3 of the electron beam collimated by the PMQs and focused at the centre of the undulator; (c) image on L4 of the electron beam collimated by the permanent magnet quadrupoles and focused at the centre of the undulator.

At L1, the electron bunch looks much more symmetric than in the case of quadrupoles attached each other (fig. 6.5) and the beam is also smaller. At L3 and L4, enhanced collimation resulting in a smaller beam size is also apparent.

Before discussing the expected beam size from GPT simulations, it is important to note that the new permanent magnet quadrupoles setting has been designed for 130 MeV, which was the mean energy observed during a previous experimental campaign. However, during the transport and FEL experiments (Chapter 7), it has not been possible to achieve this energy. In fact, during experiments, the mean electron beam energy was fluctuating greatly. The mean measured energy was 120 ± 40 MeV as shown in fig. 6.14.

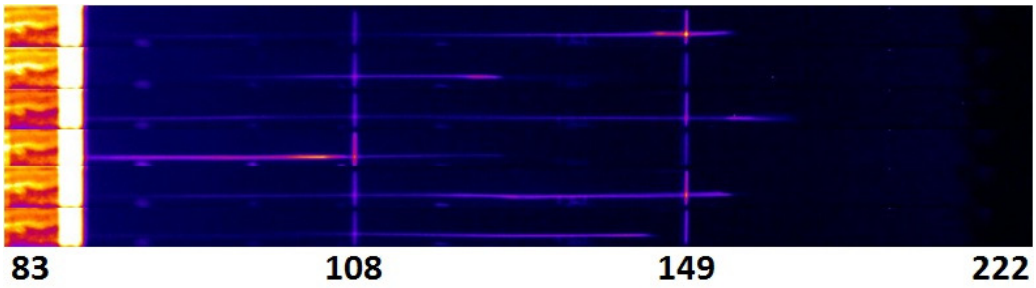

Figure 6.14: Example electron energy spectra as measured in the high energy window of ES1.

For this reason, GPT simulations have been performed with a variety of energies using the quadrupole settings used during the experiment and, in table 6.3, the expected beam size on the Lanex screens L1, L3 and L4 are reported. Simulations have been performed in order to fit the measurements.

Energy [MeV]	Lanex L1		Lanex L2		Lanex L3	
	σ_x [µm]	σ_y [µm]	σ_x [µm]	σ_y [µm]	σ_x [µm]	σ_y [µm]
90	220	1120	1460	1960	4010	7690
100	100	630	1200	180	1620	1210
110	170	270	770	600	890	590
120	310	110	280	360	380	100
130	420	200	250	140	180	150
140	510	350	720	730	660	330
150	590	480	1180	1310	1120	1350
160	660	580	1590	1860	1640	2340

Table 6.3: Expected beam sizes on the different Lanex screens placed along the beam line as a function of electron energy.

In order to compare the expected beam sizes with the measured ones, 50 consecutive shots on each Lanex screen have been analysed (table 6.4).

	Energy [MeV]	L1 [µm]	L3 [µm]	L4 [µm]
x dimension	120±40	404±530	657±690	501±205
y dimension	120±40	416±290	600±200	506±280

Tab. 6.4: Beam sizes obtained analysing 50 consecutive shots on each Lanex screen placed along the beam line during experiments, using the optimised quadrupole setting for 130 MeV.

As can be seen from table 6.3, the variation of the beam size for different energies is very large, and can range, on each Lanex screen, from a few mm to hundreds of µm, as shown in fig. 6.15.

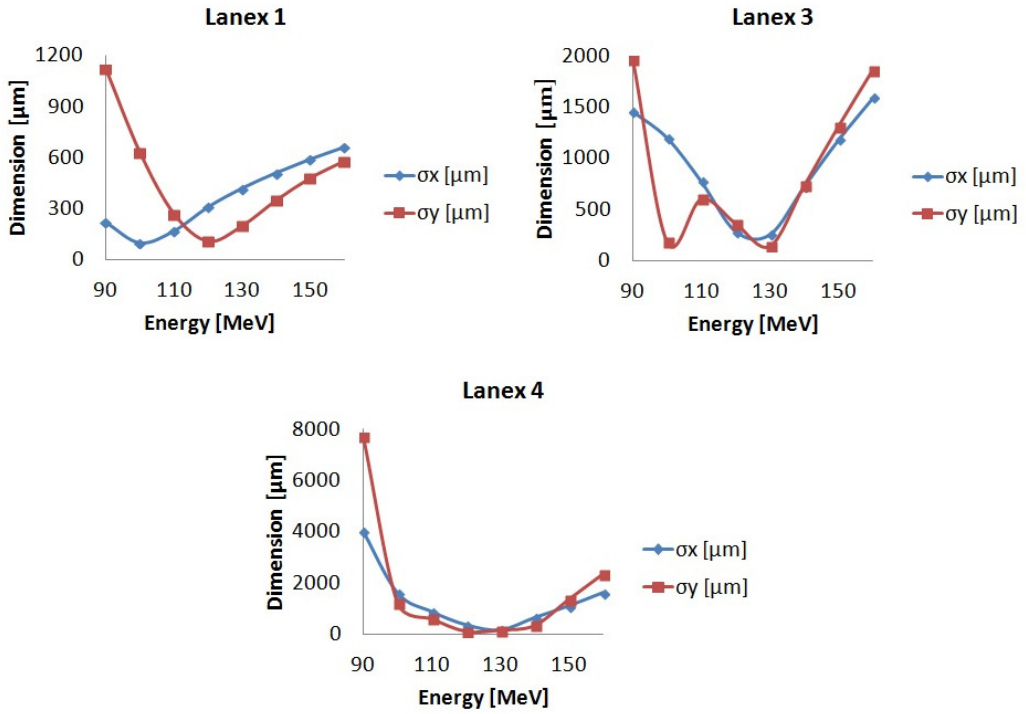

Figure 6.15: Expected beam sizes on the different Lanex screens placed along the beam line as a function of electron energy.

This behaviour has also been recorded on the experimental images (table 6.4) and, as a result, the rms large errors indicate some form of agreement between simulations and measurements. For this reason, in table 6.5, the smallest and the largest beam sizes measured on each Lanex screen are reported.

By comparing table 6.4 and 6.5, it is seen that the range of sizes on each Lanex is comparable with that predicted by GPT. However, because the beam size and the electron energy cannot be measured simultaneously (each Lanex is destructive to the beam), it is difficult to make an accurate comparison between simulations and measurements. It is possible to notice that there are big variations, mainly due to shot-to-shot fluctuations.

	Lanex L1		Lanex L2		Lanex L3	
	σ_x [μm]	σ_y [μm]	σ_x [μm]	σ_y [μm]	σ_x [μm]	σ_y [μm]
MIN	260 ± 50	230 ± 50	330 ± 50	300 ± 50	350 ± 50	300 ± 50
MAX	810 ± 50	800 ± 50	1700 ± 50	1300 ± 50	760 ± 50	860 ± 50

Tab. 6.5: Minimum and maximum beam sizes measured on each Lanex screen placed along the beam line during experiments, using the optimised quadrupole setting for 130 MeV.

6.4 Beam quality measurements

This section reports measurements of the electron beam quality performed on the beam line. As discussed in the previous chapters, in order to be able to generate FEL radiation, a very high quality electron beam is required and it has to be well transported inside the undulator. The parameters to take into account regarding the quality of the electron bunches are the transverse emittance, bunch length, charge and energy spread. The methodology of the measurement has already been given in Chapter 5 and, therefore, this section will mainly focus on the experimental results.

The first parameter that has been measured is the electron beam transverse emittance (section 5.3.2.4). To determine the normalised transverse emittance, ε_n, a pepper pot mask has been used, impinging the beamlets on a Ce:YAG crystal imaged by a CCD camera (fig. 6.16).

Using this method, the lowest ε_n of 1.2 π mm mrad has been measured with an average of 2.2 ± 0.7 π mm mrad in the horizontal axis and 2.3 ± 0.6 π mm mrad in

the vertical axis as shown in fig. 6.17. Moreover, since the observed beam divergence was 2-4 mrad, it has been possible to estimate the source size to be smaller than 3µm [22].

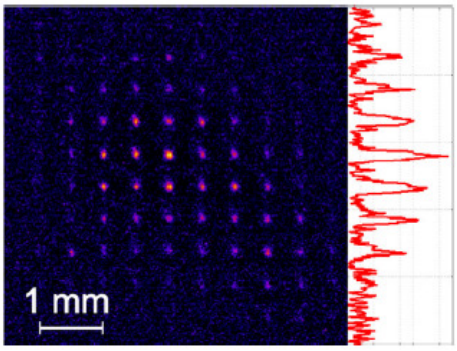

Figure 6.16: False colour, background corrected, pepper pot image produced on the Ce:YAG crystal by an electron beam after propagation through the emittance mask. A vertical lineout is shown on the right-hand side. From Ref. 22.

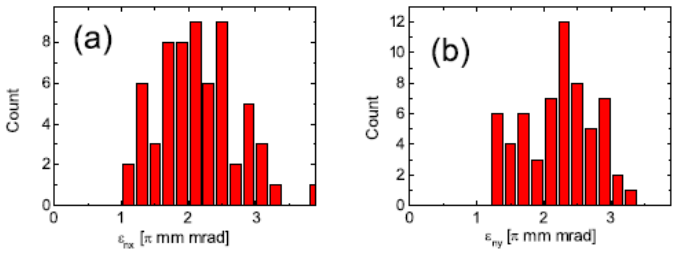

Figure 6.17: Distribution of the horizontal (a) and vertical (b) normalised emittance for a collection of 64 shots from Ref. 22.

The next parameter is the electron bunch duration, which has been measured using a transition radiation technique. Figure 6.18 shows the measurements performed (black dots with error bars), compared with simulations at different bunch durations: the simulation that best fits the measured data indicates a 2 fs duration [161]. The measurement has been performed 1 m from the accelerator, just after L1.

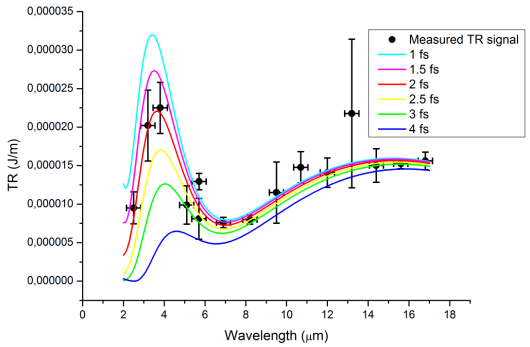

Figure 6.18: Measurement of transition radiation at different wavelength overlapped with different theoretical bunch duration curves.

The electron beam charge has been measured in many places along the beam line using Fuji BAS imaging plates (IPs) [162]. When located directly in front of a Lanex screen, simultaneous capture of the charge on the IP and the Lanex can be recorded. In this way, L2, L3 and L4 have been absolutely calibrated for charge. An example of the measurement is shown in fig. 6.19.

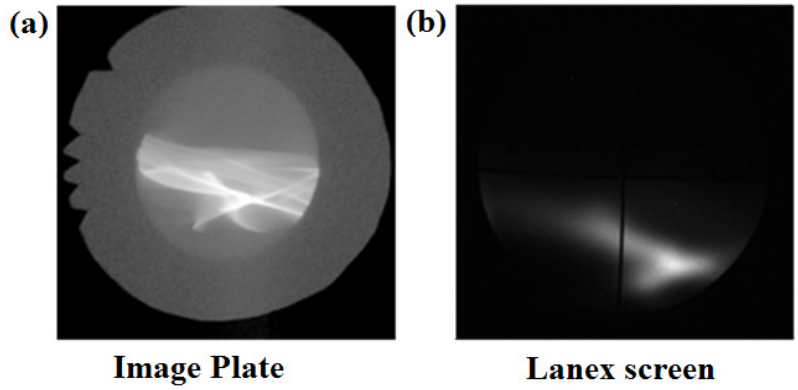

Figure 6.19: Example measurement of the charge using imaging plates; electron beam images on the (a) IP after the read-out and (b) L3.

After recording data on all the imaging plates, they have been read using a scanner (Fuji FLA 7000) and the data has been processed using eq. [5.1]. Using this method, a charge up to 20 pC has been measured on L2 while, on L3 and L4, the maximum charge measured has been 5 pC and 3.5 pC respectively. The loss in charge between

L2 and L3 and L4 is mainly due to low energy electrons (low energy halo) which are not useful for FEL anyway. Regarding the Ce:YAG screen of the electron spectrometer ES1 and the Lanex screen of the downstream spectrometer ES2, cross-calibration has been achieved on a statistical basis using the other Lanex screens simply by recording 100 shots on the calibrated Lanex followed by 100 shots on the non-calibrated Lanex/Ce:YAG and assuming equal amounts of charge in each case.

The last measurement that will be described is that of the energy spread. Figure 6.20a and 6.20b show two more typical electron spectra measured on ES1, while fig. 6.20c and 6.20d show two typical electron spectra measured on ES2.

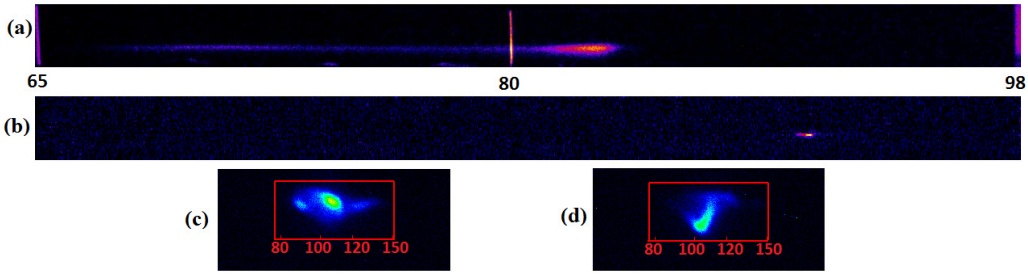

Figure 6.20: Electron spectrometers spectra measured on (a) ES1 high resolution window, (b) ES1 low resolution window, (c-d) ES2.

As can be seen in fig. 6.20a, using ES1, it is possible to measure part of the halo of the beam, but in ES2 the halo is completely dispersed (fig. 6.20c and d) and only the main central beam is observed. Also, fig. 6.20b shows the lowest energy spread thus far measured on the ALPHA-X beam line, which corresponds to 0.4% rms of the main bunch.

6.5 Beam transport through the undulator

In this section, the main results for the transport through the undulator will be shown. The main aim is to confirm that the electron beam dimensions at the undulator entrance and exit agree with the simulations and that, therefore, it can

be assumed that the beta function approximates to that calculated using the GPT code. The major parameter that is changed between simulations and measurement is the electron energy: in fact, as will be seen in Chapter 7 as well, the average electron energy that was generated during experiment was centred at 95 MeV while the simulations were carried out to optimise an electron energy of 130 MeV.

At L3, the mean r.m.s. width (over 50 consecutive shots) is 460×410 μm with the smallest width of 240 μm $\times$ 290 μm close to the modelled values of 255 μm $\times$ 259 μm. At L4, however, both the mean (640 μm $\times$ 680 μm) and smallest (360 μm $\times$ 400 μm) r.m.s. widths are significantly larger than the modelled values of 247 μm $\times$ 267 μm, which means that symmetry is not obtained. This is mainly due to the lower electron energy compared to the optimal energy. However, from the numbers given above, it is possible to predict a beam waist of 35 μm $\times$ 44 μm with a beta function of about 70 cm which is very short compare to the undulator length.

The reason of this behaviour is that the electromagnets are very close to the undulator and, therefore, to make sure that the focal point position is in the centre of the undulator, the beam must be strongly focused and this, of course, influences the beta function. There are two ways to get a longer beta function: one would be to separate further the electromagnetic quadrupoles from the undulator and the second could be to use only two of the electromagnet quadrupoles of the triplet but this could present problems at the waist by creating an asymmetric beam.

6.6 Transport issues

In this section, two main difficulties related to the transport will be discussed. One is related to the misalignment of the undulator and the second one is the effect of the laser beam blocker on the electron bunches. Both of them, in different ways, are of paramount importance. The undulator misalignment can cause various difficulties; the most evident one is a displacement of the electron beam with respect to the centre of the transport line.

The second important issue that will be discussed is the emittance growth due to the thin aluminium foil (thickness 50 µm) used to prevent the laser beam and UV plasma radiation from entering the radiation spectrometer. The effect of the laser beam filters cannot be simulated using the GPT code, hence, GEANT4 has been used to simulate this effect and it is found that, due to the multiple scattering inside the filter material, the electron bunch after the foil has an emittance that can be up to 3 times larger than that with no foil in place.

6.6.1 Undulator misalignment

The initial alignment of the entire ALPHA-X beam line has been carried out in collaboration with STFC ASTeC, Daresbury Laboratory. During this process, a laser tracker alignment system has been used to align the major beam line components to within 50 µm precision. Usually the alignment of a beam line, for a lab built on a stable ground, can last for a very long time.

For the ALPHA-X beam line, the equipment that is more sensitive to misalignments are the magnetic ones, which are the quadrupoles, the electron spectrometer and the undulator. All of them, if misaligned, can mainly give a kick to the electron beam and change its trajectory. In particular, if the undulator is misaligned, the kick that the electron beam experiences can cause the electrons to perform betatron oscillations during the propagation, and these oscillations can be as large as the misplacement between the geometrical centre of the entrance and the geometrical centre of the exit of the undulator itself. Also, as already stated in Chapter 3, large mismatch due to betatron oscillations, will degrade the FEL performance; in fact, because of the mismatch, in the wiggle plane the envelope will evolve ballistically (neglecting the space-charge effect) and have a lower average density through the undulator, destroying the FEL action.

At the beginning of the experiments presented in this thesis, the initial goal was to transport the electron bunches produced by LWFA to the end of the beam line without using the undulator in order to demonstrate that the permanent magnet quadrupoles were effectively able not only to reduce the pointing instabilities but

also to efficiently transport the electron bunches over such a long length. To do so, the undulator field has been removed by winding out the undulator magnets using its winding mechanism (it has been designed as a tuneable gap undulator) and a 3 cm diameter vacuum pipe placed on-axis. Once the electron beams have been imaged on the L4 Lanex screen, the 3 cm diameter pipe has been replaced with the normal 6 mm diameter pipe that sits between the undulator magnets and the undulator magnets has been wound back again. Unfortunately, this operation has caused a misalignment of the undulator.

During the experiments it was noticed that the electron beams were always exiting from the top right corner of the undulator, as shown in fig. 6.21. The same behaviour also been observed in the undulator radiation detected using a camera with an objective focusing at the centre of the undulator, as shown in fig. 6.22.

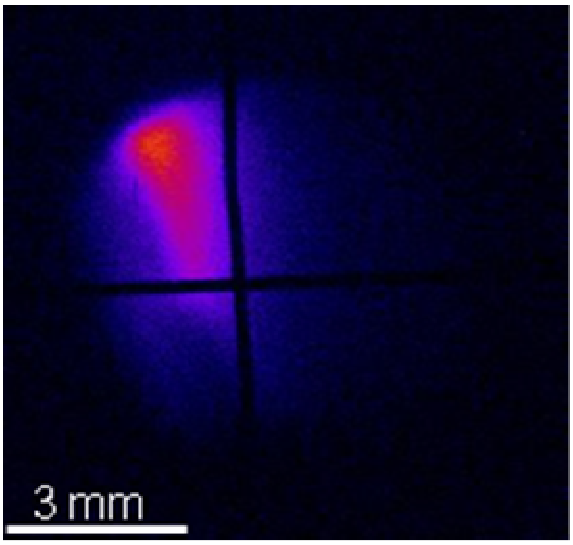

Figure 6.21 : Electron beam imaged at the exit of the undulator before alignment. The image has been taken with a camera looking at a mirror placed at 45° from the electron axis so the right corner is the real left corner and vice versa.

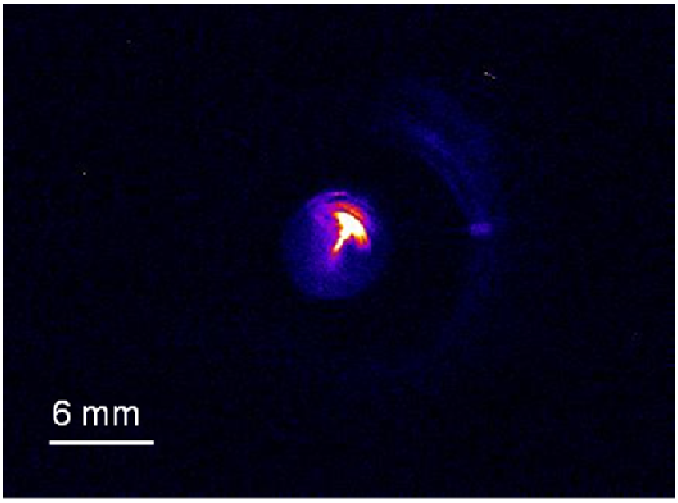

Figure 6.22: Undulator radiation imaged at the exit of the undulator using a camera with an objective focusing at the centre of the undulator.

6.6.2 Effect of the laser beam filters

The use of laser beam filters during experiments is very important because scattered laser light can readily saturate the radiation detector making measurements of the undulator spectra very difficult. During the transport experiments, however, it was quickly noticed that the filter were affecting the beam size downstream and so a study has been carried out with 2 different locations of the filter with respect to Lanex screen L3, as shown in fig. 6. 23.

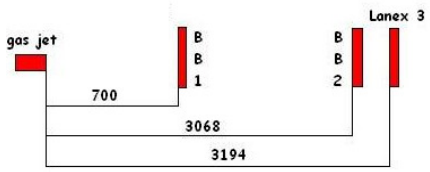

Figure 6.23: Schematic of the beam block positions (BB1 and BB2 respectively) along the beam line.

In this way, the beam size using beam blocks close to and far away from the Lanex has been measured. The obtained images on L3 for the 2 beam block positions, are shown in fig. 6.24.

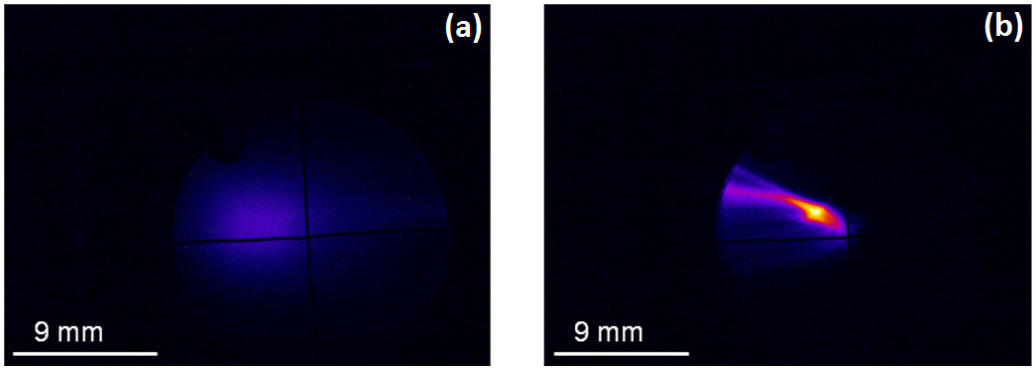

Figure 6.24: Image of the electron beam on L3 using (a) BB1 and (b) BB2.

Both BB1 and BB2 consisted of one normal aluminium foil ("kitchen foil") of thickness 50 µm. As is evident, the beam size changes dramatically. In both cases, the permanent magnet quadrupoles have been used and the transport conditions were exactly the same, which means that the observed effect is only due to the respective beam block. Analysis shows that by using the first beam block BB1, the beam size recorded on L3 is:

$$\sigma_x = 2.03 \pm 0.01 mm$$
$$\sigma_y = 1.53 \pm 0.01 mm$$

while using the second beam block BB2, the beam size is:

$$\sigma_x = 0.6 \pm 0.01 mm$$
$$\sigma_y = 0.62 \pm 0.01 mm$$

Hence, there is a dramatic factor of ~3 increase in beam size on L3 for a beam block located far in front of the screen as compared to one located very close to the screen.

Following this experiment, GEANT4 particle scattering simulations have been performed. By simulating the experimental conditions described here, it is found that the emittance of the electron bunch grows dramatically with the foil thickness and the distance of the beam blocker from the source (which is the electron beam focal spot), as shown in fig. 5.14.

Because of this issue, it has been necessary to use a very thin beam blocker at the entrance of the undulator. Different blockers have been tested and eventually it

was found that the best solution was an 800 nm thick aluminium foil, which effect on the emittance is estimated to be a factor 2.

6.7 Discussion

In this chapter, details have been described of the transport experiments that have been performed on the ALPHA-X beam line. In particular, in the first part of this chapter, the initial ALPHA-X beam line has been presented: after the accelerator, there were a triplet of electromagnet quadrupoles, a high resolution electron spectrometer followed by the undulator. The electron bunches exiting the accelerator have been shown with a divergence of 2 mrad. The optimised transport using this beam line has been shown, highlighting the need of a triplet of permanent magnet quadrupoles because of the loss of bunch charge during the transport. For this purpose, a triplet of high gradient permanent magnet quadrupoles has been designed.

Two different set of experiments have then been described, one using the permanent magnet quadrupoles (PMQs) only to reduce the divergence of the bunch and one to optimise the transport for a certain range of electron energy (which is centred on 130 MeV). These two set-ups differ from each other in two aspects: one is the position of the triplet with respect to the gas jet and the other is the position of each quadrupole with respect to the others (magnet separation). The first set-up has sandwiched the PMQs directly one after another (zero separation) and placing them 13 cm from the gas jet. Whereas the second set-up, used to collimate a 130 MeV electron bunch exiting the accelerator, had the quadrupoles separated with the first quadrupole placed just 3 cm from the gas jet. Simulations predicted that this latter set-up would minimise electron bunch lengthening. A reduction of divergence by more than 50% with the PMQs has been shown. It has been possible to transport the whole bunch up to the end of the beam line with a charge transmission along the undulator of up to 80%.

Measurements of the electron bunch quality (emittance, bunch duration, charge and energy spread) have been presented. Using the pepper-pot mask technique, an upper limit (due to the detector resolution) of 1.1 π mm mrad has been made for the normalised transverse emittance. The bunch duration at 1 m from the accelerator has been estimated with transition radiation, giving an rms duration of 2 fs (using the first set-up for the PMQs). This is in good agreement with GPT simulations and using the second set-up for the PMQs could result in an even shorter bunch duration.

Charge has been measured in absolute terms with imaging plates and imaging screens have been cross-calibrated against that data. A high resolution electron spectrometer has been used to characterise the electron energy spectrum. An rms energy spread as low as 0.4% has been measured for the main quasi-monoenergetic electron bunch.

Individually, these are parameters for an LWFA-driven FEL. The challenge is to achieve all the FEL criteria simultaneously in a well transported electron bunch. In the last section of the chapter, transport along the beam line has been investigated and the size of the electron beam predicted by GPT has been compared with the measurements. Good agreement between simulations and measurements allow a reasonable estimation to be made of the beta function inside the undulator.

Some transport issues encountered during experiments have been analysed: in particular, two obstacles have interfered with experiments; one is the undulator misalignment, which has been easily solved by re-aligning the whole beam line using a laser tracker, and the other one related to the effect of the laser beam filters.

A major issue still to be resolved is the effect of the laser beam filters. Transport experiments are unaffected in terms of characterising the beam charge and size at different places along the beam line but, in the undulator experiments, the use of laser beam blocks can be seen as a significant problem. GEANT4 simulations predict an emittance growth by a factor of 3 after a 50 μm thickness aluminium filter due to multiple scattering. This simulation has been experimentally confirmed, using beam

blocks placed in different positions along the beam line and imaging the electron beam profile on the relevant Lanex screen. In particular, using beam blocks placed roughly 2.5 m apart and using a Lanex screen L3 placed after the second beam block, a factor of 3 in the beam size has been measured.

For this reason, it is necessary to use as the laser blocker a very thin aluminium foil (800 nm thickness) placed just at the entrance of the undulator. This is the minimum practical thickness for total attenuation of the laser beam, however, it is still detrimental to the beam quality (emittance growth, in fact, is estimated to grow by a factor 2). The emittance of the beam is one of the most important parameters to preserve and it is impossible, after it has increased for whatever reason, to reduce it once again.

Chapter 7

Undulator radiation:

experimental results

7.1 Introduction

In this chapter, a demonstration of emission of LWFA-driven undulator radiation in the deep UV to VUV spectral range will be given. The short wavelength of this radiation source has the potential to serve a very large user community; especially for ultrafast studies since the LWFA has the ability to produce very short duration electron bunches which, if properly transported, can give rise to very short (sub-10 fs) radiation pulses.

In the next sections, all the experiments carried out using the ALPHA-X undulator will be described. Note that, even if the undulator gap is tuneable, all the experiments described in this chapter uses a fixed gap between the undulator poles of 8 mm. In particular, three different types of measurement will be described. The first one was achieved by placing a CCD camera and imaging lens after the exit of the undulator to image the centre of the undulator. The second method replaced the camera with an optical spectrometer and a silicon detector for measurements in the deep UV spectral region. Finally, measurements in the VUV range have been performed with a scanning monochromator and ICCD camera.

The last section of the chapter will investigate beam quality dependence based on the electron beam central energy, energy spread and length, and scaling of the output radiation. Conclusions are then made about the experiment with an analysis of the different problems experienced.

7.2 Undulator radiation imaging

The experiments described here have been performed in the initial stage of transporting the electron beam along the undulator, mainly as a proof-of-principle for the electron beam transport and also to check that some radiation was effectively emitted from the undulator. As already discussed in section 6.6, during this test the undulator was misaligned, however, this experiment has nevertheless been a useful exercise to learn how to successfully transport the beam along the

undulator, using not only the permanent magnet quadrupoles but also the electromagnet quadrupoles. Another achievement during this test has been to verify that the simulations carried with the GPT code for the transport of the electron bunches were trustable and in good agreement with observations. The electron mean energy measured during this experimental campaign is 80 MeV.

In particular, the first radiation from the undulator was measured using three different set-ups: the first one using a CCD camera (PGR Flea2) with an objective lens that was focusing at the centre of the undulator, the second one using the same CCD camera, but replacing the camera's objective with a collimating plus focusing lenses and the last one using the same lenses and replacing the CCD camera with an Oriel spectrometer coupled to a 250 x 2000 pixel Hamamatsu CCD camera.

All the different set-ups have in common some parts which are (i) a Lanex screen (L4) that can be placed in or out of the beam line and used to monitor the pointing and profile of the electron bunches exiting the undulator, (ii) a deflector which bends the electrons out of the radiation trajectory and (iii) the beam block used to block the laser and plasma light. The deflector, in this particular experiment, was used only to bend the electrons out of the beam-line (beam dump) but not as an electron spectrometer.

Two different imaging setups have been used, both using an optical window at the end of the vacuum beam line after the deflector. The first one uses the set-up shown in fig. 7.1. The CCD camera objective is set with an image focal length of 1.5 m, corresponding to the centre of the undulator.

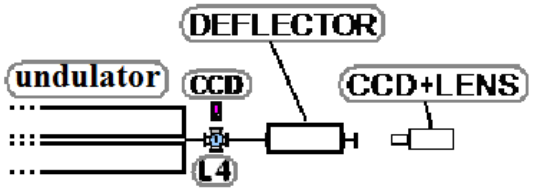

Figure 7.1: First imaging set-up: CCD camera with objective lens to image the centre of the undulator.

Using this set-up, the first undulator radiation was observed, as shown in fig. 7.2. From this image, it is evident that the radiation is located in the top right corner of the pipe and is the first proof of misalignment of the undulator.

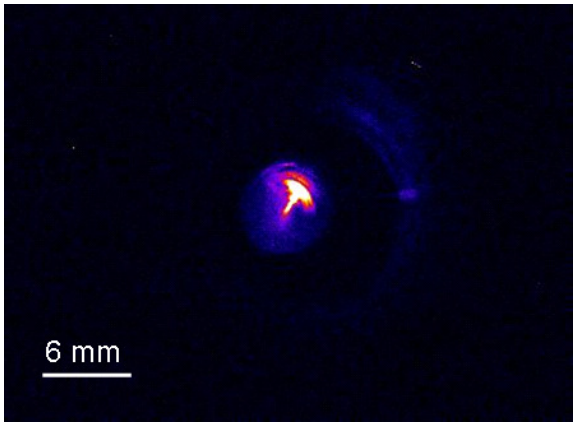

Figure 7.2: Undulator radiation imaged using a CCD camera coupled to an objective lens.

However, even if the radiation is not located at the centre of the pipe and the undulator is misaligned, some important information can be extrapolated from the images recorded. In fact, averaging over 50 shots, the size of the radiation image in both planes can be determined, as shown in table 7.1.

	σ_x [mm]	σ_y [mm]
average	1.43	1.32
error	0.15	0.22

Table 7.1: Radiation beam sizes and errors measured using a CCD camera with objective lens.

The error in the measured y dimension is larger: this is due to the fact that the undulator was misaligned more in the y direction than in the x direction, resulting in a bigger cut of the radiation on this axis with respect to the other one.

From these sizes, it is possible to calculate the divergence of the radiation. For a flat undulator, with *N* periods, the radiation cone has an aperture that scales as:

$$\vartheta_{cone} = 1/\gamma \cdot \sqrt{N} \qquad [7.1]$$

So, considering that the Lorentz factor γ is 200 for this experiment and that the undulator has 100 periods, the expected beam cone aperture after the 1.5 m undulator is 0.5 mrad. In the case shown in Table 7.1, the measured beam sizes are of the order of 1 mrad, which is quite close to the expected value.

After the experiment described above, the imaging diagnostic has then been updated by replacing the objective lens with a collimation system (1.5 m collimating lens followed by a 10 cm focusing lens), as shown in fig. 7.3. This upgrade has been conceived to find the position of the radiation focal position so to then step forward by replacing the camera with a spectrometer to resolve the spectra. The experiment has been carried out when the undulator was still misaligned.

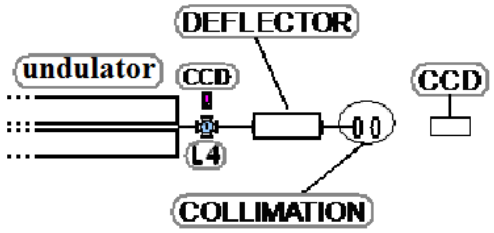

Figure 7.3: Second set-up – 1.5m collimating lens followed by a 10cm focusing lens and a CCD camera to detect the undulator radiation.

The radiation observed in this case is shown in fig. 7.4 and the size of the radiation beam is calculated to be 180 µm.

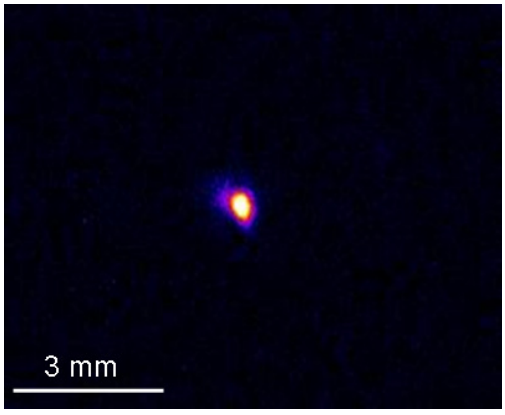

Figure 7.4: Undulator radiation imaged using a CCD camera coupled with a 1.5 m collimating lens and a 10 cm focusing lens.

This observation confirms the measurement performed before. In fact, considering that the lenses used have 1.5 m and 10 cm focal lengths, respectively, and they are placed 10 cm apart, the equivalent focal length of this system turns out to be about 10 cm and the demagnification is M = –0.067. Therefore, the real size of the radiation beam at 1.5 m from the equivalent lens, considering that the measured radiation size is 180 µm, is 2.7 mm.

7.3 Deep UV undulator radiation measurements

The first spectral measurements have been carried out by replacing the CCD camera with an Oriel spectrometer coupled to a 250 x 2000 pixel Hamamatsu CCD camera. The collimating lenses remain the same as the previous imaging setup as shown in fig. 7.5. The deflector is now the upgraded system that also acts as a simple electron spectrometer (section 4.4.3.2). The permanent magnet quadrupoles are attached to each other and the centre of the triplet is placed 15 cm from the accelerator for this experiment.

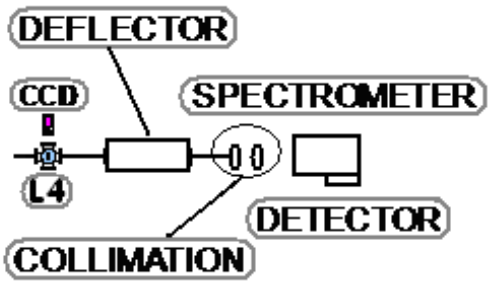

Figure 7.5: Deep UV radiation set-up – a 1.5m collimating lens followed by a 10cm focusing lens coupled with an Oriel spectrometer and Hamamatsu detector.

Two example detected spectra are shown in fig. 7.6. The images show two undulator spectra measured at two different wavelengths, corresponding to two slightly different electron energies. In particular, fig. 7.6a shows the radiation spectrum and the corresponding electron energy spectrum; the radiation peak wavelength in this case is 320 nm. Figure 7.6b, instead, shows a lower wavelength

radiation spectrum and its corresponding electron energy spectrum; the radiation peak wavelength in this case is 275 nm, which is the lowest wavelength that has been detected using the Oriel spectrometer system.

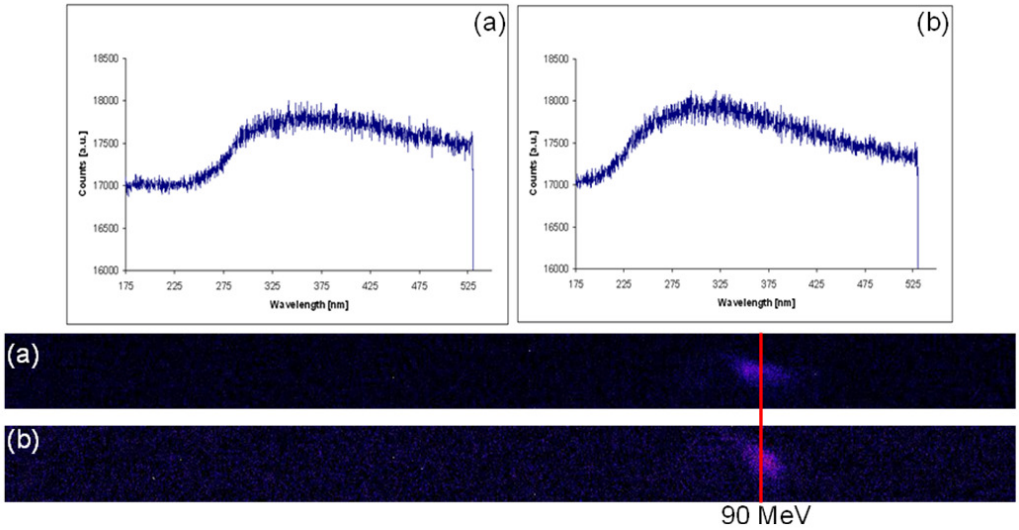

Figure 7.6: Two undulator radiation spectra and corresponding electron spectra; undulator radiation measured with Oriel spectrometer and Hamamatsu detector.

The measured spectra have been eventually corrected using the transmission curves of the Oriel spectrometer grating. An example of the corrected spectrum is shown in fig. 7.7.

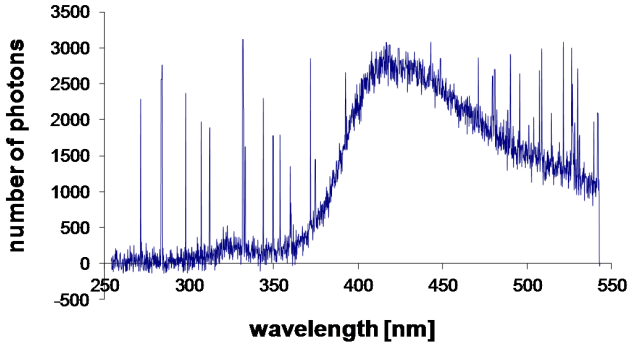

Figure 7.7: Corrected radiation spectrum using transmission functions for the grating and the Hamamatsu camera.

By analysing the spectra, considering the quantum efficiency of the Hamamatsu camera (7 photons per count), the total number of measured photons in this case is $0.5 \times 10^6 \pm 6 \times 10^3$.

7.4 VUV undulator radiation measurements

The more accurate measurement and analysis of the collected data has been conducted during this experiment. The entire layout of the experimental set-up is shown in fig. 7.8. The most important change for this experiment are alignment of the undulator and changing the spacing of the permanent magnet quadrupoles in order to collimate the beam exiting the accelerator. The distance between the quadrupoles is the one described in sections 4.4.5 and 6.3.2. Moreover, the laser and plasma light have been blocked at the entrance of the undulator with a sub-μm thickness aluminium foil (800 nm).

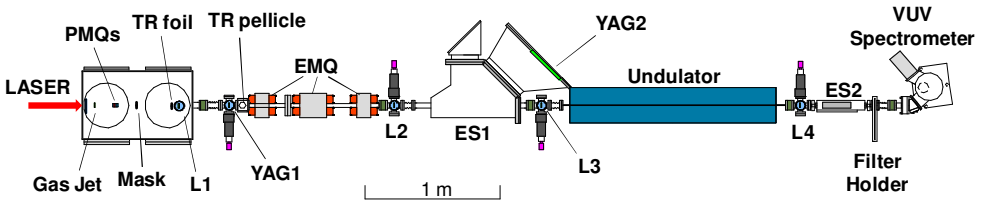

Figure 7.8: Latest experimental set-up which includes the detection system consisting of a McPherson spectrometer coupled to an Andor Newton CCD camera.

The new spectrometer used for this set of measurements is a McPherson vacuum scanning monochromator (with platinum-coated toroidal mirror and 300 l/mm grating) coupled to a 16-bit Andor Newton ICCD camera. Pictures of both the detector and the camera are shown in fig. 7.9.

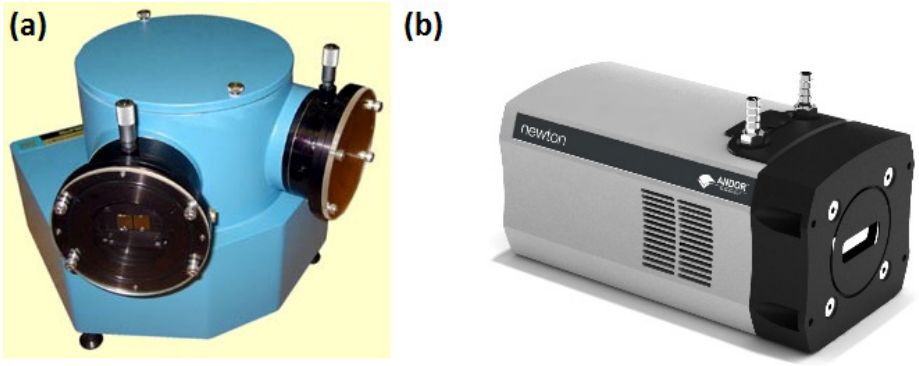

Figure 7.9: Images of the (a) McPherson spectrometer and (b) the Andor Newton CCD camera.

Three elements attenuate the radiation signal: the toroidal mirror (peak reflectivity of 65%), the grating (peak efficiency of 25% at 150 nm) and, finally, the quantum efficiency of the Andor camera (25% across the relevant spectral range).

For this experiment, the undulator was aligned with a precision of the order of 50 μm. Therefore the transmission along the undulator was very high; a statistical study of the charge on the Lanex screen placed before the undulator (L3) and the Lanex screen placed after the undulator (L4) shows that in fact the transmission has been improved from 30% to 80%. This is an important achievement because in this case it has been possible to measure the radiation spectrum produced by electron bunches with a charge up to 3pC. Some typical spectra measured using this detection system are shown in fig. 7.10.

The peak wavelength that has been measured in this set of measurements ranges from 265 nm down to 199 nm, corresponding to a peak energy for the electrons from 83 MeV up to 131 MeV. The quality of this radiation will be described in more details in the next section.

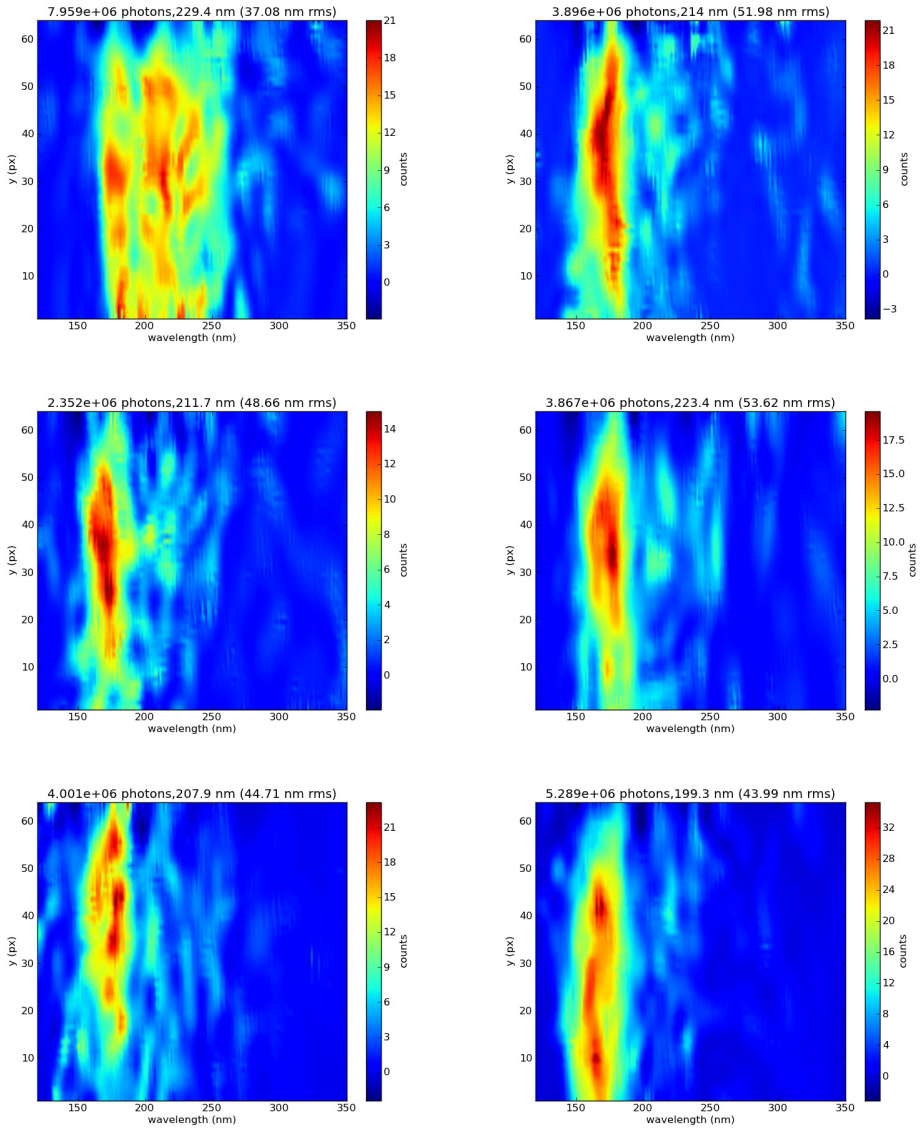

Figure 7.10: Undulator radiation measured using a McPherson spectrometer coupled to an Andor Newton CCD camera. Vertical axis corresponds to vertical axis of the monochromator entrance slit.

7.4.1 Beam quality dependence

In chapter 3, all the limitations for the FEL operation have been given. Here a summary of these limitations will be given as well as a comparison between the limits and the achievements will be presented.

The first FEL limitations are on the bunch duration, the peak current and the emittance at the undulator entrance.

The simulation result shown in fig. 7.11 has been conducted using the quadrupole settings used for this experiment, which was the optimal combination to efficiently transport a 130 MeV electron bunch through the undulator, designed to have a collimated beam exiting the triplet of permanent magnet quadrupoles and a short bunch duration (as short as 3 fs for a 0.3 fs duration at the plasma exit).

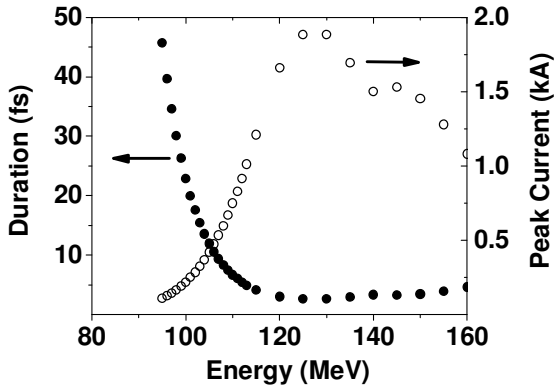

Figure 7.11: Simulations showing the dependence on the electron energy of the electron rms bunch duration and the peak current at the undulator entrance. Simulation initial bunch parameters: 5% r.m.s. energy spread, 5 pC charge, 1.75 mrad half-angle divergence, 1 μm r.m.s. radius, 0.9 fs r.m.s. duration.

The simulation shows that, at a desired electron energy of 130 MeV, a duration of 3 fs could be achieved at the undulator entrance, corresponding to a peak current close to 2 kA. However, as already discussed in Chapter 6, during the experimental campaign, it was not possible to produce stable beams with 130 MeV energy and, in fact, the energy was fluctuating in the wide range of energies from 85 to 160 MeV. A statistical analysis of the data collected on the Lanex screens placed before and after the undulator (L3 and L4 respectively) have shown that only 25% of all the shots have satisfied the optimal conditions predicted from the GPT simulations. Recorded shots demonstrate that statistically the mean energy achieved during the experiment was 100 MeV; because the mean energy was so different from the optimum 130 MeV electron energy, the transport was not optimised, causing a loss in peak brightness and in peak current. In fact, fig. 7.11 shows that, using the

quadrupole settings optimised for an energy of 130 MeV, at 100 MeV the bunch duration is of the order of 25 fs and therefore the peak energy decreased from 1.9 kA to only 0.35 kA.

The other beam quality parameter that has been measured is the energy spread. To ensure FEL operation, as shown in Chapter 3, it is of paramount importance to have very low energy spread. Energy spread, in fact, is strictly related to the FEL parameter ρ, defined as:

$$\rho \propto \left(\frac{I_{beam}}{I_A} \left(\frac{\lambda_u a_u}{2\pi\sigma_r} \right)^2 \left(\frac{1}{2\gamma} \right)^3 \right)^{1/3} \qquad [7.2]$$

which, in the case of the experiment (with a peak current of 0.35 kA, an energy of 100 MeV), is 1.15 x 10^{-3}. To have FEL gain, the energy spread has to be smaller than the FEL parameter which was not the case here. In fact, a statistical analysis of the data has shown that the average energy spread measured during the experimental campaign was of the order of 15%. This is a very important issue because from theory it can be estimated that with such a high energy spread, the saturation length grows from 3 m with the matched transport to a few kilometres!

The last parameter that influences the FEL operation is the emittance. In sections 5.4.3 and 6.6.2, the issue of using laser beam blockers on the beam line was discussed; to block the laser light and the UV plasma emission light is fundamental because otherwise the noise signal covers the radiation signal on the detector. On the other hand, multiple scattering in the beam block induces a growth in emittance. However, it has also been observed that the thinner the beam block, the smaller is the emittance growth. For this reason it was decided to use a sub-μm thickness aluminium foil (800 nm) placed at the entrance of the undulator and Monte Carlo simulations have determined that the foil induced emittance growth is negligible for such a thickness, as shown in section 5.4.3.

7.4.2 Output radiation scaling

The results achieved from the analysis of the experimental data presented in the previous two sections will be discussed. As stated before, the ALPHA-X beam line has been updated to be able to measure simultaneously the radiation emitted by the undulator and the electron bunch energy bent away using the low resolution spectrometer. Therefore, it is now possible to correlate different parameters to each other.

The first relation is that between the peak radiation wavelength and the central electron energy of the main peak given by:

$$\lambda_r \simeq \frac{\lambda_u}{2\gamma^2}\left(1+a_u^2\right) \qquad [7.3]$$

where λ_u is the undulator period, γ is the Lorentz factor and a_u is the undulator parameter (which is 0.38 for the ALPHA-X undulator). The plot in fig. 7.12 shows a reasonable agreement between the measured data and that expected from the above equation, showing that the calibration of the low resolution electron spectrometer (which is placed at the end of the beam line) made using the GPT code is very good and trustable.

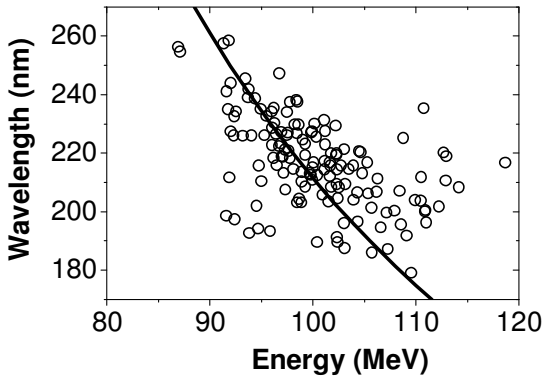

Figure 7.12: Electron central energy versus radiation peak wavelength. Experimental data is black circles and theoretical prediction is the black curve.

There is some discrepancy for higher electron energies (above 110 MeV) which may be due to the fact that large wavelength spread spectra have their centroid at longer wavelength from the peak; an example of this effect is shown in fig. 7.13.

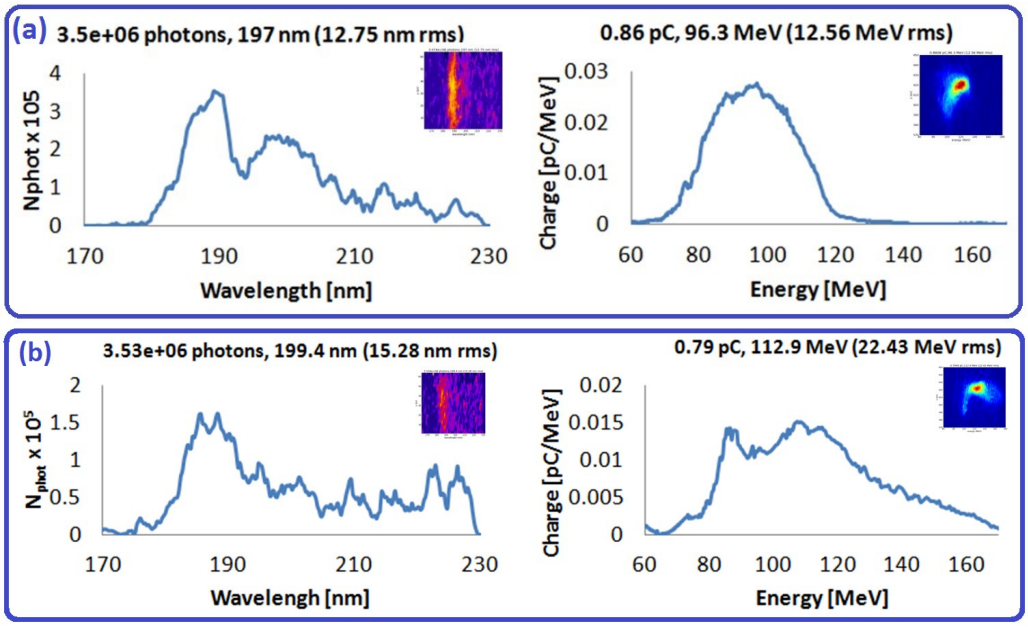

Figure 7.13: Radiation spectrum versus electron spectrum at (a) 96.3 MeV and (b) 113 MeV.

The next relationship is that between the spread of the radiation wavelength and the electron energy. The mean measured spectral bandwidth of the radiation is (69 ± 11) nm or (32 ± 7)%, decreasing as low as 16%. Images displayed in fig. 7.14 show the detected radiation spectrum (on the left hand side) and the corresponding electron beam spectrum (on the right hand side) which were recorded simultaneously.

Parameters for the radiation are the number of photons detected, mean wavelength and the wavelength spread. Equivalently for the electron beam, there is the charge, the mean energy and energy spread.

The radiation wavelength spread and the electron energy spread are related to each other by the formula:

$$\left(\frac{\delta\lambda_r}{\lambda_r}\right)^2 = \frac{1}{N_u} + \left(\vartheta^2\gamma^2\right) + \left(2\frac{\sigma_\gamma}{\gamma}\right)^2 \qquad [7.4]$$

where σ_γ/γ is the electron energy spread, $1/N_u$ is the natural bandwidth and ϑ is the divergence. The relation between the optical and electron spreads should be linear with a slope of 2 if the other terms are negligible. Applying an electron beam divergence of 0.8 mrad from the L4 data (details are reported in section 6.5), the dominant contribution to the spectral bandwidth is seen to be the electron energy spread, which was of the order of 15% (measured on the low resolution electron spectrometer placed at the end of the beam line).

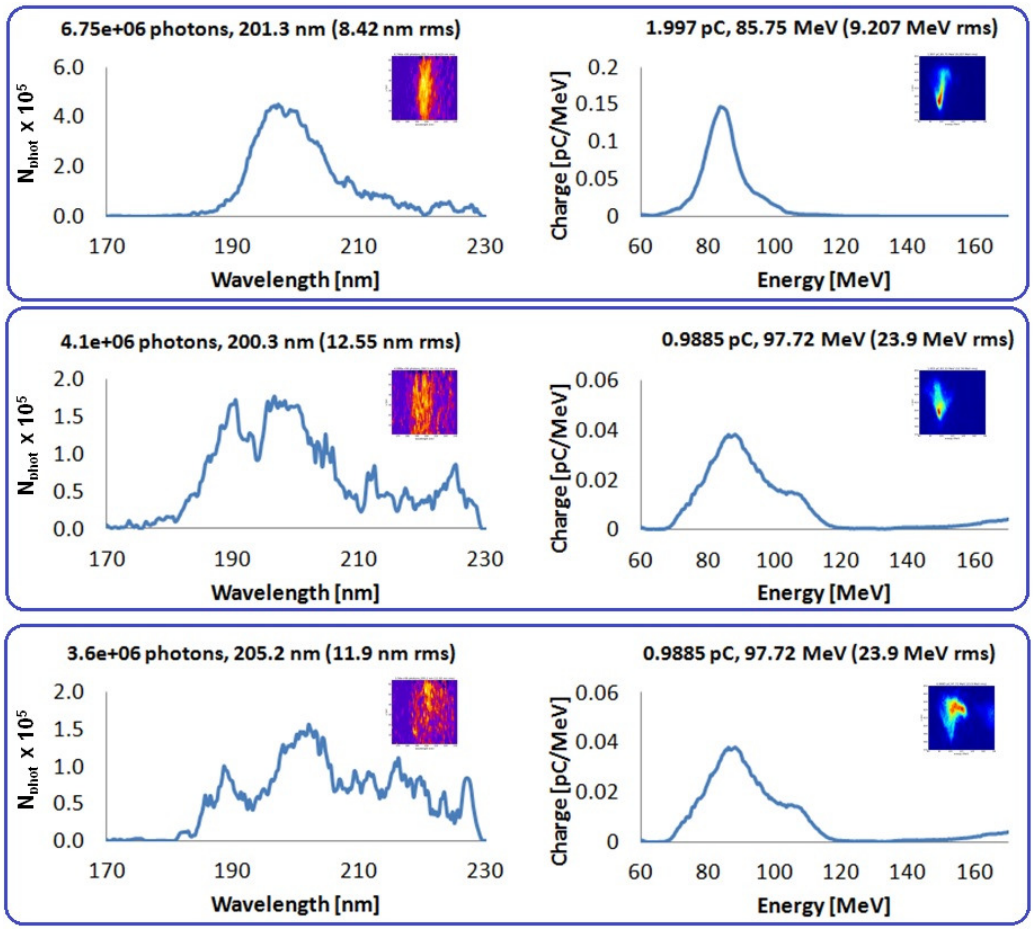

Figure 7.14: Detected undulator radiation spectra and corresponding electron energy spectra; the quality of each signal is reported on the top of each image.

Figure 7.15 shows the relation between the optical and the electron energy spreads.

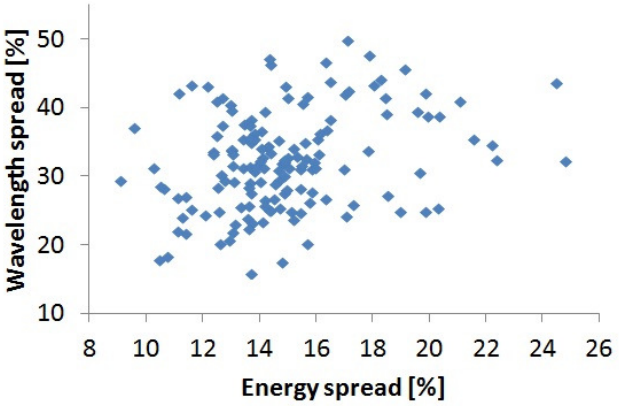

Figure 7.15: Radiation wavelength bandwidth as a function of electron energy spread.

Another important aspect coming out from the data analysis is that on the low resolution electron spectrometer, there is no trace of the large pedestal (low energy features) that have been observed on the high resolution electron spectrometer (ES1) placed just before the undulator. In fact, fig. 7.16 shows 5 shots recorded on ES1 on the same day as recorded undulator radiation. It is clear to see the high energy peak and a long pedestal, which contains up to 70% of the total electron charge.

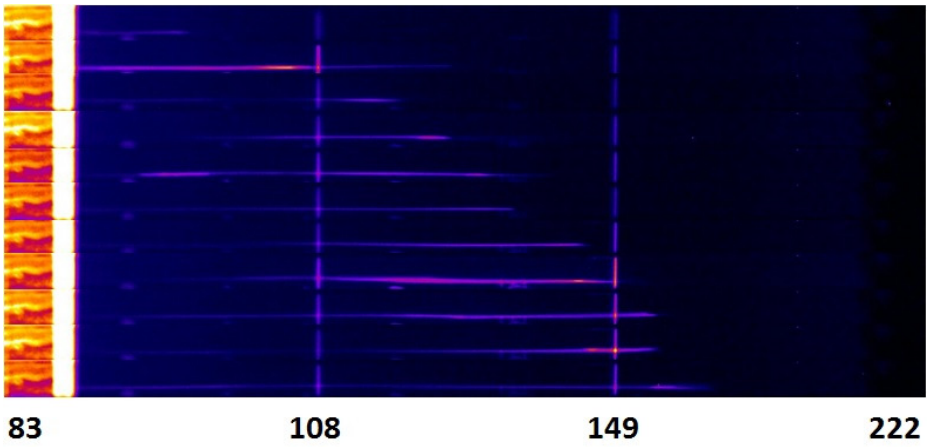

Figure 7.16: Electron energy spectra measured on the high resolution electron spectrometer (high energy window).

This aspect has been noticed also on the Lanex screens placed before and after the undulator (L3 and L4 respectively); on L3, in fact, the mean charge over 10 consecutive shots is 4.5 pC while on L4 is 2.3 pC. Therefore, it is concluded that beam loss along the undulator is dominated by loss of low energy pedestal electrons and that beam loss for the main peak electrons is reasonably low (~30%).

The next correlation is that between the number of photons emitted by the undulator and the charge of the electrons. Chapter 3 discussed the relation that there must be between these two parameters in order to measure coherent or incoherent effects. Incoherent effects produce a linear trend but, if there are coherent effects, then this dependence is quadratic.

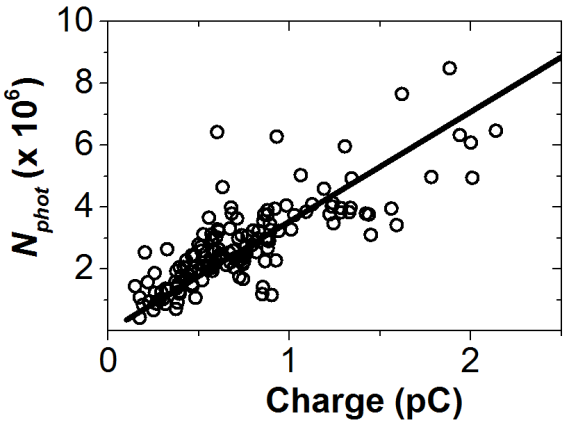

Figure 7.17: Number of photons versus charge of the electrons.

As seen in fig. 7.17, the measured trend is linear and therefore there are no observable coherent effects. The reason is that the transport for this experiment was not matched with the undulator, since the measured mean energy was much lower than the optimum expected value. A consequence of the mismatch is a low brightness electron bunch (with a longer duration and a larger focal spot). To make matters even worse, the energy spread measured during the experimental campaign was too high (much higher than the undulator parameter). However, the total number of detected photons is up to 8 x 10^6 (as seen in fig. 7.18) which is around 1-2 orders of magnitude higher than that obtained in the two previous experiments [63,163]. Moreover, as it is evident from fig. 7.18, the radiated

photons do not all reach the spectrometer, since the angular acceptance of the spectrometer is smaller (2 mrad) than the actual radiation size (1 to 5 mm).

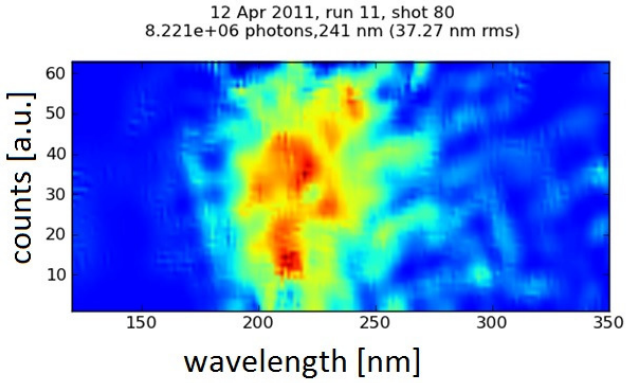

Figure 7.18: The highest number of photons measured during the undulator experimental campaign.

The last correlation is that between the number of photons per unit charge as a function of the electron energy; the energy range is the one measured during the experimental campaign, which is between 90 MeV to 115 MeV. The interval has been divided in 5 groups with a 5 MeV interval, as shown in fig. 7.19.

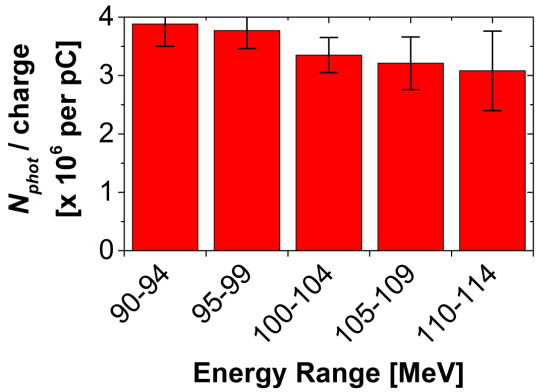

Figure 7.19: Number of photons per unit charge as a function of electron energy binned at 5 MeV intervals. The dataset comprises 137 shots.

Figure 7.19 shows that a significant increase in the efficiency of photon production has been obtained at lower electron energy; this behaviour can be attributed to the

focusing effect imparted on the electrons with energy less than 100 MeV energy by the slotted undulator field.

7.5 Discussion

This chapter summarised all the various undulator radiation experiments that have been performed. In the first part, the radiation detected with a CCD camera has been described. The first experiment has been done using a CCD camera with an objective lens tracing back the undulator radiation at the centre of the undulator. For this experiment, the camera's objective was focusing at the centre of the undulator and with this initial set-up, it was possible to see the first light coming from the wiggling of electrons in the undulator. This experiment has been very important, not only to see the radiation, but also to understand that the undulator was misaligned. The image of the radiation, however, has been used to estimate the divergence of the radiation cone which, assuming an electron mean energy of 100 MeV with a radiation rms sigma of 1.5 mm at a distance of 1.5 m, was approximately 1 mrad.

The same type of experiment has been performed by replacing the camera's objective with a series of lenses to collimate the radiation beam and focus it onto the CCD. In this case, the measured size of the radiation beam was 180 µm.

Eventually, the camera has been replaced by an Oriel optical spectrometer coupled to a 250 x 2000 pixel Hamamatsu camera. In this way, it has been possible to measure the first UV radiation spectra with a wavelength peak between 270 nm and 300 nm.

After this first experimental campaign, the undulator has been re-aligned onto the beam line axis and, at the same time, the detection system has been upgraded with a McPherson vacuum scanning monochromator coupled to a 16-bit Andor Newton ICCD camera. In addition, the permanent magnet quadrupole triplet placed after the undulator was upgraded to a new set-up with the purpose to collimate electron bunches exiting the accelerator with a mean energy of 130 MeV, ensuring a 3 fs

duration at the undulator entrance (in fact for this experiment the quadrupoles were much closer to the gas jet to avoid the lengthening of the bunch after exiting the plasma due to space-charge effects). With the new spectrometer, the higher electron energy and the undulator aligned, it has been possible to measure undulator radiation with a wavelength in the range 180-265 nm corresponding to an electron energy of 83-131 MeV. However, the quality of the electron bunches was not as high as required to drive an FEL. In fact, because the mean electron energy during the experiment was 95 MeV, well below the expected 130 MeV, the bunch duration at the undulator entrance was 1 order of magnitude higher (estimated from simulation to be around 30 fs), which lowered the peak current at the undulator entrance from the 1.5 kA expected to only 0.35 kA. Also the energy spread, which plays a fundamental role, was too high (the average was about 15%) compared to the ρ FEL parameter which was estimated to be 1.15×10^{-3} (at 95 MeV, with a peak current of 0.35 kA). And unfortunately the linear trend between the number of photon emitted and the electron beam charge linear have confirmed that no coherent effects have been observed during the experimental campaign.

However, a maximum total number of photons per shot of 8×10^{6} has been recorded, which is about 1-2 orders of magnitude higher than that obtained in the two previous experiments [63,163]. Moreover, the estimated mean number of photons per shot per $mrad^2$ per 0.1% bandwidth is ≈2200 with a mean energy of 2.6 pJ and mean peak brilliance of up to:

$$1 \cdot 10^{18}\ photons/s/mrad^2/mm^2/0.1\%\ bandwidth \qquad [7.5]$$

based on the measured radiation divergence of 2 mrad, estimated source diameter of 300 μm and minimum rms duration of 100 fs, a value that is similar to that of a 3rd generation synchrotron. This is higher than the estimated values of:

$$6.5 \cdot 10^{16}\ photons/s/mrad^2/mm^2/0.1\%\ bandwidth \qquad [7.6]$$

obtained in the visible [163] spectral range and:

$$1.3 \cdot 10^{17}\ photons/s/mrad^2/mm^2/0.1\%\ bandwidth \qquad [7.7]$$

obtained in the extreme UV [63] spectral range where longer bunch duration estimates were applied. The relatively long radiation pulse duration in experiments

here is a sum of the mean electron duration (28 fs simulated) and mean radiation slippage duration $\left(N_u \lambda_r / c = 72 fs\right)$.

Moreover, because the radiation source is driven by ultra-short electron bunches (in the scale of few femtosecond) and it is itself as short as the electrons, becomes potentially interesting for ultra-fast science; of immediate application interest in the UV range is ultra-fast spectroscopy [164,165], of photo- and biochemical process, so-called femtochemistry [166] and femtobiology [167] , with sub-10 fs temporal resolution.

Another strong motivation for minimising bunch duration is the opportunity to improve the coherence properties of the radiation. Very short bunches or even those with a rapid longitudinal structural variation, such as its leading edge rise time, can generate large Fourier components at the radiation wavelength λ that drive coherent spontaneous emission (CSE) [168] and, ultimately, FEL operation. Longer wavelength systems have demonstrated that bunch rise time of about 10 λ \c, are sufficiently rapid to seed self-amplified coherent spontaneous emission (SACSE) in FELs [169,170]. At λ = 150 nm, for example, this corresponds to a threshold rise time of $\sim$5 fs, i.e., an rms duration of 3 fs (assuming Gaussian profile). For the ALPHA-X beam line set-up, the CSE condition is close to being fulfilled at the resonant electron energy of about 120 MeV.

Chapter 8

Conclusions

8.1 Overview

In this chapter a summary of all the results will be given, starting from the techniques used for the FEL and transport simulations, the experimental results and eventually the last part will be dedicated to future research and possible improvements that can be overseen to improve both simulations and experiments.

8.2 Techniques

8.2.1 FEL simulations

There are two codes described in this thesis that have been used to perform FEL simulations: one is GENESIS and the other one is SIMPLEX.

GENESIS is a simulation code used to calculate the performance of FELs, where the kinetic energy of electrons is transferred into a tuneable, high-brightness radiation source. A 4th order Runge-Kutta solver integrates the equation of motion for the electron energy and phase while a symplectic solver tracks the transverse variables through the magnetic lattice of the undulator. There are other two features incorporated with the propagation of the electron beam. The effect of energy loss due to spontaneous radiation and the growth of the energy spread due to quantum fluctuations of the spontaneous radiation follow an analytical model [127] and is applied to the particle distribution without introducing unphysical bunching effects in the longitudinal phase space. The second feature is the effect of wakefields on the electron beam which is mainly modelled by a mean energy loss per integration step [128]. The only feature that is still not optimised with GENESIS is the time-dependent simulation tool for ultra-short electron bunches.

SIMPLEX is application software used to support design of accelerator components in FEL facilities and help the FEL users to estimate the optical properties of the FEL radiation. This code has been written to investigate phenomena in FELs, such as

radiation power growth, electron motion in phase space, evolution of angular and spatial profile of radiation field, etc. and has been developed at Spring-8 in Japan.

8.2.2 Beam transport simulations

For the transport simulation as well, two codes have been used to perform simulation: General Particle Tracer (GPT) and TRANSPORT.

GPT is a software package developed to study 3D charged particle dynamics in electromagnetic fields [133]. Using this code, it is possible to create an electron bunch and propagate it through all kinds of devices.

TRANSPORT is a very powerful transport code which considers space-charge effects and first and second order solutions of the motion equations [143].

Figures 4.30 and 4.31 showed the simulated transport along the ALPHA-X beam line, with the same quadrupole specification, for 250 MeV and 450 MeV electron bunches. There is strong agreement between the two codes: the main difference is at the focus and is due to the fact that GPT is able to use field maps for the PMQs and the undulator which leads to a more precise description of the beam line while, with TRANSPORT, this is not possible and therefore both the PMQs and the undulator are described using its internal simplified models (normal quadrupoles for the PMQs and an array of dipoles with alternate field for the undulator).

The decision to use the GPT code to simulate the whole ALPHA-X beam line for all the simulations shown in this thesis is because of the easy checking thant can be made of the behaviour of the transport due to different initial bunch parameters. Moreover, using the GPT code, it has been possible to design new components of the beam line: a triplet of permanent magnet quadrupoles and a low resolution electron spectrometer. Both of these elements have been of paramount importance: the quadrupoles for the transport of up to 80% of charge for the 5.5 m length of beam line, by maintaining the quality of the electron bunch; and the low resolution electron spectrometer placed at the end of the beam line, which has allowed simultaneous measurement of the electron beam energy and the undulator radiation.

8.2.3 Experiments

The ALPHA-X beam line is a straight 7 m long beam line, composed of the LWFA accelerator (able to accelerate electrons to the hundreds MeV energy level with a 2 mm gas jet), a triplet of permanent magnet quadrupoles (placed a few cm from the accelerator and used to lower the electron beam pointing instability and to maintain the quality of the incoming electron bunch), a triplet of electromagnetic quadrupoles (the centre of which is 1.6 m from the accelerator), then there is a high resolution electron spectrometer (placed 55 cm from the end of last quadrupole) which is followed, 0.9 m after, by a 1.5 m long 100 period undulator. A layout of the beam line is shown in fig. 8.1.

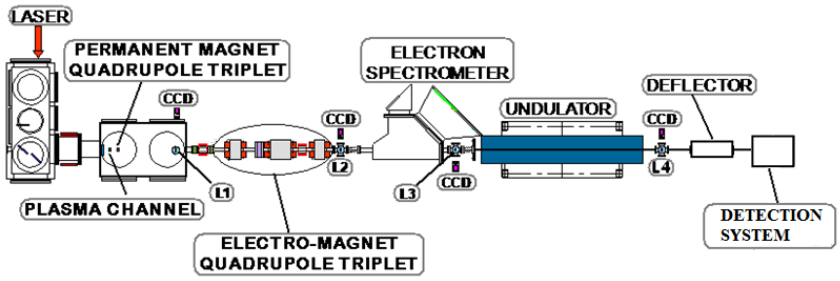

Figure 8.1: Schematic of the ALPHA-X beam line.

The whole beam line is populated by pop-in targets (Lanex scintillating screens covered by a layer of aluminium to block the laser light) which can be inserted in or out of the electron's path used to check the pointing of the electron bunch and its spatial distribution. Targets are all observed by 12- or 14-bit CCD cameras.

At the end of the beam line, for the FEL experiments, there is a radiation detection system: this has been changed different times for different experimental purposes. Initially, there was a 12-bit CCD camera coupled with an objective set to image the radiation at the centre of the undulator, which has allowed first observation of radiation from the undulator. During this experiment, radiation with a divergence cone of 1 mrad has been observed.

The next experiment has been to remove the camera's objective and replace it with a pair of lenses (1.5 m diverging lens plus a 10 cm focusing lens); during this experiment a radiation spot size (rms sigma) of 180 µm has been measured.

Eventually, the camera has been replaced with an Oriel spectrometer coupled with a 1 x 2000 pixel Hamamatsu CCD camera. With this new set-up, the first series of undulator radiation spectra in the range of wavelength between 200 nm and 500 nm has been measured.

The most important achievement of these series of experiments has been to realise that the undulator was significantly misaligned.

During undulator alignment that then took place, two major changes to the experimental set-up have been made: the permanent quadrupole triplet have been upgraded to optimise the transport for higher energy electron (130 MeV) and the detection system has been upgraded with a McPherson vacuum scanning monochromator coupled to a 16-bit Andor Newton camera (250 x 2000 pixel resolution). The new detection system is optimised to measure radiation in the VUV region of the electromagnetic spectrum. With this new set-up, undulator incoherent radiation with spectrum peaked in the VUV region down to 180 nm has been measured.

8.3 Summary of the results

8.3.1 LWFA-driven FEL simulations

Two different codes have been used to perform FEL simulations, SIMPLEX and GENESIS; the two codes are very similar to each other and the first thing that comes to mind is that SIMPLEX has a friendlier interface. However, after using the two codes, a huge difference has been found. Before discussing this problem, it is important to underline that FELs have been very well explored (both from a theoretical and an experimental point of view) as an “extension” to synchrotrons

and linacs, where the accelerating physics is very well known and all the simulation codes have been written for these kind of conditions.

The LWFA, as discussed throughout the thesis, is very different from a conventional accelerator, not only from a compactness point of view, but also for the quality of the electron bunches that are accelerated. The most different parameter between the two types of accelerator is the duration of the bunch which, in the case of LWFA, is in the fs scale. And this is the problem encountered; FEL codes, in fact, can solve the FEL equations in two different regimes, the steady-state regime (where the electron bunch is considered to be infinitely long so as to fill the whole undulator) and the time-dependent regime (where the beam has a finite duration and slippage effects become important). Of course, both codes can successfully simulate the steady-state regime, but only SIMPLEX is able to simulate the ultra-short electron bunches driven by an LWFA. The important task of an FEL simulation code in the time-dependent regime is to slice the bunch and propagate them through the undulator to see the effect of each slice on the final radiation. GENESIS has very strict rules to be fulfilled in the choice of the number of slices: the number of slices in which an ultra-short electron bunch can be split in is not enough to be able to have a valid time window to resolve the spectrum.

The same limitation is not found with the SIMPLEX code which is able to accurately predict the behaviour of the undulator in both regimes.

8.3.2 Simulations of optimal beam transport

In Chapter 6 all the experiments that have been performed on the ALPHA-X beam line concerning the transport of the electron bunches produced by the 2 mm helium gas jet have been presented. In particular, two different scenarios have been explored, which consist of two different set-ups for the permanent magnet quadrupole triplet. The first set-up has been designed mostly to experimentally check the quadrupoles and compare the simulations with the measurement to provide confidence about the predictions. This set-up was very simple and consisted of a sandwich of quadrupoles (outer quadrupoles and middle quadrupole attached

to each other) placed, with respect to the accelerator, so that the bunch divergence was highly reduced for a large range of energies (from 50 MeV up to 1 GeV).
The first experiments have shown that the quadrupoles were very efficient and that simulations and measurements were in very good agreement.
The second set-up has been specially designed for a very small range of energies (centred on 130 MeV, which was the average day-by-day energy produced by the accelerator in a previous experimental campaign). The main difference between the two set-ups is the spacing between the quadrupoles and the displacement of the triplet with respect to the accelerator: in fact, while in the first case the quadrupoles are attached to one another and placed 15 cm from the gas jet, in the second case, the quadrupoles are separated from each other (5 cm) and positioned very close to the gas jet (the first quadrupole is only 3 cm far from the gas jet exit). The measured beam sizes coming from this set-up as well have been compared to the expected beam sizes and, again, very good agreement between simulations and experiments has been found.

8.3.3 Effective beam transport experiments

As stated in the previous section, transport simulations have been found to be in very good agreement with experimental measurements. In Chapter 6 all the detailed analysis of the two different set-ups has been summarised. In particular, in section 6.3.1, the summary of transport experiments for the first set-up, with the quadrupoles attached to each other and placed 15 cm from the accelerator, have been reported; in the same section, beam profile measurements on each Lanex scintillating screen have been reported and a comparison between the expected beam size predicted using the GPT simulations and the beam size measured during the experiment has been given. Tables 8.1 and 8.2 summarise the results.

	Energy	L1	L3	L4
X dimension	80 MeV	1.2 mm	1.45 mm	1.3 mm
Y dimension	80 MeV	1.0 mm	0.9 mm	2.0 mm

Table 8.1: Expected beam sizes on the different Lanex screens as predicted by the GPT code.

	Energy	L1	L3	L4
X dimension	80 ± 5 MeV	1.4 ± 0.5 mm	1.4 ± 0.5 mm	1.5 ± 0.5 mm
Y dimension	80 ± 5 MeV	1.2 ± 0.4 mm	1.1 ± 0.5 mm	1.8 ± 0.6 mm

Table 8.2: Measured beam sizes on the different Lanex screens averaged over 50 shots.

The measurements and the predictions are very close and this is a very important achievement because predictions of the spot size of the electron beam at the centre of the undulator can be made with high confidence.

Similar analysis has been carried out using the updated permanent magnet quadrupoles set-up, which has been designed to quasi-collimate the high energy electron beam exiting the accelerator while maintaining the ultra-short duration. However, in this case, the data analysis has been more difficult because, while with the other set-up, the electron beam quality and stability was very high, in this case very large energy fluctuations were measured (between 90 and 160 MeV) and also the energy spread of the electron bunches was very high (of the order of 15%).

Because the spot size measurement are achieved with a destructive technique, making it impossible to measure simultaneously the spot size and the corresponding energy, comparison between measurement and predictions becomes much harder. To overcome this problem, a table of the expected beam size at different energies with a binning of 10 MeV in the range between 90 and 160 MeV has been compiled (table 8.3) and compared with the effective measurement (table 8.4).

As shown in table 8.4, the errors on the measurements is very high, due to the energy fluctuations, but the range of sizes measured is definitely within the expected beam size.

Energy [MeV]	Lanex L1		Lanex L2		Lanex L3	
	σ_x [μm]	σ_y [μm]	σ_x [μm]	σ_y [μm]	σ_x [μm]	σ_y [μm]
90	220	1120	1460	1960	4010	7690
100	100	630	1200	180	1620	1210
110	170	270	770	600	890	590
120	310	110	280	360	380	100
130	420	200	250	140	180	150
140	510	350	720	730	660	330
150	590	480	1180	1310	1120	1350
160	660	580	1590	1860	1640	2340

Table 8.3: Expected beam sizes on the different Lanex screens at different electron energies.

	Energy	L1	L3	L4
x dimension	[90,160] MeV	400 ± 530 μm	660 ± 690 μm	500 ± 210 μm
y dimension	[90,160] MeV	420 ± 290 μm	600 ± 200 μm	510 ± 280 μm

Table 8.4: Beam sizes obtained analysing 50 consecutive shots on each Lanex screen during experiments, using the optimised quadrupole setting for 130 MeV.

8.3.4 LWFA-driven VUV undulator radiation experiments

Different experiments have been carried out to detect the undulator radiation emitted from the 1.5 m long planar ALPHA-X undulator. In the first stage, a CCD camera with an objective has been used, with the objective set to image the radiation at the centre of the undulator. With this experiment a radiation beam with size (sigma) 1.4 mm x 1.3 mm has been measured. After this experiment, the objective has been replaced with two lenses (1.5 m and 10 cm focal length respectively), in order to find the focal plane of the radiation for the further update. These two experiments have been fundamental to find that the undulator was misaligned.

After aligning the undulator, the detection system has been updated by replacing the CCD camera with an optical Oriel spectrometer. Using this new set-up, the first radiation spectra have been measured. The electron energy during this experiment was in the range 80-90 MeV and the corresponding detected radiation wavelength was in the UV range (275 nm to 320 nm). The maximum number of photons detected during this experiment was $0.5 \times 10^6 \pm 6 \times 10^3$.

Eventually, the detection system has been upgraded again in order to detect VUV radiation, which was not detectable using the Oriel spectrometer. For this reason, a McPherson detector coupled to an Andor ICCD camera has been mounted on the vacuum beam line. During this experiment, the major results presented in this thesis have been recorded. The electron energy for this experiment is higher than the previous experiment, reaching the 130 MeV. In particular, for this experiment the permanent magnet quadrupoles have been optimised in order to transport more efficiently the electrons with this high energy and, in particular, to keep the bunch duration as short as possible and have a high peak current at the undulator centre. However, as shown in detail in Chapter 7, the electron energy did not match the expected energy, causing a mismatched transport and also a large energy spread has definitely played a significant role in the degradation of the FEL performance. For this experiment, radiation with wavelength in the VUV region of the electromagnetic spectrum (between 199 nm and 265 nm corresponding to an electron energy between 131 MeV and 83 MeV) has been measured. However, a maximum total number of photons per shot of 8×10^6 has been recorded, which is 1-2 orders of magnitude higher of magnitude higher than that obtained in the two previous LWFA-driven undulator radiation experiments [63,163].

8.4 Thesis conclusions

During this work, the entire ALPHA-X beam line after the accelerator has been simulated, with models that were as close as possible to reality. This work has been carried out using the GPT transport code, which can include 3D field maps of all the

different electromagnetic pieces of equipment, and a wide range of electron energies has been taken into account during simulations (from 50 MeV up to 1 GeV), especially in the first stage when the energy that could be reached from the ALPHA-X accelerator was still largely unknown. Using the same code, two triplets of permanent magnet quadrupoles have been designed, which can be easily adapted to different electron energy and transport situations. The agreement between simulations and transport experiment has been verified and the necessity to include inside the code the effect of laser beam filters has been encountered. During experiments, in fact, it was observed that by using the same kind of laser filter but placed in different positions along the beam line, the recorded beam size was different, demonstrating that the effect of multiple scattering from these filters is to increase the emittance of the beam. GEANT4 simulations have confirmed this hypothesis, showing an increase of the emittance by up to a factor of 3 depending on the thickness of the beam blocker foil. Of course, this is not a problem from a transport point of view because, for transport experiments, the closest laser beam block to the target can always be used but for the FEL experiment this is a huge problem, mainly because the emittance is a property of the beam that can only grow and cannot be reduced such that the transport of a beam with a 3 times larger emittance is very different, leading to a larger focal waist.

However, from an experimental point of view, there is merit in the good agreement between the GPT transport code and the measurements, but the same cannot be said about FEL experiments because, as discussed in section 8.6 later, the degradation of electron beam quality caused degradation of possible FEL performance.

8.5 Wider implications

As has been discussed, the main problem during the experiments relates to the quality of the electron bunches. FEL operations need very high quality electron bunches; theory demonstrated that the electron bunches exiting the accelerator

have a very high quality but, due to space-charge effects, they tend to explode very rapidly and therefore the main problem is to maintain the high quality during propagation. In general, this is not a problem also because there are many different transport codes that have been heavily used for conventional accelerators and are robustly tested; the transport becomes difficult when the quality of the electron bunch changes from shot-to-shot.

During experiments, in fact, it has been seen that day-by-day the accelerating conditions at that time were changing greatly and the quality of the bunches were largely different. It is unknown what was the main parameter or parameters causing the differing accelerating conditions and, therefore, day-by-day work is achieved without full knowledge of all parameters that define stability. This is a major problem because it is well known, and has been discussed several times in this thesis, that different electron energies have different transport conditions (different distances between quadrupoles, different current settings for the electromagnets and different undulator radiation wavelength to detect). So the most important task at hand is to deeply understand the injection process in order to understand and control this complicated process such that good quality, stable electron bunches are reliably generated.

8.6 Future research

8.6.1 FEL simulations

In the future, from an FEL simulation point of view, it is very important to adapt the well-known and tested GENESIS code to the ultra-short electron bunches driven by an LWFA. Chapter 3, in fact, discussed the problem of the slicing process with GENESIS. The main difference between the time-independent and the time-dependent simulations is that, in the first case, the beam is considered to have an infinite extension in time (filling the whole undulator) while, in the time-dependent simulation, the beam has a finite extension (a real bunch length) and in order to

reconstruct the radiation output, the bunch is divided in slices and propagated through the undulator. The main problem comes from the fact that the code requires each slice to have a thickness that is at least one radiation wavelength λ and, therefore, the time discretisation has to be $c\Delta t \geq \lambda$ to avoid overlapping of the slices. Consider an electron bunch accelerated by the LWFA technique at an energy of 100 MeV (which yields a radiation wavelength of around 200 nm for a dimensionless undulator parameter k = 0.38). In order to fully slice the ultra-short electron bunch (1-3 fs duration), the maximum number of slices will be only 4 and, with such a small number of slices, the code is not able to have a valid time window and resolve the spectrum.

8.6.2 Beam transport simulations

There are many different things that could be investigated in the future to improve transport simulations. The GPT code, which has been used and tested on the ALPHA-X beam line, could be expanded to include effects of interaction of electrons with materials, for example, laser beam filters. Another important improvement that can be introduced to this code is also the FEL effect: to enable the use of only one code to do a start-to-end simulation, including optimal transport and FEL conditions, could be very important and could simplify the simulations, avoiding, for example, mistakes with different expressions or units of different parameters. Also, for start-to-end simulations, the GPT code could also be expanded to include the acceleration process; at the moment, in fact, the code takes a bunch of electrons already accelerated and propagates it through a beam line. It's a very powerful code and gives both the possibility to create a bunch or to use an external file with a 3D map of particles generated from another code but to be able to perform valid start-to-end simulations, it would be preferable to have only one code.

Another alternative could be to model the whole beam line with another code, for example, GEANT4 which is a very powerful code capable not only of generating a bunch of particles and transporting it along a beam line, but also of simulating the effect of a laser beam filter on the electron bunch. Moreover, it has a better

graphical interface with respect to GPT and, therefore, the beam line can be visualised while it is simulated. With GPT this is not possible and sometimes it has been very difficult to understand part of the simulations because GPT uses a very hard-to-understand method to rotate objects!

8.6.3 High beam quality for FEL operation

There are 3 critical parameters which can drastically deteriorate the FEL operations: the emittance, the energy spread and the bunch duration. This set of parameters defines the brightness of the electron bunch, which is the current per unit area per unit of solid angle and can be expressed as:

$$Brightness = \frac{eN_b}{2\pi\sigma_z \, \sigma_\gamma / \gamma} \qquad [8.1]$$

where N_b is the number of electrons, σ_z is the bunch length, σ_γ / γ is the energy spread and the denominator corresponds to the longitudinal beam emittance. The brightness of the bunch is a fundamental parameter in FEL theory because the higher this parameter, the better the FEL operates.

Experiments show that it is possible to have monoenergetic electron bunches from a LWFA: on the ALPHA-X project, an energy spread down to 0.4% has been measured. However, it is still not very well known which parameters (from a laser point of view) can control in a reliable way the energy spread. High energy spread leads to a low brightness and severe transport problems and, therefore, a method to produce and maintain a low energy spread is important.

The emittance is, at the moment, one of the most critical parameters. On the ALPHA-X beam line, the emittance at a distance of 80 cm from the accelerator has been found to be as low as 1.1 π mm mrad, but the stability from shot-to-shot is critical; the bunch duration at about 1 m from the accelerator has also been measured to be 2 fs. For the future, it will be very interesting to do the same measurements at various positions along the beam line to determine how and where these two quantities grow. Of course, the ideal method would be to measure all the electron bunch quality parameters in a single shot in a non-destructive way

so it could be very interesting to introduce some non-destructive method to measure both the emittance and the bunch duration. Such a powerful diagnostic tool would back-up start-to-end simulations in order to gain an overall understanding if the propagation of ultra-short electron bunches along the beam line.

However, it is known that inside the accelerating structure the emittance is very low and can be as small as few hundred of μm mrad [171,172] and when the electrons leave the bubble, the bunch can be compressed (the bunch is very small in size and very short in time); when the electrons leave the bubble, the huge electromagnetic field that was controlling the expansion of the bunch becomes zero instantly and because all these particles are so compressed, they expand immediately due to space-charge effects, which leads to a large growth of the emittance and bunch duration. The only way to minimise the emittance and bunch duration growth is to start controlling the bunch as soon as it leaves the bubble and at the moment, the use of high gradient, compact permanent magnet quadrupoles to be placed as close as possible to the exit of the accelerator, seems to be the best solution. But this is not a definitive solution: the emittance and bunch duration will grow anyway and because the emittance once grown cannot be reduced, it is not possible to recover the same brightness that the bunch possessed inside the bubble at its exit. For this reason it could be very interesting to study novel kinds of FELs to be placed in the same location where the acceleration is happening, e.g. plasma undulators or wigglers. One way to do this can be to use a counter-propagating laser beam that acts as a moving undulator or a laser beam that propagates in the same direction as the electrons but that is not used for acceleration.

Other innovative way to drive an FEL from an LWFA could be external injection. In fact, conventional accelerators benefit from high reproducibility, good stability and good quality of accelerated electron bunches. The challenge with this kind of experiment will be to use a plasma accelerator to further accelerate the electrons exiting the conventional accelerator while maintaining the quality of the electron

bunch. If that could be possible, then it will be much easier to use conventional FELs to produce high brightness coherent radiation.

References

[1] L. Laurent, *"High Gradient RF Breakdown Studies"*, Ph.D. Dissertation, UC Davis, 2002.

[2] R. Tomas, *"Overview of the Compact Linear Collider"*,Phys. Rev. ST Accel. Beams **13**, 014801 (2010).

[3] V. Malka, S. Fritzler, E. Lefebvre, M.M. Aleonard, F. Burgy, J.P. Chambaret, J.F. Chemin, K. Krushelnick, G. Malka, S.P. Mangles, Z. Najmudin, M. Pittman, J.P. Rousseau, J.N. Scheurer, B. Walton, A.E. Dangor, *"Electron acceleration by a wakefield forced by an intense ultrashort laser pulse"*, Science **298**, 1596 (2002).

[4] W.P. Leemans, P. Catravas, E. Esarey, C.G.R. Geddes, C. Toth, R. Trines, C.B. Schroeder, B.A. Shadwick, J. Van Tilborg, J. Faure, *"Electron-yield enhancement in a laser-wakefield accelerator driven by asymmetric laser pulses"*, Phys. Rev. Lett. **89**, 174802 (2002).

[5] T. Tajima, J.M. Dawson, *"Laser electron accelerator"*, Phys. Rev. Lett. **43**, 267 (1979).

[6] E. Esarey, P. Sprangle, J. Krall, A. Ting, *"Overview of plasma-based accelerator concepts"*, IEEE Trans. Plasma Sci. **24**, 252 (1996).

[7] A. Modena, Z. Najmudin, A.E. Dangor, C.E. Clayton, K.A. Marsh, C. Joshi, V. Malka, C.B. Darrow, C. Danson, D. Neely, F.N. Walsh, *"Electron acceleration from the breaking of relativistic plasma waves"*, Nature, **377**, 606 (1995).

[8] D. Umstadter, S.Y. Chen, A. Maksimchuk, G. Mourou, R. Wagner, *"Nonlinear optics in relativistic plasmas and laser wake field acceleration of electrons"*, Science **273**, 472 (1996).

[9] K. Nakajima, D. Fisher, T. Kawakubo, H. Nakanishi, A. Ogata, Y. Kato, Y. Kitagawa. R. Kodama, K. Mima. H. Shiraga. K. Suzuki. K. Yamakawa. T. Zhang, Y. Sakawa, T. Shiji, Y. Nishida. N. Yugami. M. Downer, T. Tajima, *"Observation*

of Ultrahigh Gradient Electron Acceleration by a Self-Modulated Intense Short Laser Pulse", Phys. Rev. Lett. **74**, 4428 (1995).

[10] S.P.D. Mangles, C.D. Murphy, Z. Najmudin, A.G.R. Thomas, J.L. Collier, A.E. Dangor, E.J. Divall, P.S. Foster, J.G. Gallacher, C.J. Hooker, D.A. Jaroszynski, A.J. Langley, W.B. Mori, P.A. Norreys, F.S. Tsung, R. Viskup, B.R. Walton, K. Krushelnick, "*Monoenergetic beams of relativistic electrons from intense laser–plasma interactions*", Nature **431**, 535 (2004).

[11] C.G.R. Geddes, C. Toth, J. van Tilborg, E. Esarey, C.B. Schroeder, D. Bruhwiler, C. Nieter, J. Cary, W.P. Leemans, "*High-quality electron beams from a laser wakefield accelerator using plasma-channel guiding*", Nature **431**, 538 (2004).

[12] J. Faure, Y. Glinec, A. Pukhov, S. Kiselev, S. Gordienko, E. Lefebvre, J.P. Rousseau, F. Burgy, V. Malka, "*A laser–plasma accelerator producing monoenergetic electron beams*", Nature **431**, 541 (2004).

[13] A. F. Lifschitz, J. Faure, V. Malka, P. Mora, "*GeV wakefield acceleration of low energy electron bunches using petawatt lasers*". Phys. Plasmas **12**, 093104 (2005).

[14] S. Gordienko, A. Pukhov, "*Scalings for ultrarelativistic laser plasmas and quasi-monoenergetic electrons*", Phys. Plasmas **12**, 043109 (2005).

[15] D.J. Spence, S.M. Hooker, "*Investigation of a hydrogen plasma waveguide*", Phys. Rev. E **63**,015401 (2001).

[16] A. Butler, D.J. Spence, S.M. Hooker, "*Guiding of high-intensity laser pulses with a hydrogen-filled capillary discharge waveguide*". Phys. Rev. Lett. **89**, 185003 (2002).

[17] W.P. Leemans, B. Nagler, A.J. Gonsalves, Cs. Tóth, K. Nakamura, C.G.R. Geddes, E. Esarey, C.B. Schroeder, S.M. Hooker, "*GeV electron beams from a centimetre-scale accelerator*", Nature Phys. **2**, 696 (2006).

[18] K. Nakamura, B. Nagler, Cs. Tóth, C.G.R. Geddes, C.B. Schroeder, E. Esarey, W.P. Leemans, A.J. Gonsalves, S.M. Hooker, *"GeV electron beams from a*

centimeter-scale channel guided laser wakefield accelerator", Phys. Plasmas **14**, 056708 (2007).

[19] S. Karsch, J. Osterhoff, A. Popp, T.P. Rowlands-Rees, Zs. Major, M. Fuchs, B. Marx, R. Hörlein, K. Schmid, L. Veisz, S. Becker, U. Schramm, B. Hidding, G. Pretzler, D. Habs, F. Grüner, F. Krausz, S.M. Hooker, *"GeV-scale electron acceleration in a gas-filled capillary discharge waveguide"*, New J. Phys. **9**, 415 (2007).

[20] S. Cipiccia, M. Islam, B. Ersfeld, R. Shanks, E. Brunetti, G. Vieux, X. Yang, R. Issac, M.S. Wiggins, G. Welsh, M. Anania, D. Maneuski, R. Montgomery, G. Smith, M. Hoek, D. Hamilton, N. Lemos, D. Symes, P. Rajeev, O. Shea, J.M. Dias and D.A. Jaroszynski, *"Gamma-rays from harmonically resonant betatron oscillations in a plasma wake"*, Nature Phys. **7**, 867 (2011).

[21] N.A.M. Hafz, T.M. Jeong, I.W. Choi, S.K. Lee, K.H. Pae, V.V. Kulagin, J.H. Sung, T.J. Yu, K.-H. Hong, T. Hosokai, J.R. Cary, D.-K. Ko, J. Lee, *"Stable generation of GeV-class electron beams from self-guided laser–plasma channels"*, Nature Photonics **2**, 571 (2008).

[22] E. Brunetti, R.P. Shanks, G.G. Manahan, M.R. Islam, B. Ersfeld, M.P. Anania, S. Cipiccia, R.C. Issac, G. Raj, G. Vieux, G.H. Welsh, S.M. Wiggins, D.A. Jaroszynski, *"Low emittance, high brilliance relativistc electron beams from a laser-plasma accelerator"*, Phys. Rev. Lett. **105**, 215007 (2010).

[23] O. Lundh, J. Lim, C. Rechatin, L. Ammoura, A. Ben-Ismaïl, X. Davoine, G. Gallot, J.P. Goddet, E. Lefebvre, V. Malka, J. Faure, *"Few femtosecond, few kiloampere electron bunch produced by a laser-plasma accelerator"*, Nat. Phys. **7**, 219222 (2011).

[24] R.M. Phillips, *"Electron Devices"*, IRE Transactions **7**, 4, 231, (1960).

[25] B.N. Murdin, *"Far-infrared free-electron lasers and their applications"*, Contemp. Phys. **50**, 391 (2009).

[26] R. Bonifacio, F. Cerchioni, L. De Salvo Souza, P. Pierini and N. Piovella, *"Physics of the high-gain FEL and superradiance"*, Rivista del Nuovo Cimento, **3**, 1 (1990).

[27] J. Amann, W. Berg, V. Blank, F.-J. Decker, Y. Ding, P. Emma, Y. Feng, J. Frisch, D. Fritz, J. Hastings, Z. Huang, J. Krzywinski, R. Lindberg, H. Loos, A. Lutman, H.-D. Nuhn, D. Ratner, J. Rzepiela, D. Shu, Yu. Shvyd'ko, S. Spampinati, S. Stoupin, S. Terentyev, E. Trakhtenberg, D. Walz, J. Welch, J. Wu, A. Zholents, D. Zhu, *"Demonstration of self-seeding in a hard-X-ray free-electron laser"*, Nature Photonics **6**, 693 (2012).

[28] J.M. Madey, *"Stimulated Emission of Bremsstrahlung in a Periodic Magnetic Field"*, J. Appl. Phys. **42**, 1906, (1971).

[29] J.M.J. Madey, H.A. Schwettmann and W.M. Fairbank, *"A Free Electron Laser"*, IEEE Trans. Nucl. Sci. NS **20**, 905 (1973).

[30] P.L. Kapitza, P.A.M. Dirac, *"The reflection of electrons from standing light waves"*, Proc Cambridge Phil Soc **29**, 297 (1933).

[31] R.H. Pantell, G. Soncini and H.E. Puthoff, *"Stimulated photon-electron scattering"*, IEEE J. Quantum Electronics **4**, 905 (1968).

[32] V.P. Sukhatme and P.W. Wolff, *"Stimulated Compto scattering as a radiation source-theoretical limitations"*, J. Appl. Phys. **44**, 2331 (1973).

[33] M.S. Livingstom, J. Blewett, *"Particle Accelerators"*, McGraw-Hill (1962).

[34] E. Tanabe, *"Breakdown in high-gradient accelerator cavities"* (GSI--**84**-11). Angert, N. (Ed.). Germany (1994).

[35] R. Wideroe - US Patent 2,533,859 (1950).

[36] http://home.web.cern.ch/topics/large-hadron-collider

[37] http://www.bnl.gov/rhic/

[38] http://www.fnal.gov/pub/tevatron/tevatron-accelerator.html

[39] M.P. Marder, *"Condensed Matter Physics"*, John Wiley & Sons (2010).

[40] P.M. Chaikin and T.C. Lubensky, *"Principles of Condensed-Matter Physics"*, Cambridge University Press, **26**, 11, 940 (2001).

[41] G. Schatz, A. Weidinger, *"Nuclear condensed matter physics Nuclear methods and applications"*, J Wiley & Sons, (1996).

[42] https://www6.slac.stanford.edu/

[43] http://www.esrf.eu/

[44] http://www.aps.anl.gov/

[45] http://www.spring8.or.jp/en/

[46] http://www.diamond.ac.uk/

[47] http://www.xfel.eu/

[48] http://www.lightsource.ca/

[49] G. Vignola, The DAFNE Project Team, *"DAFNE: the Frascati Phi-Factory"*, Proceedings of PAC91, **68**, San Francisco, USA (1991).

[50] https://portal.slac.stanford.edu/

[51] http://www.bnl.gov/ps/

[52] http://xfel.riken.jp/eng/index.html

[53] http://www.psi.ch/sls/

[54] L.M. Chen, W.C. Yan, D.Z. Li, Z.D. Hu, L. Zhang, W.M. Wang, N. Hafz, J.Y. Mao, K. Huang, Y. Ma, J.R. Zhao, J.L. Ma, Y.T. Li, X. Lu and Z.M. Sheng, Z.Y. Wei, *"Bright betatron X-ray radiation from a laser-driven-clustering gas target"*, Scientific Reports **3**, 1912 (2013).

[55] K. Ta Phuoc, E. Esarey, V. Leurent, E. Cormier-Michel, C.G.R. Geddes, C.B. Schroeder, A. Rousse and W.P. Leemans, *"Betatron radiation from density tailored plasmas"*, Phys. Plasmas **15**, 063102 (2008).

[56] S. Corde, K. Ta Phuoc, R. Fitour, J. Faure, A. Tafzi, J. P. Goddet, V. Malka and A. Rousse, *"Controlled Betatron X-Ray Radiation from Tunable Optically Injected Electrons"*, Phys. Rev. Lett. **107**, 255003 (2011).

[57] S. Kneip, C. McGuffey, F. Dollar, M.S. Bloom, V. Chvykov, G. Kalintchenko, K. Krushelnick, A. Maksimchuk, S.P.D. Mangles, T. Matsuoka, Z. Najmudin, C.A.J. Palmer, J. Schreiber, W. Schumaker, A.G.R. Thomas, V. Yanovsky, *"X-ray phase contrast imaging of biological specimens with femtosecond pulses of betatron radiation from a compact laser plasma wakefield accelerator"*, Appl. Phys. Lett. **99**, 093701 (2011).

[58] S. Kneip, C. McGuffey, J.L. Martins, S.F. Martins, C. Bellei, V. Chvykov, F. Dollar, R. Fonseca, C. Huntington, G. Kalintchenko, A. Maksimchuk, S.P.D. Mangles, T. Matsuoka, S.R. Nagel, C.A.J. Palmer, J. Schreiber, K. Ta Phuoc,

A.G.R. Thomas, V. Yanovsky, L.O. Silva, K. Krushelnick, Z. Najmudin, *"Bright spatially coherent synchrotron X-rays from a table-top source"*, Nature Phys. **6**, 980 (2010).

[59] S. Cipiccia, S.M. Wiggins, R.P. Shanks, M.R. Islam, G. Vieux, R.C. Issac, E. Brunetti, B. Ersfeld, G.H. Welsh, M.P. Anania, D. Maneuski, N.R.C. Lemos, R.A. Bendoyro, J. Martins, F. Fiuza, M. Marti, P.P. Rajeev, P. Foster, N. Bourgeois, T.P.A. Ibbotson, P.A. Walker, V. O'Shea, J.M. Dias, L.O. Silva, S.M. Hooker, D.A. Jaroszynski, *"A tuneable ultra-compact bright gamma-ray source based on bremsstrahlung radiation from laser-plasma accelerated electrons"*, J. Appl. Phys. **111**, 063302 (2012).

[60] J. Galy, M. Maučec, D.J. Hamilton, R. Edwards, J. Magill, *"Bremsstrahlung production with high-intensity laser matter interactions and applications"*, New J. Phys. **9**, 23 (2007).

[61] A.L. Meadowcroft, R.D. Edwards, *"High-Energy Bremsstrahlung Diagnostics to Characterize Hot-Electron Production in Short-Pulse Laser-Plasma Experiments"*, IEEE Trans. Plasma Sci. **40**, 1992 (2012).

[62] J.G. Gallacher, M.P. Anania, E. Brunetti, F. Budde, A. Debus, B. Ersfeld, K. Haupt, M.R. Islam, O. Jäckel, S. Pfotenhauer, A.J.W. Reitsma, E. Rohwer, H.P. Schlenvoigt, H. Schwoerer, R.P. Shanks, S.M. Wiggins, D.A. Jaroszynski, *"A method of determining narrow energy spread electron beams from a laser plasma wakefield accelerator using undulator radiation"*, Phys. Plasmas **16**, 093102 (2009).

[63] M. Fuchs, R. Weingartner, A. Popp, Z. Major, S. Becker, J. Osterhoff, I. Cortrie, B. Zeitler, R. Hörlein, G.D. Tsakiris, U. Schramm, T.P. Rowlands-Rees, S.M. Hooker, D. Habs, F. Krausz, S. Karsch and F. Grüner, *"Laser-driven soft-X-ray undulator source"*, Nature Phys. **5**, 826 (2009).

[64] F. Grüner, S. Becker, U. Schramm, T. Eichner, M. Fuchs, R. Weingartner, D. Habs, J. Meyer-ter-Vehn, M. Geissler, M. Ferrario, L. Serafini, B. van der Geer, H. Backe, W. Lauth and S. Reiche, *"Design considerations for table-top,*

laser-based VUV and X-ray free electron lasers", Appl. Phys. B **86**, 3, 431 (2007).

[65] K. Nakajima, M. Kando, T. Kawakubo, T. Nakanishi, A. Ogata, *"A table-top X-ray FEL based on the laser wakefield accelerator-undulator system"*, Nucl. Instrum. Methods Phys. Res., Sect. A **375**, 593 (1996).

[66] J. van Tilborg, *"Coherent terahertz radiation from laser-wakefield-accelerated electron beams"*, PhD Thesis, Technische Universiteit Eindhoven (2006).

[67] J. van Tilborg, C.B. Schroeder, C.V. Filip, Cs. Tóth, C.G.R. Geddes, G. Fubiani, E. Esarey, W.P. Leemans, *"Terahertz radiation as a bunch diagnostic for laser-wakefield-accelerated electron bunches"*, Phys. Plasmas **13**, 056704 (2006).

[68] W.P. Leemans, C.G.R. Geddes, J. Faure, Cs. Tóth, J. van Tilborg, C.B. Schroeder, E. Esarey, G. Fubiani, D. Auerbach, B. Marcelis, M.A. Carnahan, R.A. Kaindl, J. Byrd, M.C. Martin, *"Observation of Terahertz Emission from a Laser-Plasma Accelerated Electron Bunch Crossing a Plasma-Vacuum Boundary"*, Phys. Rev. Lett. **91**, 074802 (2003).

[69] J. van Tilborg, C.B. Schroeder, C.V. Filip, Cs. Tóth, C.G.R. Geddes, G. Fubiani, R. Huber, R.A. Kaindl, E. Esarey and W.P. Leemans, *"Temporal Characterization of Femtosecond Laser-Plasma-Accelerated Electron Bunches Using Terahertz Radiation"*, Phys. Rev. Lett. **96**, 014801 (2006).

[70] G.R. Plateau, N.H. Matlis, O. Albert, C. Tóth, C.G.R. Geddes, C.B. Schroeder, J. van Tilborg, E. Esarey and W.P. Leemans, *"Optimization of THz Radiation Generation from a Laser Wakefield Accelerator"*, **CP1086**, AIP Conf. Proc. 1086, 707 (2009).

[71] S. Chen, A. Maksimchuk, D. Umstadter, *"Experimental observation of relativistic nonlinear Thomson scattering"*, Nature **396**, 653-655 (1998).

[72] P. Catravas, E. Esarey, W.P. Leemans, *"Femtosecond x-rays from Thomson scattering using laser wakefield accelerators"*, Meas. Sci. Technol. **12**, 1828 (2001).

[73] K. Ta Phuoc, A. Rousse, M. Pittman, J.P. Rousseau, V. Malka, S. Fritzler, D. Umstadter, and D. Hulin, *"X-Ray Radiation from Nonlinear Thomson Scattering of an Intense Femtosecond Laser on Relativistic Electrons in a Helium Plasma"*, Phys. Rev. Lett. **91**, 195001 (2003).

[74] H. Schwoerer, B. Liesfeld, H.P. Schlenvoigt, K.U. Amthor, R. Sauerbrey, *"Thomson-Backscattered X Rays From Laser-Accelerated Electrons"*, Phys. Rev. Lett. **96**, 014802 (2006).

[75] P. Tomassini, A. Bacci, J. Cary, M. Ferrario, A. Giulietti, D. Giulietti, L.A. Gizzi, L. Labate, L. Serafini, V. Petrillo and C. Vaccarezza, *"Linear and Nonlinear Thomson Scattering for Advanced X-ray Sources in PLASMONX "*, IEEE Trans. Plasma Sci. **36**, 4 (2008).

[76] A. Debus, S. Bock, M. Bussmann, T.E. Cowan, A. Jochmann, T. Kluge, S.D. Kraft, R. Sauerbrey, K. Zeil and U. Schramm, *"Linear and non-linear Thomson-scattering x-ray sources driven by conventionally and laser plasma accelerated electrons"*, Proc. SPIE 7359, 735908 (2009).

[77] https://espace.cern.ch/pwfa-network/default.aspx

[78] S.M. Wiggins, R.C. Issac, G.H. Welsh, E. Brunetti, R.P. Shanks, M.P. Anania, S. Cipiccia, G.G. Manahan, C. Aniculaesei, B. Ersfeld, M.R. Islam1, R.T.L. Burgess, G. Vieux, W.A. Gillespie, A.M. MacLeod, S.B. van der Geer, M.J. de Loos, D.A. Jaroszynski, *"High quality electron beams from a laser wakefield accelerator"*, Plasma Phys. Control. Fusion **52** (2010).

[79] M.R. Islam, E. Brunetti, R.P. Shanks, B. Ersfeld, R.C. Issac, S. Cipiccia, M.P. Anania, G.H. Welsh, S.M. Wiggins, A. Noble, R.A. Cairns, G. Raj, D.A. Jaroszynski, *"Near-threshold electron injection in the laser-plasma wakefield accelerator leading to femtosecond bunches"* (unpublished).

[80] G. Shvets, N.J. Fisch, *"Superradiant Amplification of an Ultrashort Laser Pulse in a Plasma by a Counterpropagating Pump"*, Phys. Rev. Lett. **81**, 22 (1998).

[81] R.M.G.M. Trines, F. Fiuza, R. Bingham, R.A. Fonseca, L.O. Silva, R.A. Cairns, P.A. Norreys, *"Simulations of efficient Raman amplification into the multipetawatt regime"*, Nature Phys. **7,** 87 (2011).

[82] I.S. Ruddock, W. Sibbett, D.J. Bradley, *"Direct generation of transform-limited sub-picosecond pulses in a mode-locked CW dye laser",* Opt. Commun. **18**, 1, 26-27 (1976).

[83] J. Zhou, I.P. Christov, G. Taft, C. Huang, M.M. Murnane and H.C. Kapteyn, *"Pulse evolution in a broad-bandwidth Ti:sapphire laser"*, Opt. Lett. **19**, 1149 (1994).

[84] D. Strickland, G. Mourou, *"Compression of amplified chirped optical pulses"*, Opt. Commun. **56**, 3 (1985).

[85] S. Svanberg, C.G. Wahlström, *"X-ray Lasers"*, Institute of Physics, Bristol (1996).

[86] J.J. Rocca, P.L. Hagelstein, *"Soft X-ray Lasers and Applications"*, Proc. SPIE 2520, SPIE, Bellingham, USA (1995).

[87] M. Tabak, J. Hammer, M.E. Glinsky, W.L. Kruer, S.C. Wilks, J. Woodworth. E., M. Campbell, M.D. Perry, *"Ignition and high gain with ultrapowerful lasers"*, Phys. Plasmas **1**, 1626 (1994).

[88] M. Roth, T.E. Cowan, M.H. Key, S.P. Hatchett, C. Brown, W. Fountain, J. Johnson, D.M. Pennington, R.A. Snavely, S.C. Wilks, K. Yasuike, H. Ruhl, F. Pegoraro, S.V. Bulanov, E.M. Campbell, M.D. Perry, H. Powell, *"Fast Ignition by Intense Laser-Accelerated Proton Beams"*, Phys. Rev. Lett. **86**, 436 (2001).

[89] G.A. Askar'yan, *"Effects of the gradient of a strong electromagnetic beam on electrons and atoms"*, Sov. Phys. JETP **15**, 1088 (1962).

[90] A.G. Litvak, *"Finite-amplitude wave beams in a magneto active plasma"*, Zh.Eksp. Theor. Fiz. **57** (1968) 629-636, Transl. Sov. Phys. JETP, **30**, 344 (1970).

[91] C. Max, J. Arons, A.B. Langdon, *"Self-modulation and self-focusing of electromagnetic waves in plasmas"*, Phys. Rev. Lett. **33**, 209 (1974).

[92] A.B. Borisov, A.V. Borovskiy, O.B. Shiryaev, V.V. Korobkin, A.M. Prokhorov, J.C. Solem, T.S. Luk, K. Boyer, C.K. Rhodes, *"Relativistic and Charge-Displacement Self-Channeling of Intense Ultrashort Laser Pulses in Plasmas"*, Phys. Rev. A **45**, 5830 (1992).

[93] P. Monot, T. Auguste, P. Gibbon, F. Jakober, G. Mainfray, A. Dulieu, M. Louis-Jacquet, G. Malka, J.L. Miquel, *"Experimental demonstration of relativistic self-channeling of a multiterawatt laser pulse in an underdense plasma"*, Phys. Rev. Lett. **74**, 2953 (1995).

[94] P. Sprangle, E. Esarey, J. Krall, G. Joyce, *"Propagation and guiding of intense laser pulses in plasmas"*, Phys. Rev. Lett. **69**, 2200 (1992).

[95] T. M. Antonsen Jr., P. Mora, *"Self-focusing and Raman scattering of laser pulses in tenuous plasmas"*, Phys. Rev. Lett. **69**, 2204 (1992).

[96] N.E. Andreev, L.M. Gorbunov, V.I. Kirsanov, A.A. Pogosova, R.R. Ramazashvili, *"Resonant excitation of wakefields by a laser-pulse in a plasma"*, JETP Lett. **55**, 571 (1992).

[97] C.A. Coverdale, C.B. Darrow, C.D. Decker, W.B. Mori, K-C. Tzeng, K.A. Marsh, C.E. Clayton, C. Joshi, *"Propagation of Intense Subpicosecond Laser Pulses through Underdense Plasmas"*, Phys. Rev. Lett. **74**, 4659 (1995).

[98] S.P. Le Blanc, M.C. Downer, R. Wagner, S.-Y. Chen, A. Maksimchuk, G. Mourou, D. Umstadter, *"Temporal Characterization of a Self-Modulated Laser Wakefield"*, Phys. Rev. Lett. **77**, 5381 (1996).

[99] N. E. Andreev, L. M. Gorbunov, V. I. Kirsanov,. A. A. Pogosova, and A. S. Sakhorov, *"Resonant excitation of wakefields by a laser pulse in a plasma"*, Plasma Phys. Rep. **22**, 379 (1996).

[100] C.D. Decker, W.B. Mori, T. Katsouleas, *"Particle-in-cell simulations of Raman forward scattering from short-pulse high-intensity lasers"*, Phys. Rev. E **50**, R3338(R) (1994).

[101] C.G. Durfee, III, J. Lynch, H.M. Milchberg, *"Development of a plasma waveguide for high-intensity laser pulses"*, Phys. Rev. E **51**, 2368 (1995).

[102] A. Chiron, G. Bonnaud, A. Dulieu, J.L. Miquel, G. Malka, M. Louis-Jacquet, G. Mainfray, *"Experimental observations and simulations on relativistic self-guiding of an ultra-intense laser pulse in underdense plasmas"*, Phys. Plasmas **3**, 1373 (1996).

[103] A.B. Borisov, X. Shi, V.B. Karpov, V.V. Korobkin, J.C. Solem, O.B. Shiryaev, A. McPherson, K. Boyer, C.K. Rhodes, *"Stable self-channeling of intense ultraviolet pulses in underdense plasma, producing channels exceeding 100 Rayleigh lengths"*, J. Opt. Soc. Am. B **11**, 1941 (1994).

[104] E. Esarey, J. Krall, P. Sprangle, *"Envelope analysis of intense laser pulse self-modulation in plasmas"*, Phys. Rev. Lett. **72**, 2887 (1994).

[105] D. Gordon, K.C. Tzeng, C.E. Clayton, A.E. Dangor, V. Malka, K.A. Marsh, A. Modena, W.B. Mori, P. Muggli, Z. Najmudin, D. Neely, C. Danson, C. Joshi, *"Observation of Electron Energies Beyond the Linear Dephasing Limit from a Laser-Excited Relativistic Plasma Wave"*, Phys. Rev. Lett. **80**, 2133 (1998).

[106] http://plasma.desy.de/e65240/e85405/index_eng.html

[107] M. Moisan, M. Chaker, Z. Zakrzewski, J. Paraszczak, *"The waveguide surfatron: a high power surface-wave launcher to sustain large-diameter dense plasma columns"*, J. Phys. E: Sci. Instrum. **20**, 1356 (1987).

[108] E. Esarey, C.B. Schroeder, W.P. Leemans, *"Physics of laser-driven plasma-based electron accelerators"*, Rev. Mod. Phys. **81**, 1229 (2009).

[109] C. Joshi, W.B. Mori, T. Katsouleas, J.M. Dawson, J.M. Kindel, D.W. Forslund, *"Ultrahigh gradient particle acceleration by intense laser-driven plasma density waves"*, Nature **311**, 525 (1984).

[110] T. Katsouleas, *"Physical mechanisms in the plasma wake-field accelerator"*, Phys. Rev. A **33**, 2056 (1986).

[111] P. Sprangle, B. Hafizi, J.R. Peñano, R.F. Hubbard, A. Ting, C.I. Moore, D.F. Gordon, A. Zigler, D. Kaganovich, T.M. Antonsen Jr., *"Wakefield generation and GeV acceleration in tapered plasma channels"*, Phys. Rev. E **63**, 056405 (2001).

[112] E. Esarey, B.A. Shadwick, C.B. Schroeder, W.P. Leemans, *"Nonlinear Pump Depletion and Electron Dephasing in Laser Wakefield Accelerators"*, AIP Conf. Proc. **737**, 578 (2004).

[113] M.J. de Loos, S.B. van der Geer, Y.M. Saveliev, V.M. Pavlov, A.J.W. Reitsma, S.M. Wiggins, J. Rodier, T. Garvey, D.A. Jaroszynski, *"Radial bunch*

compression: Path-length compensation in an rf photoinjector with a curved cathode", Phys. Rev. ST Accel. Beams **9**, 084201 (2006).

[114] C.B. Schroeder, E. Esarey, B.A. Shadwick, W.P. Leemans, *"Trapping and dark current in nonlinear plasma waves"*, Phys. Plasmas **13**, 33103 (2006).

[115] S. Wilks, T. Katsouleas, J.M. Dawson, P. Chen, J.J. Su, *"Beam Loading In Plasma Waves"*, IEEE Trans. Plasma Sci. **15**, 210 (1987).

[116] S.Wilks, T. Katsouleas, J.M. Dawson, J.J. Su, *"Beam Loading Efficiency in Plasma Accelerators"*, Proceeding of PAC87, **100**, Whashington DC, USA (1987).

[117] J.M.J. Madey, *"Relationship between mean radiated energy, mean squared radiated energy and spontaneous power spectrum in a power series expansion of the equation of motion in a FEL"*, Nuovo Cimento, **50B**, 64 (1979).

[118] D.H. Bilderback, P. Elleaume, E. Weckert, *"Review of third and next generation synchrotron light sources"*, J. Phys. B At. Mol. Opt. Phys. **38**, S773 (2005).

[119] R. Bonifacio, L. De Salvo, P. Pierini, N. Piovella, C. Pellegrini, *"Spectrum, temporal structure, and fluctuations in a high-gain free-electron laser starting from noise"*, Phys. Rev. Lett. **73**, 70 (1994).

[120] J.D. Jackson, *"Classical Electrodynamics"*, Wiley, Second Edition, Ch.14 (1975).

[121] R. Bonifacio, C. Pellegrini, L.M. Narducci, *"Collective instabilities and high-gain regime in a free electron laser"*, Opt. Commun. **50**, 373 (1984).

[122] Z. Huang, K.-J. Kim, *"Review of x-ray free-electron laser theory"*, Phys. Rev. ST Accel. Beams **10**, 034801 (2007).

[123] P. Schmüser, M. Dohlus, J. Rossbach, C. Behrens, *"Free-Electron Lasers in the Ultraviolet and X-Ray Regime"*, Springer Tracts in Modern Physics **258** (2014).

[124] J.E. LaSala, D.A.G. Deacon, J.M.J. Madey, *"Optical guiding in a free-electron–laser oscillator"*, Phys. Rev. Lett. **59**, 2047 (1987).

[125] S. Reiche, *"GENESIS 1.3: a fully 3D time-dependent FEL simulation code"*, Nucl. Instrum. Methods Phis. Res., Sect. A **429**, 243 (1999).

[126] T. Tanaka, *"FEL simulation code for undulator performance estimation"*, Proceedings of FEL2004, **435**, Trieste, Italy (2004).

[127] E.L. Saldin, E.A. Schneidmiller, M.V. Yurkov, *"Calculation of energy diffusion in an electron beam due to quantum fluctuations of undulator radiation"*, Nucl. Instr. and Meth. A**381**, 545 (1996).

[128] S. Reiche, B. Faatz, *"Status of the 3D Time-Dependent FEL Simulation Code GENESIS 1.3"*, UCLA PBPL **311** (2008).

[129] T. Tanaka, *"Reference manual for SIMPLEX 1.3 – an X-ray FEL Practical SIMulator"*, Japan, 2008.

[130] H. Wiedemann, *"Particle Accelerator Physics"*, Springer Publications (2007).

[131] S.I Tzenov, *"Contemporary accelerator physics"*, World Scientific Publishing Co. (2004).

[132] M.P. Anania, D. Clark, S.B. van der Geer, M.J. de Loos, R. Isaac, A.J.W. Reitsma, G.H. Welsh, S.M. Wiggins, D.A. Jaroszynski, *"Transport of ultra-short electron bunches in a free-electron laser driven by a laser-plasma wakefield accelerator"*, Proc. SPIE 7359, Harnessing Relativistic Plasma Waves as Novel Radiation Sources from Terahertz to X-Rays and Beyond, 735916 (2009).

[133] S. B. van der Geer and M. J. de Loos, *"General Particle Tracer code: design, implementation and application"*, GPT Manual (2001).

[134] S. Jolly, *"An Intra-pulse Fast Feedback System for a Future Linear Collider"*, Ph.D. Thesis, Exeter College, Oxford (2003).

[135] T. Eichner, F. Grüner, S. Becker, M. Fuchs, D. Habs, R. Weingartner, U. Schramm, H. Backe, P. Kunz, W. Lauth, *"Miniature magnetic devices for laser-based, table-top free-electron lasers"*, Phys. Rev. ST Accel. Beams **10**, 082401 (2007).

[136] S. Humphries Jr., *"Charged particle beams"*, New York, Wiley (1990).

[137] J. D. Lawson, *"The Physics of charged particle beams"*, Clarendon (1977).

[138] R. B. Miller, *"Introduction to the Physics of intense charged particle beams"*, Plenum (1982).

[139] S. Humphries Jr., *"Principle of charged particle acceleration"*, New York, Wiley (1986).

[140] http://www.cst.com/

[141] B.J.A. Shepherd, J.A. Clarke, *"Design, measurement and correction of a pair of novel focusing undulators for the ALPHA-X project"*, Nucl. Instrum. Methods Phys. Res., Sect. A **654**, 8 (2011).

[142] C.P. Browne, W.W. Buechner, *"Broad-Range Magnetic Spectrograph"*, Rev. Sci. Instrum. **27**, 899 (1956).

[143] D.C. Carey, K.L. Brown, F. Rothacker, *"Third-Order TRANSPORT with MAD input: a computer program for designing charged particle beam transport systems"*, FERMILAB-Pub-**98**/310 (1998).

[144] G.P.A. Malcolm, A.I. Ferguson, *"Self-mode locking of a diode-pumped Nd:YLF laser"*, Opt. Lett. **16,** 1967 (1991).

[145] T. Hosokai, K. Kinoshita, A. Zhidkov, K. Nakamura, T. Watanabe, T. Ueda, H. Kotaki, M. Kando, K. Nakajima and M. Uesaka, *"Effect of a laser prepulse on a narrow-cone ejection of MeV electrons from a gas jet irradiated by an ultrashort laser pulse"*, Phys. Rev. E **67**, 036407 (2003).

[146] T. Hosokai, K. Kinoshita, T. Ohkubo, A. Maekawa, M. Uesaka, A. Zhidkov, A. Yamazaki, H. Kotaki, M. Kando, K. Nakajima, S.V. Bulanov, P. Tomassini, A. Giulietti, D. Giulietti, *"Observation of strong correlation between quasimonoenergetic electron beam generation by laser wakefield and laser guiding inside a preplasma cavity"*, Phys. Rev. E **73**, 036407 (2006).

[147] H. Kotaki, M. Kando, I. Daito, T. Homma, T. Kameshima, K. Kawase, L.M. Chen, Y. Fukuda, H. Kiriyama, S. Kondo, S. Kanazawa, Y. Nakai, T. Shimomura, M. Tanoue, A. Akutsu, H. Okada, T. Motomura, H. Daido, S.V. Bulanov, *"Contrast Effect on the Laser Injected Electron Beam"*, Laser-driven relativistic plasmas applied to Science, Industry and Medicine: 2nd Int. Symp. **1153**, 1, AIP Publishing (2009).

[148] P. Maine, D. Strickland, P. Bado, M. Pessot, G. Mourou, *"Generation of ultrahigh peak power pulses by chirped pulse amplification"*, IEEE J. Quantum Elect. **24**, 398 (1988).

[149] C. Iaconis, I.A. Walmsley, *"Self-Referencing Spectral Interferometry for Measring Ultrashort Optical Pulses"*, IEEE J. Quantum Elect. **35**, 501 (1999).

[150] C. Aniculaesei, Ph.D. thesis, Strathclyde University (to be submitted).

[151] R. Weingartner, S. Raith, A. Popp, S. Chou, J. Wenz, K. Khrennikov, M. Heigoldt, A.R. Maier, N. Kajumba, M. Fuchs, B. Zeitler, F. Krausz, S. Karsch, F. Gruner, *"Ultralow emittance electron beams from a laser-wakefield accelerator"*, Phys. Rev. ST Accel. Beams **15**, 111302 (2012).

[152] B.W. Miller, H. Bradford Barber, H.H. Barrett, D.W. Wilson, L. Chen, *"A low-cost approach to high-resolution, single-photon imaging using columnar scintillators and image intensifiers"*, Nuclear Science Symposium Conference Record, **6**, 3540 (2006).

[153] M. William Yen, S. Shionoya, H. Yamamoto, *"Practical Applications of Phosphors"*, CRC Press (2006).

[154] J. Miyahara, K. Takahashi, Y. Amemiya, N. Kamiya, Y. Satow, *"A new type of X-ray area detector utilizing laser stimulated luminescence"*, Nucl. Instr. Methods Res., Sect. A **246**, 572 (1986).

[155] Y. Amemiya, T. Matsushita, A. Nakagawa, Y. Satow, J. Miyahara, J-I. Chikawa, *"Design and performance of an imaging platesystem for X-ray diffraction study"*, Nuc. Instrum. Methods Phys. Res., Sect. A **266**, 645 (1988).

[156] Fuji Internal Report: http://www.fujifilm.com/products/life science/si imgplate/img plate.html

[157] R.P. Shanks, M.P. Anania, E. Brunetti, S. Cipiccia, B. Ersfeld, J.G. Gallacher, R.C. Issac, M.R. Islam, G. Vieux, G.H. Welsh, S.M. Wiggins, D.A. Jaroszynski, *"Pepper-pot emittance measurement of laser-plasma wakefield accelerated electrons"*, Proc. SPIE **7359**, 735907 (2009).

[158] G. Manahan, *"Studies of transverse properties of relativistic electrons from laser wakefield accelerator"*, Ph.D. Thesis, University of Strathclyde.

[159] B.J.A. Shepherd & J.A. Clarke, ASTeC, *"Magnetic design of a focusing undulator for ALPHA-X"*, Proceedings of EPAC 2004, **MOPKF066**, Lucerne, Switzerland (2004).

[160] R.C. Issac, G. Vieux, G.H. Welsh, R. Shanks, E. Brunetti, S. Cipiccia, M.P. Anania, X. Yang, S.M. Wiggins, M.R. Islam, B. Ersfeld, J. Farmer, G. Raj, S. Chen, D. Clark, T. McCanny, D.A. Jaroszynski, *"Electron beam pointing stability of a laser wakefield accelerator"*, Proc. SPIE **7359**, 735915 (2009).

[161] R. Shanks, *"Comprehensive Characterisation of Laser Plasma Wakefield Accelerated Electrons"*, Ph.D. Thesis, University of Strathclyde.

[162] http://www.fujifilmusa.com/products/medical/cr-systems/fujifilm-imaging-plates/

[163] H.-P. Schlenvoigt, K. Haupt, A. Debus, F. Budde, O. Jäckel, S. Pfotenhauer, H. Schwoerer, E. Rohwer, J.G. Gallacher, E. Brunetti, R.P. Shanks, S.M. Wiggins, D.A. Jaroszynski, *"A compact synchrotron radiation source driven by a laser-plasma wakefield accelerator"*, Nature Phys. **4**, 130 (2008).

[164] G.C. Walker, W. Jarzeba, T.J. Kang, A.E. Johnson, P.F. Barbara, *"Ultraviolet Femtosecond Fluorescence Spectroscopy: Techniques and Applications"*, J. Opt. Soc. Am. B **7**, 1521 (1990).

[165] T. Kobayashi, Y. Kida, *"Ultrafast spectroscopy with sub-10 fs deep-ultraviolet pulses"*, Phys. Chem. Chem. Phys. **14**, 6200 (2012).

[166] A.H. Zewail, *"Femtochemistry"*, J. Phys. Chem. A **104**, 5660 (2000).

[167] V. Sundström, *"Femtobiology"*, Annu. Rev. Phys. Chem. **59**, 53 (2008).

[168] B.W.J. McNeil, G.R.M. Robb, D.A. Jaroszynski, *"Self-amplification of coherent spontaneous emission in the free electron laser"*, Opt. Commun. **165**, 65 (1999).

[169] D.A. Jaroszynski, R.J. Bakker, A.F.G. van der Meer, D. Oepts, P.W. van Amersfoort, *"Coherent startup of an infrared free-electron laser"*, Phys. Rev. Lett. **71**, 3798 (1993).

[170] S.M. Wiggins, D.A. Jaroszynski, B.W.J. McNeil, G.R.M. Robb, P. Aitken, A.D.R. Phelps, A.W. Cross, K. Ronald, V.G. Shpak, M.I. Yalandin, S.A. Shunailov, M.R.

Ulmaskulov, N.S. Ginzburg, *"Self-amplification of coherent spontaneous emission in a Cherenkov free-electron maser"*, Phys. Rev. Lett. **84**, 2393 (2000).

[171] G.R. Plateau, C.G.R. Geddes, D.B. Thorn, M. Chen, C. Benedetti, E. Esarey, A.J. Gonsalves, N.H. Matlis, K. Nakamura, C.B. Schroeder, S. Shiraishi, T. Sokollik, J. van Tilborg, Cs. Toth, S. Trotsenko, T.S. Kim, M. Battaglia, Th. Stöhlker, W.P. Leemans, *"Low-emittance electron bunches from a laser-plasma accelerator measured using Single-Shot X-Ray spectroscopy"*, Phys. Rev. Lett. **109**, 6, 064802 (2012).

[172] S. Kneip, C. McGuffey, J.L. Martins, M.S. Bloom, V. Chvykov, F. Dollar, R. Fonseca, S. Jolly, G. Kalintchenko, K. Krushelnick, A. Maksimchuk, S.P.D. Mangles, Z. Najmudin, C.A.J. Palmer, K. Ta Phuoc, W. Schumaker, L.O. Silva, J. Vieira, V. Yanovsky, A.G.R. Thomas, *"Characterization of transverse beam emittance of electrons from a laser-plasma wakefield accelerator in the bubble regime using betatron x-ray radiation"*, Phys. Rev. ST Accel. Beams **15**, 021302 (2012).